Evolution of CALIFA: From single detector modules to benchmark reactions

Die Entwicklung von CALIFA: Von einzelnen Detektoren zu Testreaktionen
Dem Fachbereich Physik der Technischen Universität Darmstadt
zur Erlangung des Grades eines Doktors der Naturwissenschaften (Dr. rer. nat.)
genehmigte Dissertation von M.Sc. Anna-Lena Hartig aus Aschaffenburg
Tag der Einreichung: 22.06.2021, Tag der Prüfung: 19.07.2021

1. Gutachten: Prof. Dr. Thorsten Kröll
2. Gutachten: Prof. Dr. Joachim Enders

Darmstadt 2021 - D17

TECHNISCHE UNIVERSITÄT DARMSTADT

Fachbereich Physik
Institut für Kernphysik
AG Kröll

GEFÖRDERT VOM

Bundesministerium für Bildung und Forschung

ENSAR2

HGS-HIRe for FAIR
Helmholtz Graduate School for Hadron and Ion Research

Evolution of CALIFA: From single detector modules to benchmark reactions
Die Entwicklung von CALIFA: Von einzelnen Detektoren zu Testreaktionen

Doctoral thesis by M.Sc. Anna-Lena Hartig

1. Review: Prof. Dr. Thorsten Kröll
2. Review: Prof. Dr. Joachim Enders

Date of submission: 22.06.2021
Date of thesis defense: 19.07.2021

Darmstadt 2021 - D17

Erklärung gemäß §9 Promotionsordnung

Hiermit versichere ich, dass ich die vorliegende Dissertation selbstständig angefertigt und keine anderen als die angegebenen Quellen und Hilfsmittel verwendet habe. Alle wörtlichen und paraphrasierten Zitate wurden angemessen kenntlich gemacht. Die Arbeit hat bisher noch nicht zu Prüfungszwecken gedient.

Darmstadt, 22.06.2021

M.Sc. Anna-Lena Hartig

Abstract

As one of the key detectors of the R^3B setup (**R**eactions with **R**adioactive **R**elativistic **B**eams) at FAIR (**F**acility for **A**ntiproton and **I**on **R**esearch), the CALIFA (**CAL**orimeter for the **I**n **F**light detection of γ rays and light charged p**A**rticles) detector array surrounds the reaction target and measures γ rays with energies of $100\,\mathrm{keV} < E_\gamma < 30\,\mathrm{MeV}$ as well as light charged particles up to $E_{particle} = 700\,\mathrm{MeV}$. The entire array will consist of 1952 CsI(Tl) scintillating crystals in the Barrel and 460 crystals in the Endcap part. Each crystal is read-out by a **L**arge **A**rea **A**valanche **P**hoto **D**iode.
To match the requirements, several steps, tests and quality assurance procedures have to be fulfilled in order to provide the basic components of the CALIFA array. This work gives a detailed description of the assembly of 120 Endcap detector-units and the equipment of two Endcap segments. Furthermore, a gain-matching procedure is performed on the two Endcap segments and their energy resolution is compared to additional test results on the same crystals and to test data stemming from Barrel detectors.
A benchmark experiment was performed at the Bronowice Cyclotron Center in Kraków using the quasi-free scattering reaction ^{208}Pb$(p, 2p)^{207}$Tl in direct kinematics. Within the scope of the experiment, a monoenergetic proton beam of $E_{beam} = 200\,\mathrm{MeV}$ impinged on a ^{208}Pb target and the outgoing protons and γ rays were detected by 3 CALIFA petals, containing 64 crystals each. Additionally, two DSSSDs (**D**ouble **S**ided **S**ilicon **S**trip **D**etectors) were used to enable vertex reconstruction. The entire setup was read-out by the CALIFA DAQ and operated in air.
As proof of concept, two known γ transitions in ^{207}Tl could be identified studying the reaction ^{208}Pb$(p, 2p)^{207}$Tl. In coincidence with one proton, the transition from the $11/2^-$-state, with a lifetime of $1.33\,\mathrm{s}$, could be observed. Furthermore, it could be shown in this work that the coincident measurement of the two outgoing protons together with the γ ray, stemming from the transition of the $5/2^+$-state to the $3/2^+$-state in ^{207}Tl, is feasible. For use at FAIR, the performance of the CsI(Tl) detectors matches the requirements of CALIFA.
The conducted experiment is the first successful measurement of a $(p, 2p\gamma)$ reaction for such heavy nuclei and therefore was a good test case for experiments planned at FAIR that will investigate nuclei in the third r-process peak.

Zusammenfassung

Als einer der Schlüsseldetektoren des R^{3}B Aufbaus (**R**eactions with **R**adioactive **R**elativistic **B**eams) an FAIR (**F**acility for **A**ntiproton and **I**on **R**esearch), umgibt der CALIFA-Detektoraufbau (**CAL**orimeter for the **I**n **F**light detection of γ rays and light charged p**A**rticles) das Reaktionstarget und misst sowohl γ-Strahlen mit Energien von $100\,\mathrm{keV} < E_\gamma < 30\,\mathrm{MeV}$ als auch leichte geladene Teilchen mit Energien von bis zu $E_{particle} = 700\,\mathrm{MeV}$. Der gesamte Aufbau wird aus 1952 CsI(Tl)-Szintillationskristallen im Barrel und 460 Kristallen im Endcapteil bestehen. Jeder Kristall wird mit einer **L**arge **A**rea **A**valanche **P**hoto **D**iode ausgelesen.
Um den Anforderungen zu genügen, werden diverse Fertigungsschritte, Tests und Qualitätsicherungsmaßnahmen durchgeführt, um die Grundkomponenten des CALIFA Aufbaus zur Verfügung zu stellen. Die vorliegende Arbeit beinhaltet eine detailierte Beschreibung der Herstellung von 120 Endcapdetektoreinheiten und der Bestückung von zwei Endcapsegmenten. Darüberhinaus wurde ein Verfahren zur Anpassung der Verstärkung an zwei Endcapsegmenten durchgeführt und die Energieauflösung der Kristalle wurde mit weiteren Testergebnissen und mit Testdaten von Barreldetektoren verglichen.
Am Bronowice Cyclotron Center in Krakau wurde ein Testexperiment durchgeführt, das sich der quasifreien Streuung ^{208}Pb$(p, 2p)^{207}$Tl in direkter Kinematik bediente. Dazu wurde ein monoenergetischer Protonenstrahl von $\mathrm{E}_{Beam} = 200\,\mathrm{MeV}$ auf ein ^{208}Pb-Target geleitet und die ausgehenden Protonen und γ-Quanten wurden mit drei CALIFA-Petals, die je 64 Kristalle enthalten, vermessen. Zusätzlich wurden zwei DSSSDs (**D**ouble **S**ided **S**ilicon **S**trip **D**etectors) genutzt um die Scheitelpunktrekonstruktion durchzuführen. Der gesamte Aufbau wurde mit der CALIFA-DAQ ausgelesen und an Luft betrieben.
Zum Konzeptnachweis wurden zwei bekannte γ-Übergänge in ^{207}Tl mit Hilfe der Reaktion ^{208}Pb$(p, 2p)^{207}$Tl identifiziert. Zusammen mit einem Proton wurde der γ-Übergang vom $11/2^-$-Zustand mit einer Lebensdauer von $1.33\,\mathrm{s}$ beobachtet. Weiterhin konnte in dieser Arbeit gezeigt werden, dass die Messung von zwei ausgehenden Protonen zusammen mit dem γ-Quant, das vom Übergang vom $5/2^+$-Zustand zum $3/2^+$-Zustand in ^{207}Tl stammt, umsetzbar ist. Zur Nutzung an FAIR genügen die Ergebnisse der CsI(Tl)-Detektoren den Ansprüchen von CALIFA.
Das durchgeführte Experiment ist die erste erfolgreiche Messung einer $(p, 2p\gamma)$-Reaktion für solch schwere Kerne und deshalb ein guter Testfall für die geplanten Experimente an FAIR, die Kerne der $A = 196$ Erhöhung in den Elementhäufigkeiten des r-Prozesses untersuchen werden.

Contents

1. Introduction

The atomic nucleus consists of protons and neutrons and its number of protons defines the chemical element and its chemical properties. What seems to be clear nowadays, needed millenia of considerations and experiments in order to form a model of the atomic nucleus that is compliant with observations. A milestone was a series of scattering experiments of α-particles on a gold foil performed by H.Geiger and E.Marsden in the group of E.Rutherford in 1909 [1] revealing the concentration of positive charge and mass at a point [2].

1.1. Nuclear theory

The finding of the nucleus together with the discovery of the proton in 1920 [3] and of the neutron in 1932 [4] necessitated the development of modern nuclear models that are capable of reproducing experimental results. A first successful description of the nuclear binding energy was established in 1935 by H.Bethe and C.F.v.Weizsäcker [5] describing the nucleus as a liquid drop consisting of a homogenous charged medium, like proposed by N.Bohr [6], and adding the asymmetry and pairing term.

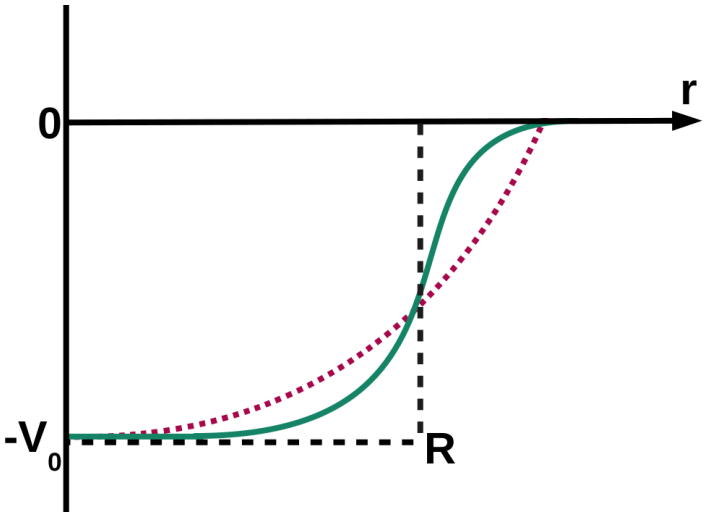

Figure 1.1.: The nuclear potential approximated by box (dashed), Wood-Saxon (continuous) and a harmonic-oscillator potential (dotted).

1.1.1. Fermi-gas model

The next step, that took the internal structure of the nucleus more into account, was done by introducing the Fermi-gas model of the atomic nucleus. Within this model protons and neutrons are described as spin-$\frac{1}{2}$ particles that obey the Pauli principle while moving independently and without interacting with each other within a defined potential well. The source of this well is the superposition of the nucleon-nucleon

force between the nucleons. As for most nuclei, there is no exact solution of the Schrödinger equation for many-body problems, the resulting well needs to be replaced by an easy to handle approximation like the box potential or the harmonic-oscillator potential as shown in Figure 1.1. An alternative to the before mentioned approximations is the Wood-Saxon potential

$$V(r) = -V_0[1 + e^{\frac{r-R}{a}}]^{-1} \tag{1.1}$$

with the depth of the potential $V_0 = 40\,\mathrm{MeV}$, the nuclear radius R and a parameter a that describes the density distribution of the nuclear boundary [7]. The Wood-Saxon potential is a radial symmetric potential that reproduces the measured particle density within the nucleus. The solution of the Schrödinger equation for one single nucleon is now a set of discrete energy states. Each state can be occupied according to the Pauli exclusion principle by two nucleons of the same kind starting with the lowest available level up to full occupation, as outlined in Figure 1.2. Nucleons in the highest occupation level have the Fermi energy E_F and the Fermi momentum p_F defined as

$$E_F = (\frac{1}{2}m)3^{\frac{2}{3}}\pi^{\frac{4}{3}}\hbar^2(\frac{n}{\tau})^{\frac{2}{3}} = 30\,\mathrm{MeV}[7] \tag{1.2}$$

and

$$p_F = \frac{\hbar}{R}(\frac{9\pi}{8})^{\frac{1}{3}} \approx 250\,\mathrm{MeV/c}[8] \tag{1.3}$$

with nucleon mass m, the nuclear radius R and the density of the nuclear matter $\frac{n}{\tau}$. For heavy nuclei the density is approximately constant over the entire nuclear radius.
The Fermi-gas model reproduces the different occupation numbers for neutron and protons due to the Coulomb repulsion, but fails in reflecting the observed magic numbers 2, 8, 20, 28, 50, 82 and 126 for neutrons. Theses numbers represent nuclei that are especially strongly bound due to their closed nuclear shells.

1.1.2. Shell model

In 1949 M.Goeppert-Mayer and J.Jensen discovered independently the importance of the spin-orbit coupling $(\vec{l} \cdot \vec{s})$ and added it to the single-particle potential [9], [10]

$$V_i = V(r) + V_{ls}(r)(\vec{l} \cdot \vec{s}) + V_{Rest}, \tag{1.4}$$

hence expanding the Fermi-gas model towards the shell model. V_{Rest} reflects effects of the nucleon-nucleon interaction that are not described by the central potential.
The introduction of the spin-orbit interaction results in the energy splitting of the states with different total angular momenta $j = l \pm 1/2$. Unlike in the atomic electron-shells, $j = l + 1/2$ states have lower energy than the $j = l - 1/2$ states. This leads to a occupation of the main shells resulting in the formation of shell closures at the well known magic numbers. Nuclei with magic proton and/or neutron number are stronger bound than nuclei in their vicinity, resulting in higher separation energies for single nucleons and higher lying excitation energies.
The shell model is an established theory of the atomic nucleus but reaches its limits when going to more neutron or proton-rich nuclei. To increase and proof the accuracy of shell-model predictions for exotic nuclei, many dedicated beam facilities and experiments have been developed in the past decades. One facility, namely FAIR, specialized in the investigation of exotic heavy-ions, is discussed in the following section.
Modern approaches to nuclear theory are mostly mean-field models or ab-initio calculations. For the later, a

derivation of nucleon-nucleon interaction directly from QCD(**Q**uantum **C**hromo**D**ynamics) is done. Effective field theories take into account symmetries of the QCD and employ mathematical many-body methods. The application of this approach was limited to light nuclei, but could be expanded to medium-mass nuclei in the past years. For heavy nuclei, no ab-initio calculations are available up to now, hence mean-field approaches have to be made. Core of a mean-field model is an effective potential that affects a single nucleon while the potential is created by all other nucleons. Mean-field approaches like the IPM (**I**ndependent-**P**article **M**odel) exploit a central potential, for example a Wood-Saxon Potential, and neglect the effects of two-body correlations [11]. The applicability of mean-field models ranges from light to heavy nuclei.

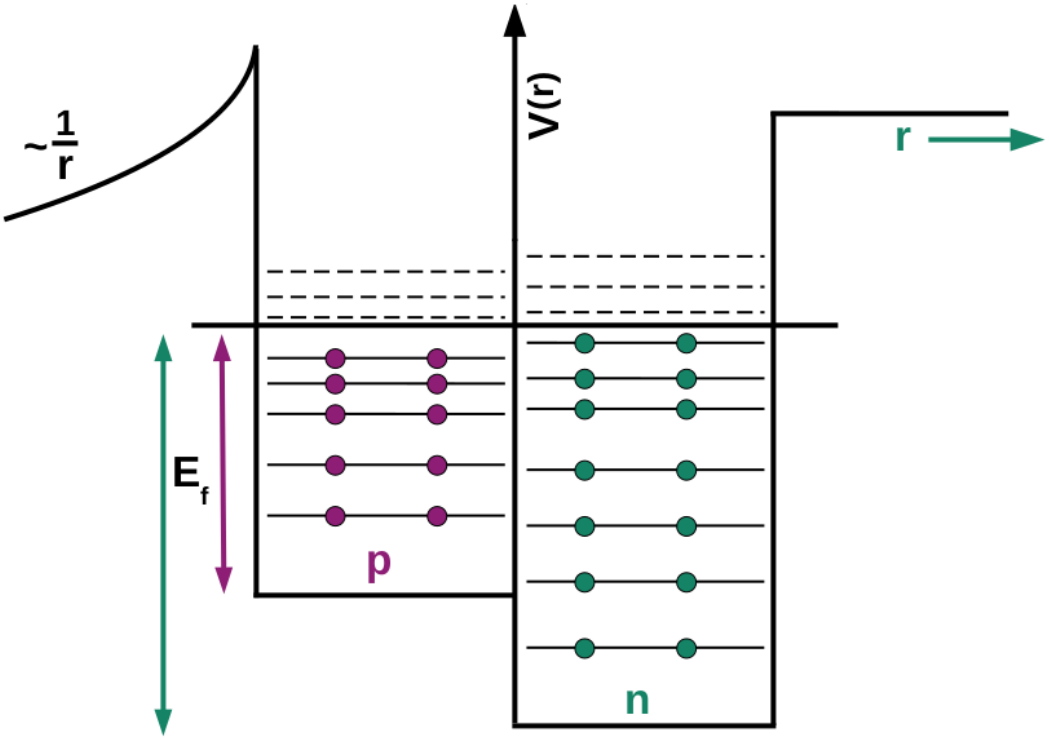

Figure 1.2.: Potential well with energy levels for neutrons and protons like described by the Fermi-gas model. The potential well for neutrons is deeper than for protons due to the missing Coulomb repulsion, resulting in different Fermi energies E_F for neutrons and protons.

1.2. FAIR and R^{3}B

Currently under construction, the FAIR facility (**F**acility for **A**ntiproton and **I**on **R**esearch) offers an excellent experimental side to study exotic nuclei produced by the in-flight method. For this purpose a production target is bombarded by a stable heavy-ion beam. The result is a variety of nuclei stemming from fragmentation, fission, and spallation processes that can be identified by a following fragment separator. In order to produce highly relativistic and exotic secondary-beams of highest intensities, already at the first stage high beam energies and intensities are needed. At FAIR, see Figure 1.3, this is achieved by the SIS100 synchrotron that accelerates the primary beam with an intensity of $5 \cdot 10^{11}\,\frac{\text{particles}}{\text{s}}$ up to an energy of $1.5\,\text{AGeV}$ [12]. This high-intensity primary-beam enables the Super-FRS (**super**-conducting **FR**agment **S**eparator) with its large angular ($\Delta\Phi_x = \pm 40\,\text{mrad}$ and $\Delta\Phi_y = \pm 20\,\text{mrad}$) and momentum ($\frac{\Delta p}{p} = \pm 2.5\,\%$) acceptance [13] and high transmission to select the desired exotic secondary-beam up to an energy of $1\,\text{AGeV}$ while exceeding the existing FRS by a factor of 10^3 in terms of intensity [14].

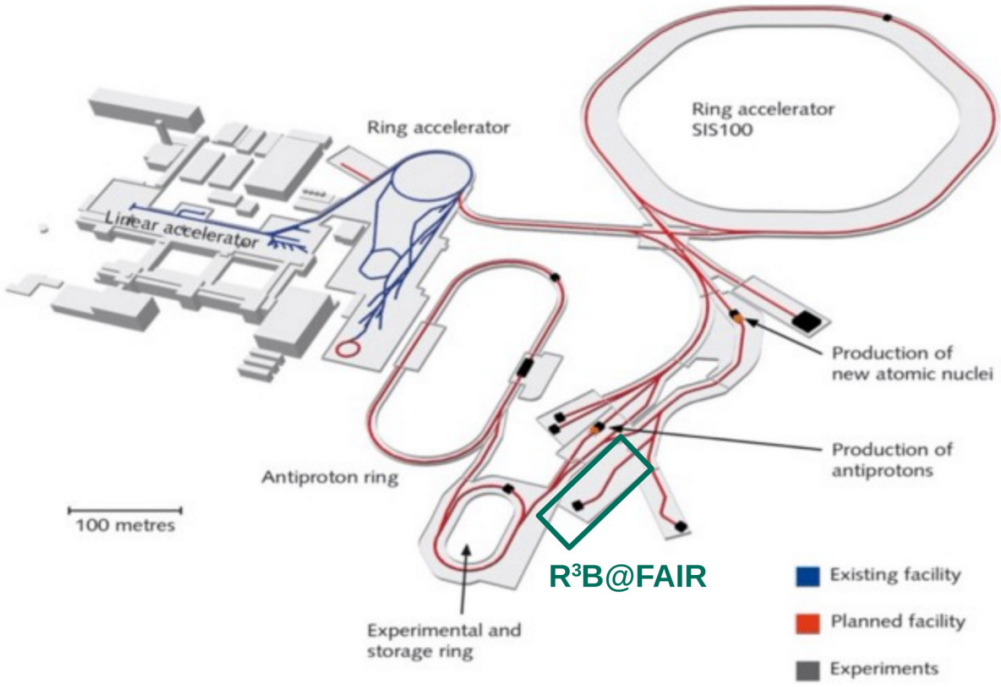

Figure 1.3.: The FAIR experimental site displaying the existing GSI facility (blue) and the planned expansion (red), currently under construction ©GSI/FAIR [15].

At the end of the high-energy branch of the Super-FRS, experiments with exotic nuclei will be conducted mostly in inverse kinematics employing for example the R^{3}B setup (**R**eactions with **R**adioactive **R**elativistic **B**eams). At this experimental site, shown in Figure 1.4, the charge Z and mass A of the secondary beam particles as well as their position are identified before impinging on the reaction target that is surrounded by a multi-layer silicon-tracker array. The silicon tracker detects light charge reaction-fragments and determines their first point of interaction. Both reaction target and tracker are surrounded by the R^{3}B calorimeter CALIFA (**CALI**orimeter for the **I**n **F**light detection of γ rays and light charged p**A**rticles) that detects γ rays and light charged particles, and will be discussed in detail in Chapter 2. In forward direction

emitted charged reaction products are deflected by the superconducting dipole magnet GLAD(**G**SI **L**arge **A**cceptance **D**ipole) according to their momentum to charge ratio. The magnet is positioned $1\,\mathrm{m}$ behind the reaction target and offers a magnetic field integral of up to $4.8\,\mathrm{Tm}$ [16]. Behind the magnet a set of tracking detectors such as fiber detectors and time-of-flight walls gives crucial information to determine the momenta and masses of protons and the heavy charged fragments. The momenta of neutrons are determined by NeuLAND (new **L**arge-**A**rea **N**eutron **D**etector) via position and time-of-flight measurements.

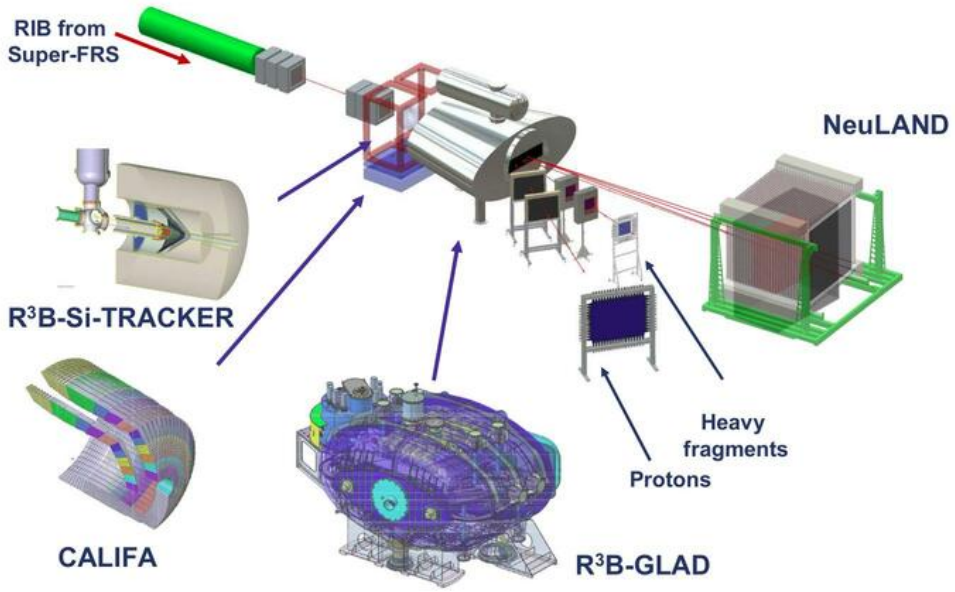

Figure 1.4.: Key detectors of the R^{3}B setup that is supplied with secondary beams by the Super-FRS ©GSI/FAIR [15].

The R^{3}B setup allows for performing kinematically complete measurements and the investigation of the nuclear structure of exotic nuclei. In the following a set of useful reaction-types like Coulomb excitation, fission as well as knockout and quasi-free scattering shall be shortly discussed as they demonstrate the many facets and the importance of the R^{3}B setup.

Coulomb excitation

In Coulomb excitation experiments the long-range electromagnetic interaction with the changing field of a projectile particle causes the excitation of the target nucleus. As the well-known electric Coulomb force causes the excitation, less understood processes such as nuclear interactions and magnetic excitations are smaller. Therefore, reduced transition-strengths like $B(E2; 0^+ \rightarrow 2^+)$ allow for the investigation of collectivity and probing of shell closures.

Fission

Another type of experiments able to reveal a lot of information on nuclear structure are fission experiments. The fission-fragment distribution in Z and A as well as their kinetic energies are of great interest for the

production of neutron-rich secondary beams as well as for the incineration of nuclear waste. Moreover, gained knowledge of the fission process and the neutron-rich nuclei will eventually lead to a deeper understanding of the nucleo-synthesis [17] [18].

Knockout and quasi-free scattering

The scattering of protons from single nucleons or clusters within a nucleus enables direct access to the single-particle wave-function. For beam energies of $700\,\mathrm{AMeV}$ the nucleus appears nearly transparent for the reaction products. This makes probing of valence nucleons as well as investigation of deeply bound nucleons possible. Therefore, it is a perfect tool to investigate single-particle properties of exotic nuclei.

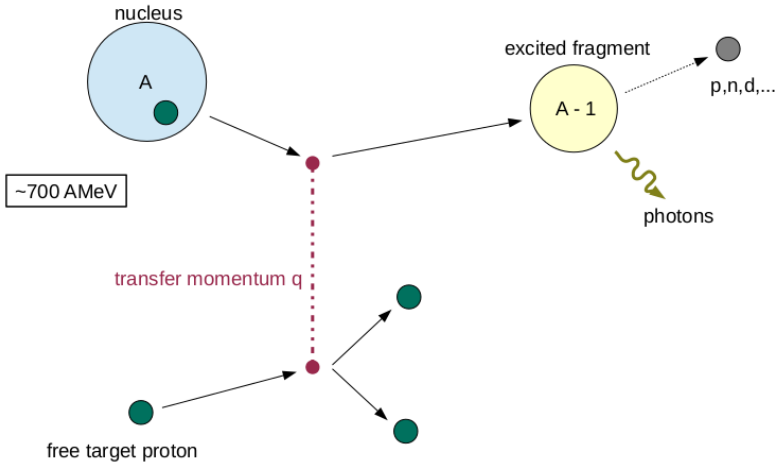

Figure 1.5.: Schematic representation of quasi-free scattering performed in inverse kinematics like conducted at R^{3}B.

Besides the above described experiments, also other reaction types like spallation, total-absorption measurements and many more are feasible with the R^{3}B setup. Anyhow, in the following section the focus will be on the quasi-free scattering process that was employed in direct kinematics for the benchmark experiment of the R^{3}B calorimeter CALIFA. For details on CALIFA see Chapter 2 and for an overview of the conducted benchmark experiment see Chapter 4.

1.3. Quasi-free scattering

Quasi-free scattering (QFS) reactions of the form (p, pN) describe a process in which an incident proton with energy E_0 and momentum $\vec{k}_0$ is scattered on a bound nucleus (or cluster) as if both participants are free and the nucleon (or cluster) is scattered out of the nucleus, as shown in Figure 1.6. This ejected particle N might be a single nucleon, but also a deuteron, triton or any other cluster of the nucleus. With regard to the later discussed benchmark experiment, the further discussion is confined to an ejected proton, hence a $(p, 2p)$ reaction. A classic definition of the reaction was given by Jacob and Marris [19] [20], who delivered a theoretical description in the second half of the 20th century, which states:

"Qualitatively speaking, by quasi-free scattering a process is meant in which a high energy $(100 - 1000\,\mathrm{MeV})$ particle knocks a nucleon out of a nucleus and no further violent interaction occurs between the nucleus and the incident or the two outgoing particles."[19]

To ensure no further interaction between the nucleus and the protons takes place, the energy E_0 of the incoming proton needs to be sufficiently high to fulfill the adiabatic approximation [21]. The adiabatic or sudden approximation states, that if the beam energy is high enough, the reaction occurs faster than the internal motion of the nucleons. As a consequence the core of the nucleus is treated as spectator of the reaction. In addition, also the eikonal approximation is exploited to simplify theoretical calculations treating projectile trajectories as well defined straight lines while passing the target field.

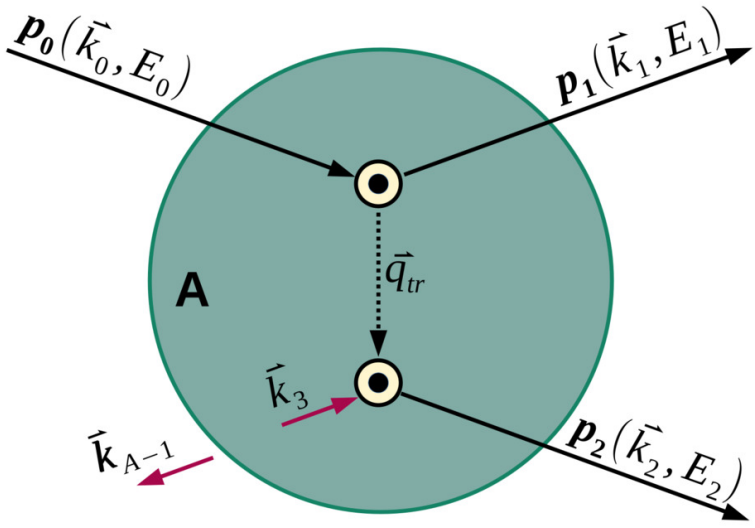

Figure 1.6.: Schematic view of the quasi-free scattering $(p, 2p)$ reaction in the rest frame of the target nucleus.

After the ejection of a proton, the residual $(A-1)$ nucleus exhibits a hole in the proton's former energy level. If the hole is created in a deeper lying state, this can cause an additional excitation energy E^*_{A-1} of the residual nucleus. Hence, the binding energy of the struck nucleon B_N can be calculated using

$$B_N = S_N + E^*_{A-1} = T_0 - (T_1 + T_2 + T_{A-1}) \tag{1.5}$$

where T_0, T_1, T_2 and T_{A-1} represent the kinetic energies of the incident proton, the scattered proton, the knocked-out nucleon and the residual fragment, respectively. Moreover, $S_N = (M_A - M_{A-1} - m_N)c^2$ denotes the separation energy of the weakest bound nucleon in the nucleus. Therefore, two cases emerge, namely:

- $0 < E^*_{A-1} < S_{A-1}$ De-excitation of the fragment via emission of γ rays
- $E^*_{A-1} > S_{A-1}$ Breakup of the residual nucleus by emission of a nucleon

In any case, the binding energy spectrum is expected to show peaks at the energies corresponding to various nuclear shells from which the nucleon can be removed.
Besides the binding energy of a nucleon, also its internal momentum $\vec{k}_3$ inside the nucleus, see Figure 1.6, characterizes its state. Applying the momentum conservation law, the internal momentum $\vec{k}_3$ can be related to the recoil momentum $\vec{k}_{A-1}$ of the residual $(A-1)$ nucleus by

$$\vec{k}_{A-1} = \vec{k}_0 - \vec{k}_1 - \vec{k}_2 = -\vec{k}_3. \tag{1.6}$$

Here $\vec{k}_0$, $\vec{k}_1$ and $\vec{k}_2$ refer to the momentum of the incoming, the outgoing and ejected proton respectively. It is thus possible to determine the internal momentum either by measuring the recoil momentum of the spectator or by measuring the momenta of all three protons involved in the $(p, 2p)$ reaction.
Moreover, quasi-free scattering is an optimal tool to probe also deeply bound nucleons and to obtain cross sections on single orbitals by performing kinematically complete measurements. These cross sections give insight into the occupation probability of an orbital and into the assigned angular momentum, probing the shell model directly.
Here, the R^3B setup at FAIR will offer optimal conditions, as it allows kinematically complete measurements and the energy of the incoming particles lie well in the region where elastic scattering dominates the total cross section, as can be seen in Figure 1.7 and a reaction cross-section of up to $25\,\mathrm{mbar}$ can be expected [22].

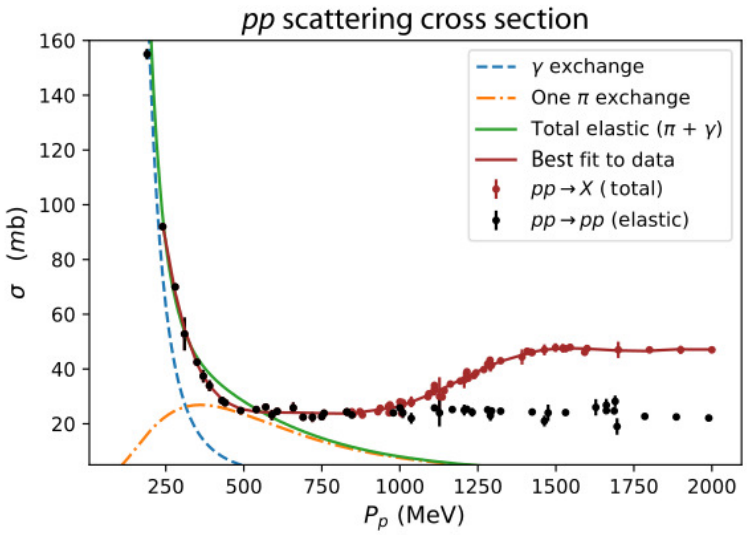

Figure 1.7.: Total and elastic cross sections for pp collisions exhibiting best quasi-free scattering conditions for beam energies under $1\,\mathrm{GeV}$, unrestricted use by [23].

2. CALIFA

The CALIFA calorimeter (**CAL**orimeter for the **I**n **F**light detection of γ rays and light charged p**A**rticles) is going to surround the entire reaction-target area and therefore forms a core detector of the kinematically complete measurement for R^3B. The detector array is divided into two parts, the Barrel section covering the angular range from $140.3°$ to $43.2°$ and the Endcap section covering the most forward angles from $43.2°$ down to $7°$. This angular coverage ensures the detection of $97.2\ \%$ γ rays in the range of $100\,\mathrm{keV} < E_\gamma < 30\,\mathrm{MeV}$ that are strongly focused in forward direction due to the Lorentz boost [24]. Besides γ rays, light charged particles, mostly protons of up to $700\,\mathrm{MeV}$, will also be measured.

2.1. Geometry

For conceptual reasons CALIFA is split into two sections, the Barrel covering backward angles and the Endcap in forward direction.

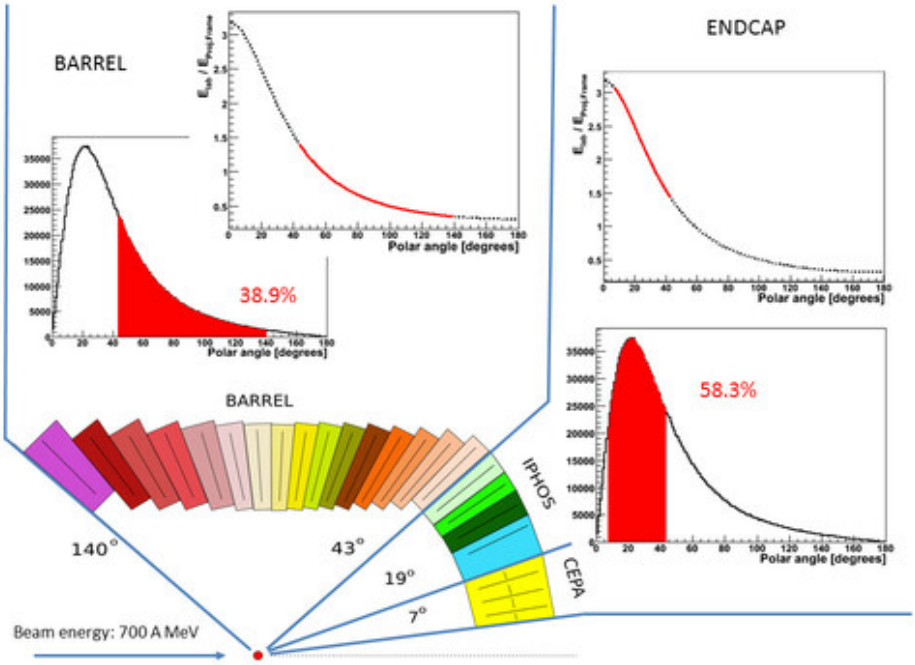

Figure 2.1.: Schematic representation of the CALIFA detector profile, where Barrel crystals can be located within an angular range from $140.3°$ down to $43.2°$ and the Iphos detectors in the angular range from $43.2°$ to $19°$ ©H. Alvarez Pol, FAIR/NUSTAR-Collaboration [24].

2.1.1. The CALIFA Barrel

The Barrel consists of 1952 CsI(Tl) scintillating crystals whose basic shape is an asymmetric frustum of pyramid. Due to the high velocity of the incoming beam of up to $1\,\mathrm{AGeV}$ the emitted photons are Doppler-shifted towards higher energies E_γ^L in laboratory frame (**L**) given by the Lorentz transformation

$$E_\gamma^L = \frac{E_\gamma^{PF}}{\gamma}\frac{1}{1-\beta\cos\theta}. \tag{2.1}$$

Here E_γ^{PF} is the energy of the γ ray in the **P**rojectile rest **F**rame, β the velocity of the projectile divided by the speed of light c, $\gamma = \frac{1}{\sqrt{1-\beta^2}}$ the Lorentz-factor and θ the emission angle. For larger angles the Lorentz boost reduces the energy of the γ rays, therefore a shorter version of the crystals is sufficient. For more forward angles the crystals need to be longer in order to stop charged particles stemming from the reaction area and to absorb Lorentz-boosted γ rays.
On the other hand, the length of the crystals is limited by the loss of efficiency in light collection, resulting in a drop in energy resolution. The reduction of energy resolution is a consequence of the light-collection process in the larger material volume. For a schematic representation of the different lengths of Barrel crystals and their angular coverage see Figure 2.1.

2.1.2. The Endcap

Iphos

The above described situation is even more complicated when going to more forward angles and closer to the beam line. Here the energy of scattered protons and light particles can be up to $E_{particle} = 700\ MeV$ and even higher. Also, the γ rays are strongly shifted to higher energies by the Lorentz boost. As shown in Figure 2.1 this results in three times higher γ-ray energies for the smallest angles.

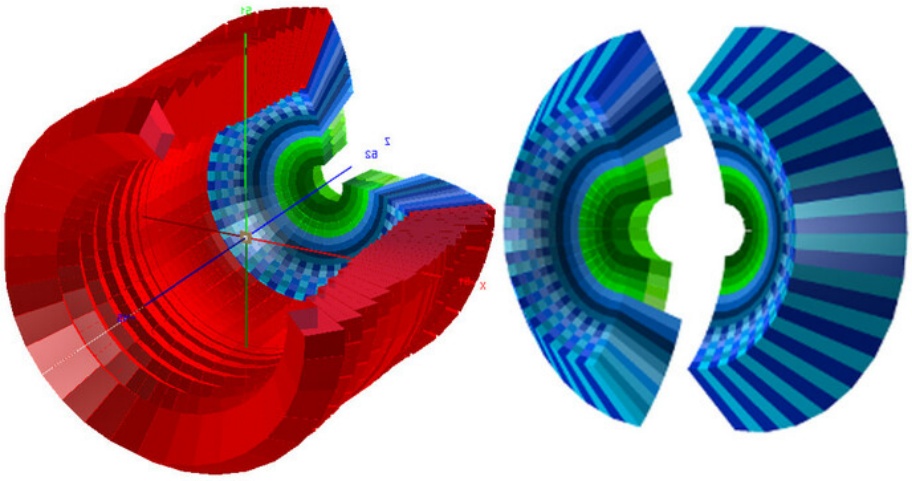

Figure 2.2.: Artistic view of the CALIFA calorimeter, that can be split into the Barrel part (red), the Iphos section (blue) and the CEPA ring (green) ©B. Heiss and M.Bendel, FAIR/NUSTAR-Collaboration [24].

In order to fully stop protons of $E_p = 700\,\mathrm{MeV}$ in CsI(Tl), a crystal length of $70\,\mathrm{cm}$ is needed. Such a long crystal however comes with the disadvantage of worse energy resolution in case of γ-ray detection

and consumes a lot of space, space that is scarce in front of the GLAD magnet. Due to these reasons as compromise between efficiency and energy resolution the crystal length of $22\,\mathrm{cm}$ was chosen. To perform the high-energy particle-identification and to reconstruct particle energies whenever the length of the crystal is not sufficient to stop the particle, TU München developed a particle identification method based on the two different intrinsic decay times of CsI(Tl), called **Q**uick **P**article **ID**entification (QPID) that will be used for the Endcap CsI(Tl) crystals [25] that are called Iphos crystals due to the fact that the reconstruction works according to an **i**ntrinsic **phos**wich concept.

Cepa

For the innermost rings of the Endcap the choice of CsI(Tl) is not sufficient. Due to the high count rates that are expected around the beam pipe and the very high γ-energies caused by the Doppler-shift, a faster detector is needed. As a solution, a combination of $LaBr_3$(Ce) and $LaCl_3$(Ce) that forms a phoswich detector in one single encapsulation called CEPA (**C**alifa **E**ndcap **P**hoswich **A**rray) is proposed. The read-out is realized by a **P**hoto **M**ultiplier **T**ube (PMT), that is resistant to magnetic fields like the stray field of the magnet and can cope with the expected high count rates in this region. The excellent time resolution of $LaBr_3$(Ce) and $LaCl_3$(Ce) is visible in their decay constants of $28\,\mathrm{ns}$ and $16\,\mathrm{ns}$ [26]. As a consequence of the difference in decay constants and the phoswich setup, it is possible to apply pulse-shape analysis and identify the measured particle.

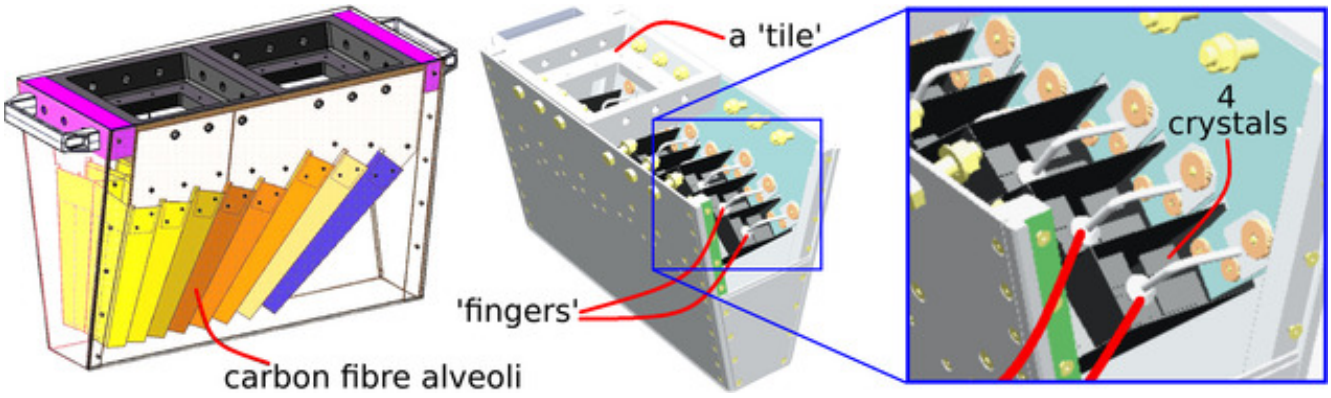

Figure 2.3.: Detailed insight into a CALIFA petal box, with the carbon fiber structure (left) and mounting fingers (right), courtesy of B.Pietras [27]

2.2. CALIFA setups

2.2.1. Standalone petal setups

For detector tests and benchmark experiments of the CALIFA detector array, 64 Barrel detectors that cover the angular range of $43° < \theta < 93°$ are mounted in one aluminum housing and form one CALIFA petal. In this aluminum box a carbon fiber structure is mounted that divides the volume into 16 alveoli pockets with a material thickness of just $200\,\mu\mathrm{m}$ ensuring low γ-ray absorption and low energy loss for protons [24], as displayed in Figure 2.3. These pockets are filled with four single detector modules of the same length. The most forward six pockets are filled with the longest of the crystals, having a length of $22\,\mathrm{cm}$. The six middle alveoli are filled with crystals of $18\,\mathrm{cm}$ length, leaving the $17\,\mathrm{cm}$ crystals for the four most backward pockets. Each CsI(Tl) crystal has the shape of a asymmetric truncated pyramid and is wrapped into a highly

reflective Vikuiti ESR foil [28] ensuring reflection of 98% of the scintillating light and is equipped with a **L**arge **A**rea **A**valanche **P**hoto **D**iode (LAAPD). To ensure a fixation inside the pockets, metal fingers are used to hold the crystals deep in the alveoli. The lid of the box, called tile, ensures a lighttight environment for the detectors and offers a feedthrough for the preamplifiers.

With this compact setup detector tests were performed in the lab by the CALIFA collaboration, like the investigation of the detector response, for details see [29]. Moreover, test experiments at beam facilities have been conducted to confirm the components' performance, see [27], or to carry out first benchmark experiments. One of these was done in Kraków in 2017 and will be discussed in more detail in Chapter 4.

2.2.2. CALIFA demonstrator

A first milestone on the way to a full CALIFA array was the CALIFA demonstrator that held seven CALIFA petals whereby four of them were mounted in two double petal boxes as shown in Figure 2.4. During the experiments at GSI in 2018 the demonstrator was successfully used to detect protons and light-charged particles with four petals operated in low gain mode and to measure γ rays in the remaining three petals.

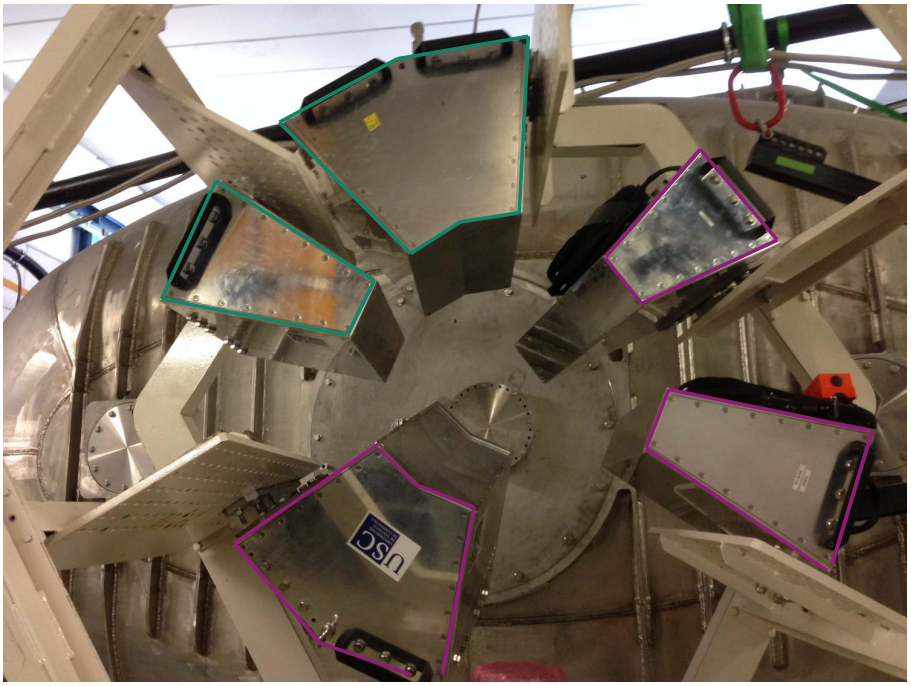

Figure 2.4.: Upstream view on the CALIFA demonstrator equipped with 7 Barrel petals, three (green) operated in high-gain mode and five (magenta) operated in low-gain mode.

2.2.3. CALIFA phase-0 setup

The summit of the CALIFA buildup so far was reached in the beginning of 2021 when the final CALIFA mechanical structure was equipped with 1264 CALIFA crystals, see Figure 2.5. Here, the Iphos part of the Endcap, counting 480 channels, was assembled with 360 detectors as well as the entire forward Barrel section, counting 904 channels. The angular range from $19^\circ < \theta < 93^\circ$ was covered for the phase-0 experiments that were conducted in the first half of the year.

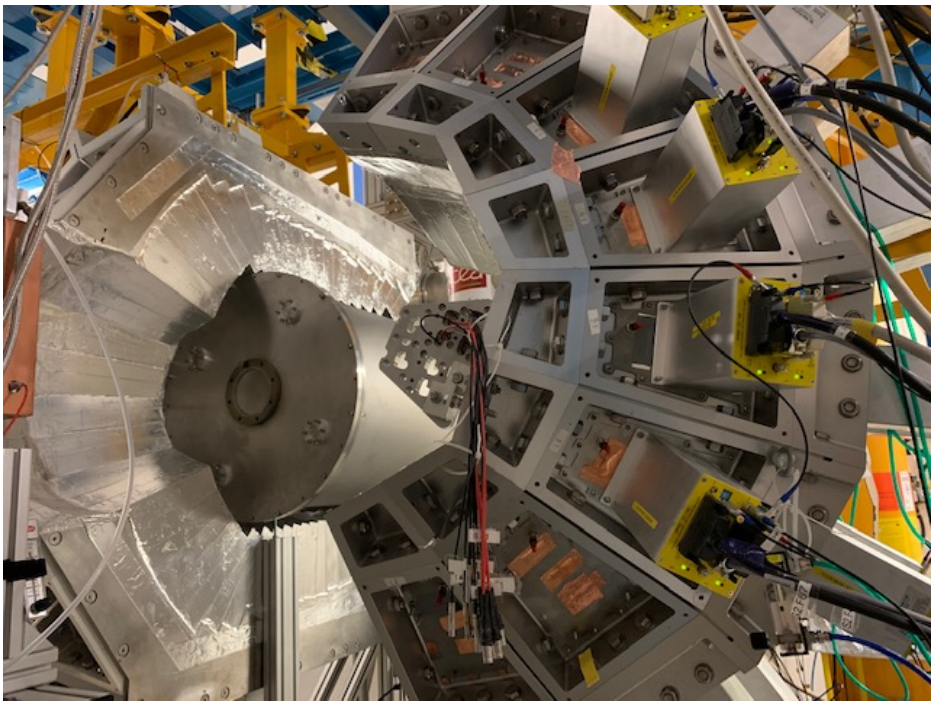

Figure 2.5.: Half-open CALIFA array of the phase-0 setup enabling an upstream view onto the target chamber and the Barrel section of CALIFA. The prominent ring structure on the right side of the picture shows half of the Iphos section with its read-out.

2.3. CALIFA components

2.3.1. CsI(Tl)

The scintillating material for CALIFA has to meet several requirements, namely:

- good energy resolution and high light output
- scintillating light matching read-out unit
- high stopping power for charged particles
- variety of shapes and mechanical stability

The chosen material CsI(Tl) provides an intrinsic energy resolution of $\frac{\Delta E}{E} \leq 4.9\ \%$ when coupled to an **A**valanche **P**hoto **D**iode (APD) and measured with γ rays of $662\,\mathrm{keV}$ [30] and a light yield of $54\,000\ \frac{\mathrm{photons}}{\mathrm{MeV}}$ at room temperature [31]. The wavelength of the scintillating light ranges from $400\,\mathrm{nm}$ to $560\,\mathrm{nm}$ [31].The composition of the inorganic scintillating material and its density of $4.5\ \frac{\mathrm{g}}{\mathrm{cm}^3}$ ensure a high stopping power for charged particles such as protons and provide a relatively high detection efficiency for γ rays in the range of $0.1 - 15\,\mathrm{MeV}$.
Moreover, CsI(Tl) can be produced in diverse shapes and sizes while it does not need an encapsulation due to its comparatively low hygroscopicity, a faint flow of nitrogen is enough to create a sufficiently dry environment. Thus the inorganic scintillator CsI(Tl) meets all requirements.
In addition, the scintillating process inside the crystal is mainly based on two decay components, a fast $\tau_f = 0.68\,\mu\mathrm{s}$ and a slow $\tau_s = 3.34\,\mu\mathrm{s}$ one [31]. The ratio of slow and fast component depends on the

ionization density that is different for different impinging particles or radiation. Using this fingerprint particles can be identified by applying pulse-shape analysis. For this particle identification a method was developed by the CALIFA group of TU München that is explained in detail in Chapter 2.3.5.

2.3.2. Photosensors

The scintillating light of the CsI(Tl) crystal needs to be transformed into an electronic signal that can be amplified and processed by the data acquisition. The photosensor of choice should comply with the spacial requirements of the detector array and its position in front of the dipole magnet GLAD that has a very strong magnetic fringe-field. Moreover, it is supposed to cover a wide dynamic range, enabling the array to detect γ rays from $0.1\,\mathrm{MeV}$ up to protons of several hundreds of MeV. Notwithstanding the above, the photosensor has to perform well in terms of quantum efficiency, time response and gain stability.
In order to meet the above described requirements, Hamamatsu developed a **L**arge **A**rea **A**valanche **P**hoto **D**iode (LAAPD) that covers $10 \times 20\,\mathrm{mm}^2$ of active surface and is casted in ceramic, Hamamatsu S12102 [32]. In principle a LAAPD is similar to a standard photo diode but it contains an additional highly doted p-layer that forms a region of very high field strength. The functional principle is shown in Figure 2.6 and the resulting multiplication factor M is defined as

$$M = \frac{1}{1 - \int_0^L \alpha(x)dx} \tag{2.2}$$

with the space-charge boundary L for electrons and α the multiplication coefficient for electrons α.

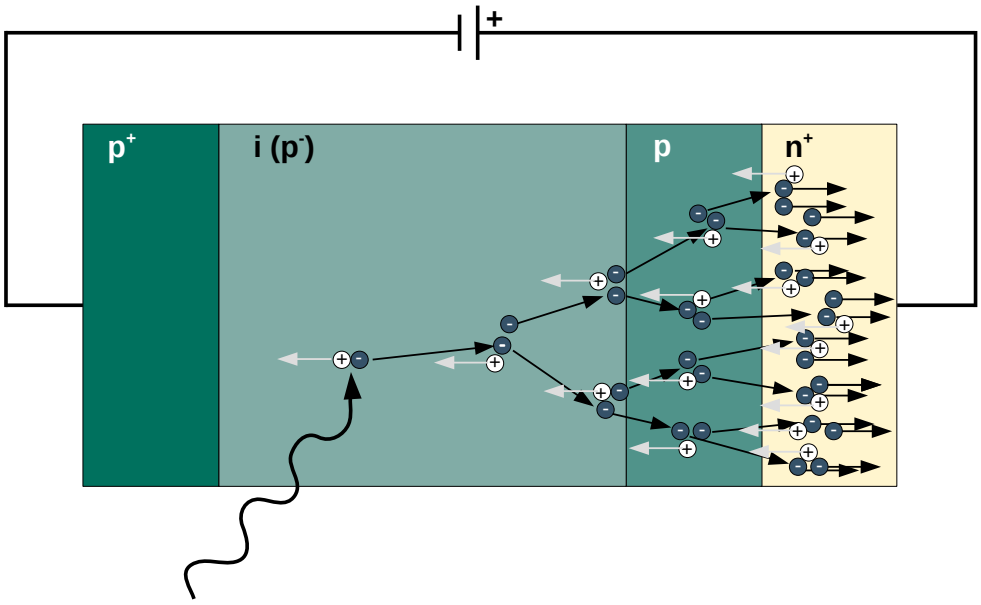

Figure 2.6.: Functional principle of an LAAPD.

These LAAPDs fit perfectly to the chosen scintillating material with a quantum efficiency of 85% for the CsI(Tl) emission spectrum and provide a linear light response in the range from $400\,\mathrm{nm}$ to $800\,\mathrm{nm}$ [24].

They have an internal gain of $40 - 50$ in the bias-voltage region of interest, depending strongly on the applied voltage and the operating temperature. This dependency can be compensated with monitoring the temperature and adjusting the applied voltage, like shown in Figure 3.2. For this purpose mesytec [1] developed the charge-sensitive preamplifier MPRB-32 [33] that is capable of compensating the temperature-dependent gain-drifts by readjusting the bias voltages while in general providing high voltage for 32 LAAPDs and offering two different sensitivities due to capacitors of $30\,\mathrm{pC}$ for $30\,\mathrm{MeV}$ and capacitors of $3\,\mathrm{pC}$ for $300\,\mathrm{MeV}$.

2.3.3. Read-out

The preamplified signal of the LAAPD is subsequently processed in the modern digital data acquisition system developed for CALIFA based on MBS (**M**ulti **B**ranch **S**ystem) and GOSIP (**G**igabit **O**ptical **S**erial **I**nterface **P**rotocol). Core of the entire DAQ is the FEBEX 3b (**F**ront **E**nd **B**oard with optical link **EX**tension), a compact digitiser board offering 16 ADC channels that sample the analog input signal with a sampling rate of $50\,\mathrm{MHz}$, a resolution of $14\,\mathrm{bit}$ and a serial multi-gigabit connection of $2\,\mathrm{Gbits/s}$. The data is then processed by a Lattice ECP3-150 FPGA (**F**ield **P**rogrammable **G**ate **A**rray) offering 150k LUTs (**L**ook **U**p **T**ables), sufficient for very sophisticated firmwares, dedicated hardware multipliers, memory cells and built-in high speed I/O standards.
Auxiliary electronics may be plugged onto the FEBEX 3B via a high density extension connector carrying the 16 differential analog inputs to the ADC channels and 16 general purpose LVDS I/Os (**L**ow **V**oltage **D**ifferential **S**ignaling). Via a PCIe (**P**eripheral **C**omponent **I**nterconnect **e**xpress) like connector, the FEBEX 3B boards are plugged into the 19 inch create.
For CALIFA the FEBEX 3b is used for pulse generation and trigger processing, but particularly as digitiser with integrated realtime pulse-shape analysis. Therefore, a FAB (**F**EBEX **A**dd-on **B**oard) was developed by TU München that contains individual **D**igital to **A**nalog **C**onverters (DAC) to apply DC offsets to each channel and ensures proper Nyquist filtering for later digitization of the signal, for more details see [25].

2.3.4. Gain-monitoring system

In order to continuously monitor the functionality of its components, CALIFA will be equipped with a light monitoring and calibration system. During an experiment the gain of each detector channel, namely crystal, readout and the electronics, may shift. This is an unfortunate behavior complicating further analysis steps. Hence it is an advantage to monitor the gain and enabling a correction of the shift in the aftermath.
The CALIFA gain-monitoring system consists of three main components

- LED-based light source providing a well-defined input to the crystal
- optical-fiber transport-system distributing the LED light to the crystals
- reference system to monitor the stability of the LED light-source

that are partly displayed in Figure 2.7. The well-defined LED light is transported to the crystal via a plastic optical-fiber and can be processed inside the crystal like a γ ray due to the fitting LED-wavelength. A signal is produced in the readout chain of the detector and can be compared to the signal produced in the reference system. Therefore, occuring gain shifts can be identified and either directly corrected or later compensated in the offline analysis.

[1] www.mesytec.de, mesytec GmbH & Co. KG, Wernher-von-Braun-Str. 1, 85640 Putzbrunn, Germany

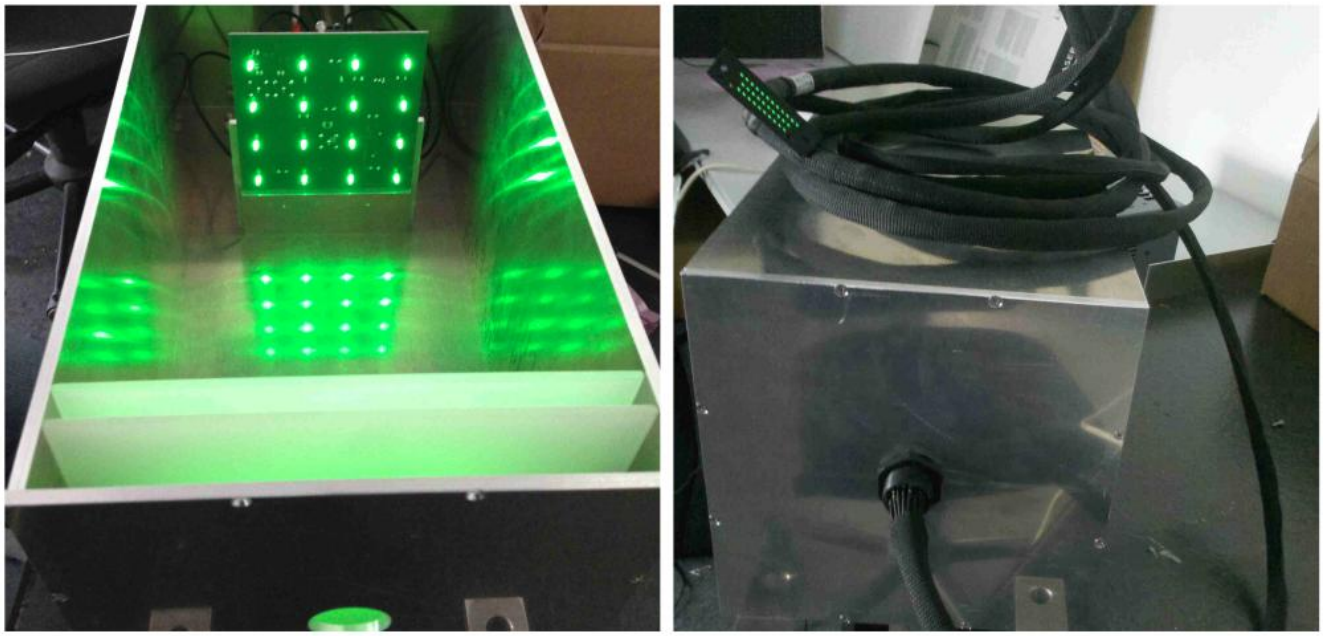

Figure 2.7.: LED source of the gain-monitoring system and the prototype of the optical-fiber transport-system ©A.Ignatov, FAIR/NUSTAR-Collaboration [24].

2.3.5. Particle identification

As mentioned before, CsI(Tl) is a good material to identify particles by pulse-shape analysis. Such an identification is based on different decay times of the scintillating processes inside the inorganic scintillator. In CsI(Tl) the scintillation is based on three scintillation components a rapid $\tau_\mathrm{r} \approx 30\,\mathrm{ns}$, a fast $\tau_\mathrm{f} \approx 700\,\mathrm{ns}$ and a slow $\tau_\mathrm{s} \approx 3.34\,\mu\mathrm{s}$ [31] component. The rapid decay can be neclected due to the fact that its decay time is much shorter than the fast and slow decay times. So the luminescence function $L(t)$ for CsI(Tl) can be expressed as

$$L(t) = \frac{N_f}{\tau_f} e^{-\frac{t}{\tau_f}} + \frac{N_s}{\tau_s} e^{-\frac{t}{\tau_s}}. \tag{2.3}$$

In order to get the fingerprint of the incident radiation it is necessary to extract the light amplitudes N_f and N_s from the luminescence function because they depend on the ionization density. This can be done by pulse-shape analysis, implemented in the CALIFA firmware that has been developed by TU München and is explained in the following. For a more detailed picture the PhD Thesis of M.Winkel [25] may be recommended.

Baseline Reconstruction and Moving Averaging Unit

A first step of the pulse-shape analysis is reconstructing the baseline. Due to low frequency noise the baseline is shifting to different offsets and thus is distorting the trace. By calculating a moving average before and after the actual trace and subtracting it, one can restore the baseline. For low event rates this can be done for each event uniquely, but for higher rates it has to be done at the beginning of the measurement under the assumption that the variation of the baseline can be neglected.
For smoothing out high frequency noise a **M**oving **A**verage **U**nit (MAU) is used. By moving a small window

over the trace and averaging the trace's amplitude, distortions from high frequency noise can be smoothed out as long as the window is not too wide.

Moving Window Deconvolution

The signal of the CsI(Tl) crystal is preamplified before being processed by the DAQ. The preamplifier itself has an exponential decay with a decay time $\tau_{preamp} = 50\,\mu$s. This leads to pileups whenever a trace is not entirely processed before the next signal arrives or to a ballistic deficit due to the continuously discharging of the preamplifier's capacitors. For this reason it is necessary to deconvolute the preamplifier decay from the raw trace. This can be achieved by a **M**oving **W**indow **D**econvolution (MWD) where a window of fixed length L is moved over the raw trace. As the preamplifier deconvolutes the signal with a single exponential function, the MWD can be described as

$$Q(t) = U(t) - U(t-L) + \frac{1}{\tau_{preamp}} \sum_{t'=t-L}^{t} U(t'), \tag{2.4}$$

where $Q(t)$ describes the convoluted and $U(t)$ the raw signal and τ_{preamp} is given in units of the sampling interval t_s. Inside the window the charge can be integrated and will have its maximum when the window of length L overlaps with the entire raw trace. Hence the ballistic deficit is identified and corrected and the probability of pileups is reduced.

Quick Particle Identification

In order to identify the incident particle, an integration of the photo current within two windows is necessary. A short window directly follows the trigger signal and the larger window is delayed so that the first window is dominated by the fast component whilst the second is dominated by the slow component. The **Q**uick **P**article **ID**entification (QPID) is based on this method and was developed by Max Winkel (TU München) [25].

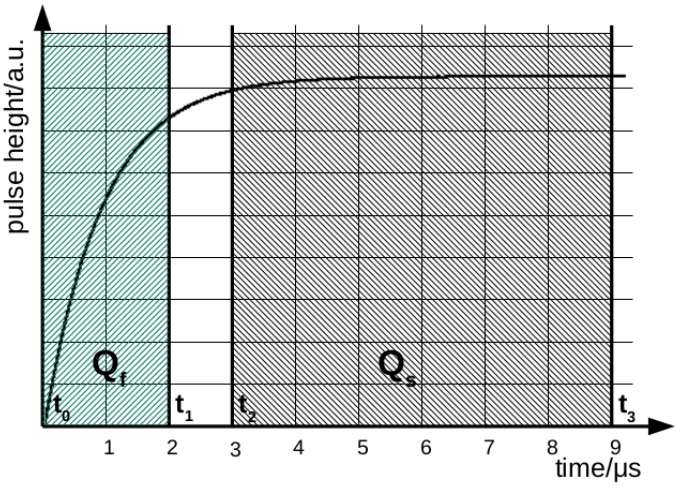

Figure 2.8.: Exemplary charge function $Q(t)$ and the corresponding windows Q_f and Q_s.

The smoothened and deconvoluted signal can be described by the smoothened charge functions

$$F_1(t) = \frac{1}{T}\int_0^t Q(t')dt' = \frac{N_f}{T}[t + \tau_f(e^{-\frac{t}{\tau_f}} - 1)] + \frac{N_s}{T}[t + \tau_s(e^{-\frac{t}{\tau_s}} - 1)] \tag{2.5}$$

$$F_2(t) = \frac{1}{T}\int_{t-T}^{T} Q(t')dt' = N_f[1 - \frac{\tau_f}{T}(e^{-\frac{T}{\tau_f}} - 1)e^{-\frac{t}{\tau_f}}] - N_s[\frac{\tau_s}{T}(e^{\frac{T}{\tau_s}} - 1)e^{-\frac{t}{\tau_s}}] \tag{2.6}$$

where $Q(t)$ describes the integrated charge in the time window $[0, t]$ and T the window size of the MAU. The smoothened charge function $F(t)$ is split into two time intervals namely $[t_0, t_1]$ and $[t_2, t_3]$. The integrated charge $Q(t)$ within each interval is connected to the fast N_f and the slow N_s component via

$$\begin{pmatrix} Q_f \\ Q_s \end{pmatrix} = \begin{pmatrix} F(t_1) - F(t_0) \\ F(t_3) - F(t_2) \end{pmatrix} = \begin{pmatrix} A & B \\ C & D \end{pmatrix} \cdot \begin{pmatrix} N_f \\ N_s \end{pmatrix}. \tag{2.7}$$

This equation can be inverted to

$$\begin{pmatrix} N_f \\ N_s \end{pmatrix} = \frac{1}{AD - BC}\begin{pmatrix} D & -B \\ -C & A \end{pmatrix} \cdot \begin{pmatrix} Q_f \\ Q_s \end{pmatrix} \tag{2.8}$$

in order to derive the slow and fast component. According to [25] a proper choice of t_i leads to $A, B = 1$ and $C, D = 0$ resulting in an independence of $N_f(N_s)$ from $Q_s(Q_f)$.

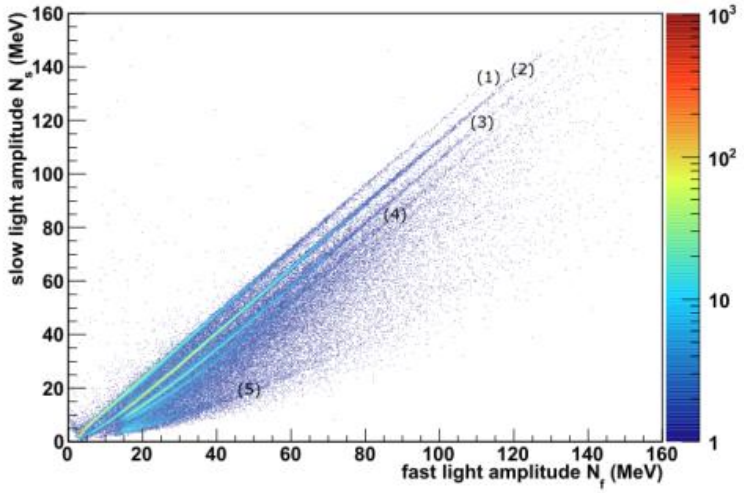

Figure 2.9.: CsI(Tl) crystal irratiated with neutrons revealing (1) the γ and stopped proton branch and branches for (2) fully stopped protons, (3) deuterons, (4) tritons and (5) helium nuclei, taken with permission from [34].

Figure 2.9 gives an example for the particle identification of a CsI(Tl) crystal that detects γ rays and punched-through light particles (1), stopped protons (2), deuterons (3), tritons (4) and heavier particles (5). On the right side of Figure 2.9 it is challenging to separate and identify particles due to the closeness of the branches. Hence, another step is necessary in order to reliably identify the detected particles. A clearer picture can be achieved by fitting the slope α of the γ-ray branch and turn the entire QPID-plot clockwise by this angle as can be described by:

$$\begin{pmatrix} N_{f,red} \\ N_{s,red} \end{pmatrix} = \begin{pmatrix} \cos\alpha & -\sin\alpha \\ \sin\alpha & \cos\alpha \end{pmatrix} \begin{pmatrix} N_f \\ N_s \end{pmatrix} \tag{2.9}$$

The resulting plot, as displayed in Figure 2.10, gives a more detailed picture of the particle branches and allows for an identification of the whole set of detected particles.

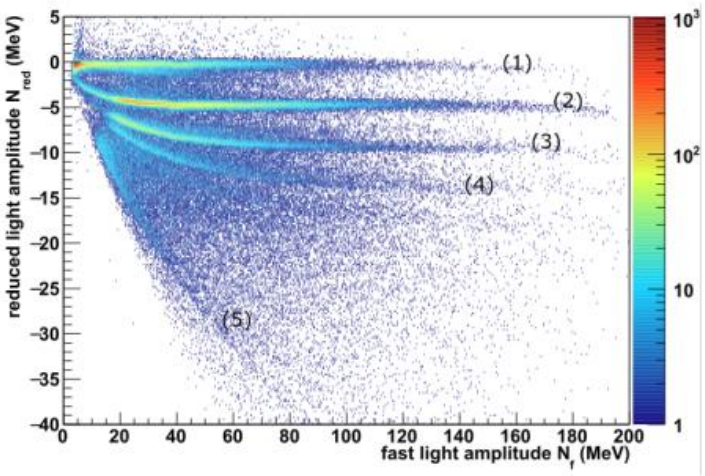

Figure 2.10.: Reduced representation of the PID plot of CsI(Tl) irradiated with neutron. The particle branches are better separable, with the same numbering as in Figure 2.9, taken with permission from [34].

3. Detector

On the way to the final calorimeter, a lot of assembling steps, tests and quality assurance procedures have to be fulfilled in order to provide the basic components of the CALIFA array while matching the requirements. In the following sections the assembly of 120 Endcap detector-units, analogous to the Barrel detectors, and their testing is described. After that the equipping of two Endcap segments with the 120 CsI(Tl) crystals will be explained and the quality of these two parts of the Endcap will be examined.

3.0.1. Assembling of single channels

Quality assurance of CsI(Tl) crystals

The core of each channel of CALIFA is the CsI(Tl) crystal that is produced by Amcrys [1] in various different geometries, as summarized in Table 3.1. To match the requirements, the manufacturer checks if the resolution of the crystal is better than 9 % when coupled to a standard photomultiplier tube (PMT) and irradiated with $661\,\mathrm{keV}$, stemming from a ^{137}Cs source. Moreover, a central scan along the main axis of the crystal in steps of $2\,\mathrm{cm}$ is done to ensure the linearity of the light output. Without any surface treatment the light output of the crystal would vary with the position of the impinging radiation. To overcome this issue, Amcrys applies lapping to the surfaces, see Fig. 3.1, thus improving the linearity.

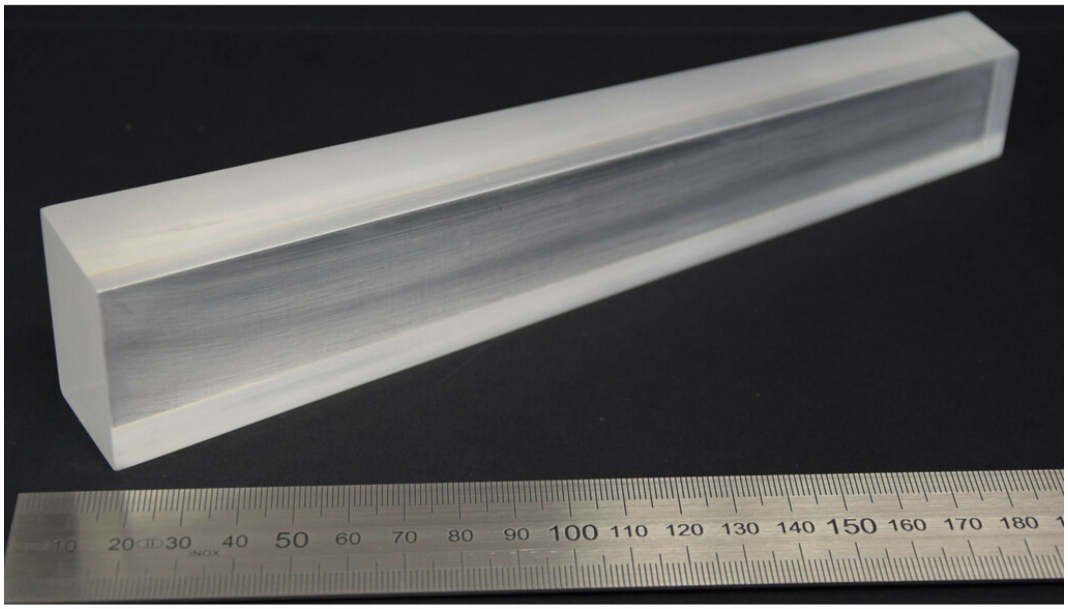

Figure 3.1.: Unpacked raw Iphos crystal of shape 1213 as received from the manufacturer.

[1] Amcrys, Lenina Ave 60, Kharkiv 61072, Ukraine

Front view	Type	Front		Exit		Length/mm	Weight/kg
		Width/mm	Height/mm	Width/mm	Height/mm		
Iphos							
	1233 1234	35.1/38.6 38.6/41.8	19.8 18.7	53.7/59.0 59.0/63.9	30.1 28.7	219.7 219.7	1.17 1.21
	1221/24 1222/23	19.0/27.9 28/30.8	35.0 35.1	38.8/51.8 51.9/56.0	53.6 53.6	219.7 219.6	1.44 1.71
	1205/6 1207/8 1209/10 1211/12 1213/14 1215/16	21.0/22.5 22.5/23.5 24.0/25.3 25.3/26.7 26.7/28.0 28.0/19.2	18.1 17.7 17.4 17.4 18.1 15.5	32.0/34.3 34.3/36.5 36.6/38.6 38.6/40.7 40.7/42.7 42.7/44.5	27.7 26.6 26.6 26.6 27.7 23.7	219.7 219.7 219.6 219.6 219.5 219.5	0.63 0.65 0.69 0.73 0.80 0.71
Barrel							
	1101/2 1103/4 1105/6	29.2 29.3 29.3	15.3 15.3 15.3	44.6 44.6 45.5	15.3 15.3 15.3	220 180 170	0.76 0.59 0.56
	1113/14	29.1/30.0	15.1	45.9/47.3	24.7	220	0.78

Table 3.1.: Summary of the different crystal geometries needed for Iphos and the CALIFA forward Barrel.

When the crystals arrive at our laboratory, they need to be taken out of their vacuum packing and need to be checked for surface damages or smashes on edges and corners. Also a look into the crystal is mandatory in order to locate air bubbles or any other possible inclusion that might disturb the light-collection process. When a crystal meets the standards as listed in Table 3.2, that were agreed on with the producer, the CsI(Tl) crystal will be equipped with its read-out device.

Size of inclusions	Acceptable number of defined inclusions
up to $0.3\,\mathrm{mm}$	not specified
$0.3\,\mathrm{mm} - 0.7\,\mathrm{mm}$	6
$0.7\,\mathrm{mm} - 0.9\,\mathrm{mm}$	2
$> 0.9\,\mathrm{mm}$	not allowed

Table 3.2.: Specification of allowed inclusions.

Quality assurance of the LAAPDs

The specially designed LAAPDs Hamamatsu S12102 [32] have an effective area of $10 \times 20\,\mathrm{mm}^2$ and are mounted on a ceramic plate. Each LAAPD needs to be characterized separately. This is due to the fact that

they show an individual sensitivity to temperature and bias-voltage changes. Therefore a dedicated APD test stand has been developed at TU Darmstadt that provides a stable light source and controllable temperature conditions. Additionally, it allows to scan through different bias-voltages and temperature settings in order to get the characteristic gain curve of each LAAPD and its behavior under slight temperature changes, as exemplary shown for a standard LAAPD in Figure 3.2 and can be found in details in [29]. With the help of these gain curves and the temperature coefficients possible shifts in temperature can be compensated by adjusting the bias voltage and thus the gain can be steadied. Moreover, the scan serves as a general quality assurance test for all LAAPDs arriving at our laboratory.

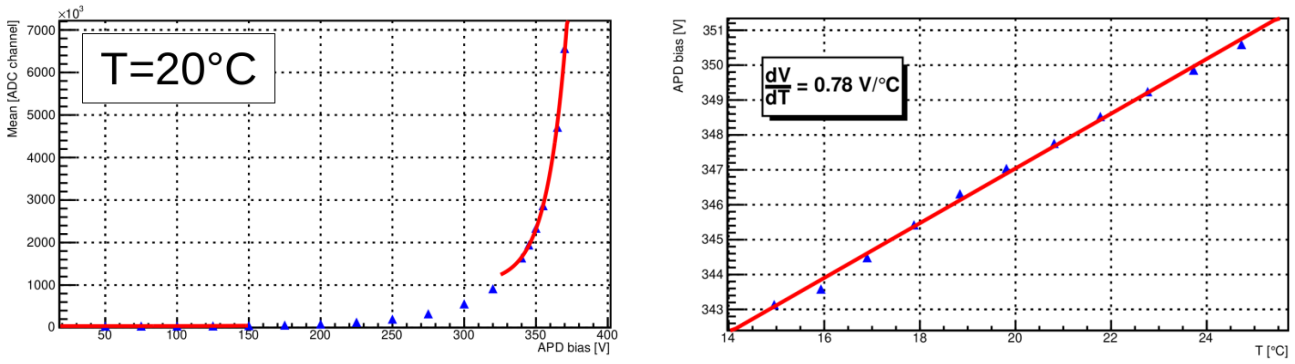

(a) Voltage-dependent gain curve.

(b) Temperature coefficient for gain=50.

Figure 3.2.: Dependence of the LAAPD gain on the increasing bias-voltage that can be described as a plateau followed by an exponential rise when approaching the break-down voltage (a). The temperature-coefficient for the constant gain=50 showing the necessary increase in bias-voltage to compensate temperature changes (b).

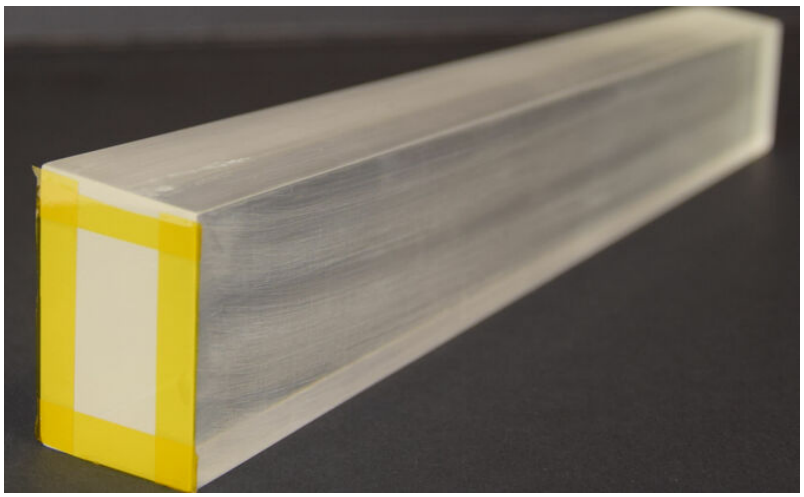

Figure 3.3.: Checked and with ethanol cleaned crystal with already applied Kapton® window, marking the bonding surface for the LAAPD.

Attaching the LAAPD

The read-out unit of the scintillator is attached on its broader end, in the center of gravity of the surface. In order to position the LAAPD correctly, the area is marked with Kapton® tape as shown in Fig. 3.3. This material can be removed easily and also prevents the cement from spreading over the crystal's surface. A thorough cleaning of the surface is performed using ethanol on lint-free precision wipes. After the crystal has been set up for attaching the LAAPD, an appropriate glue needs to be chosen and prepared. Throughout the last decade of CALIFA research and development various products out of two main groups of glue have been used, namely optical grease and optical cement. While optical grease has the advantage of removability, optical cement most of the time forms a final conjunction. In connection with a crystal, different performance of light output and non-uniformity in the light output was observed and described in detail in [35]. As a result of these studies as well as of measurements and investigations performed in our institute, the choice was to keep the optical cement EJ-500 by Eljen Technologies [2] as it gave the best results in terms of light output and non-uniformity and thus fulfills the requirements.
The chosen optical cement EJ-500 is a two-component cement, where resin and hardener need to be mixed in defined ratios at room temperature. A clear recommendation at this point is to measure the shares according to weight and not to volume as experience shows a better durability of the connection. The two components are perfectly mixed by spreading one component with a spatula into the other and by repeating this movement for a minute. The advantage of this procedure is a minimum of air bubbles forming within the cement. Anyhow, after mixing the optical cement needs half an hour rest in order to let air diffuse out of the glue. As guaranteed by the manufacturer [36] the optical cement has a working life of 60 minutes where it can be applied without drying out.

(a) Standard LAAPD. (b) Optical cement EJ-500.

Figure 3.4.: (a) Standard LAAPD as developed by Hamamatsu and used by the CALIFA collaboration. (b) Optical cement EJ-500 that showed best results during assembling of Barrel crystals and was chosen for glueing of Iphos detectors.

The last step before applying the optical cement is to thoroughly clean both the crystal's and LAAPD's surface with ethanol and letting it dry. The cement is now spread onto the LAAPDs' surface by using a metal spatula. Only a thin film in the order of $0.1\,\mathrm{mm}$ of glue is needed to form a strong conjunction

[2] ELJEN TECHNOLOGY, 1300 W. Broadway, Sweetwater, TX 79556, USA

with the crystal. If the layer is too thick, it oozes out around the LAAPD and inhibits a tight fitting of the reflective-foil wrapping. Moreover, the probability for the inclusion of air as well as for negative effects on the light propagation due to a reduced transmission increases. On the other hand, if the layer is too thin, the conjunction forms weakly so that LAAPD may fall of or covers part of the LAAPDs surface only. However, the overall performance of crystals with partially glued LAAPDs is surprisingly not worse than the average. As experience shows, fallen off LAAPDs can be reglued using EJ-500 without polishing the old layer of optical cement of the surface. In the very rare cases in which this had to be done, the obtained properties were not worse compared to the average values for non-reprocessed APDs. Anyhow, the best way is to directly apply a continuous thin film of glue and pressing the LAAPD onto the marked area of the crystal's surface while the crystal is held in an upright position, best achieved by a foam fixture as shown in Figure 3.5.

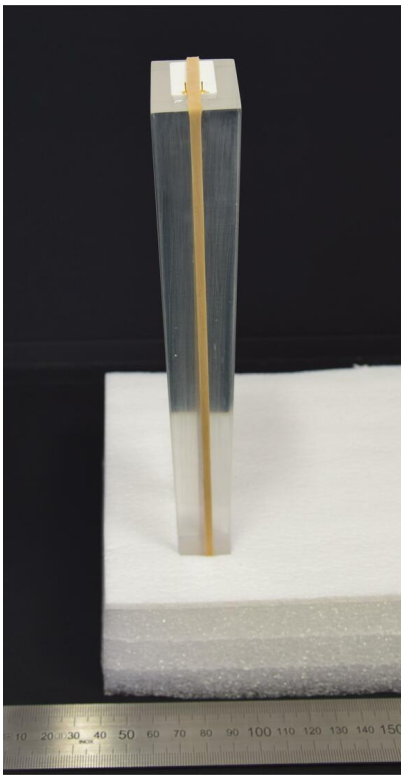

Figure 3.5.: Detector held upright in a foam fixture in order to prevent sliding of the LAAPD for as long as the optical cement needs to harden.

By putting the LAAPD down starting from one small edge up to the entire surface, one may press possible air bubbles out of the optical cement. After the positioning of the LAAPD, more pressure can be applied by bare hands and a customary rubber band is used to keep both the correct position and pressure like shown in Figure3.6. Afterwards it is advisable to visually inspect the crystal from the opposite side because air and bad conjunction are normally visible already at this stage. If any faults are noticed, there are three possible measures:

- Applying more pressure in order to enhance the adhesion.
- Slightly moving the LAAPD to get rid of bubbles and increase adhesion.
- Taking off the LAAPD, cleaning both crystal and LAAPD, and finally restarting the procedure.

If the conjunction looks fine, it is advisable to check it again after 2 to 4 hours of drying because slight movements of the LAAPD, that need to be corrected, are possible. Additionally, the adhesion might weaken which demands more pressure or reglueing. After 24 hours the glue is hardened and both rubber band and Kapton® tape can be removed. The crystal can be kept in lying position hereafter.

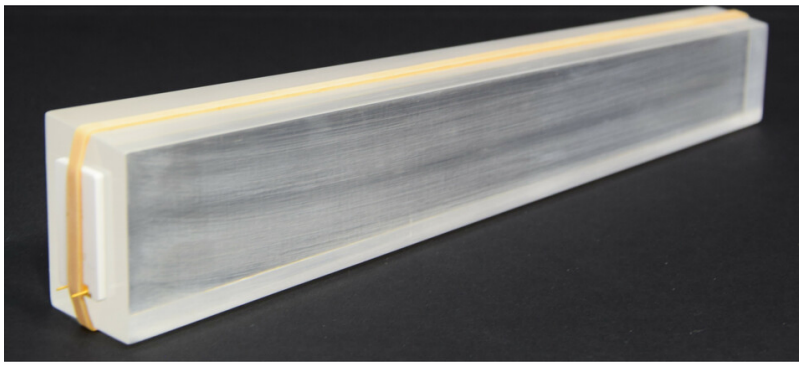

Figure 3.6.: Detector during dry process with attached rubber band to support the adhesion. Unlike shown, the detector is held in an upright position for half a day to avoid slipping of the LAAPD.

In a final step the reflective wrapping is attached. The material of choice is Vikuiti^{TM} Enhanced Specular Reflector (ESR) foil that provides an excellent reflectivity of more than 98% [28]. The thickness of $65\,\mu\mathrm{m}$ of the foil makes a tight fitting around the crystal possible. Three pieces are cut out of the reflector sheet by laser, namely one for the shell surface, one for the entrance window and another one for the exit window where the position of the LAAPD is left open. As visible in Figure 3.7, the shell-surface part is prefolded by the provider of the cutting. This eases the wrapping process around the crystal but the usage of prefolded foils is not strictly necessary as in former wrapping cycles non-prefolded material was succesfully used at TU Darmstadt. The advantage of this measure is the tightest achievable fitting, leaving nearly no air between the crystal and its wrapping, and therefore an optimum positioning within the carbon pockets at a later point. However, this may come at the price of losing photons at the edges of the crystal because in the crease line the material is so thin that the reflectivity decreases.

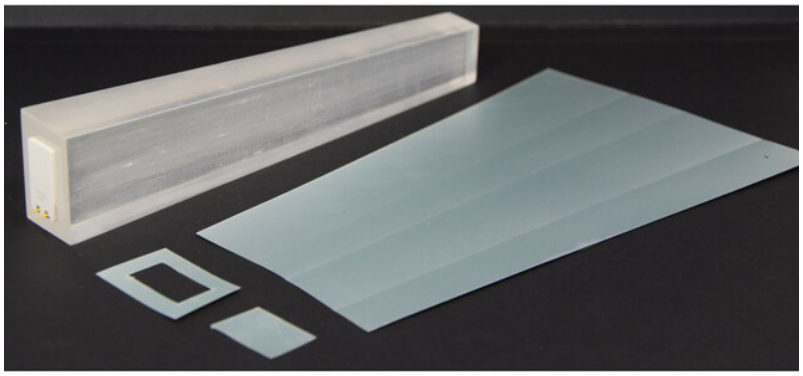

Figure 3.7.: Raw crystal with attached LAAPD and reflective wrapping. The shell-surface piece is pre-folded and the exit and entrance window are individual parts to enhance the fit accuracy.

Starting point of the foil wrapping procedure is the shell surface piece that needs to be wrapped around

the crystal as tight as possible and has to be fixed with 6 to 8 straps of Kapton® along the crystal's main axis. The gap between the two cutting edges of the reflector can be closed by using a silver polyester tape that is easily foldable and thin, with its crucial high reflectivity and low water vapour permeability [37]. In order to achieve an as tight as possible fitting, the reflector foil can be wrapped around the crystal with the crystal sticking $3 - 5\,\mathrm{mm}$ out at the LAAPD side. After fixing the reflector with Kapton®tape, the crystal has to be pressed into the reflector pocket until it lies flush at the entrance and exit window. The reflector pieces for entrance and exit window are then added and all gaps are closed with the polyester tape. Also the gap between the LAAPD and the reflector foils needs to be covered as photons might escape and humidity may enter and damage the crystal. Important at this point is to leave an opening where the light guide of the light calibration system will be attached to the completed detector, as can be seen in Figure 3.8. For a more detailed description of this step, see Appendix A.

Figure 3.8.: Assembled detector unit with light tight silver taping along the gaps. The blue tag provides information on the crystal's shape and its identification number and together with the serial number of the LAAPD ensures the unique identification of the detector.

3.0.2. Quality assurance of the single channels with the LUND crystal scanner

The goal for CALIFA is an energy resolution of 7 % at $1\,\mathrm{MeV}$ or better per crystal. Besides the characteristics of the material CsI(Tl), there are several properties of each individual crystal and of the read-out chain that rule the performance, namely

- Doping concentration and inclusions
- Light output non-uniformity
- Choice of photosensor and its connection
- (Noise of) readout electronics

Together with the supplier, the CALIFA working group agreed on a doping concentration of $0.08\,\mathrm{mol}\%$ that minimizes effects on the linearity [38]. There is also a well defined number and classification on inclusions that are acceptable when receiving the detector, as listed in Table 3.2.

Another measure that has a huge impact on the performance of a detector channel is the **l**ight **o**utput **n**on-**u**niformity (LONU) that can be observed when irradiating the crystal at different positions along its main axis. In doing so, a decrease in light yield is observed when approaching the LAAPD side of the

crystal. In order to quantify this observation, the LONU can be defined as

$$\Delta LO = \frac{(C_{max} - C_{min})}{\frac{1}{N}\sum_{i=1}^{N} C_i} \times 100\%, \tag{3.1}$$

where N is the number of measuring points and C_{min} and C_{max} the smallest and highest centroid position of the photopeak at a measuring point [39]. Experience shows that a high LONU impacts the energy resolution more than the individual light yield of a crystal [39]. Therefore each crystal undergoes a special lapping procedure where all shell surfaces are polished with zinc-oxide powder and ethylene glycol in order to minimize differences in the light output.

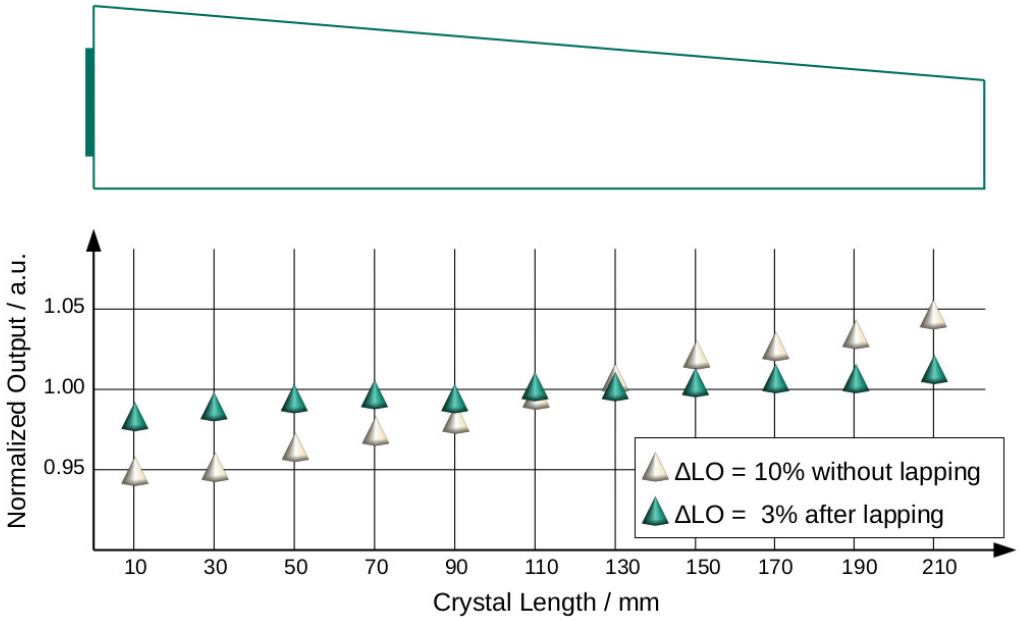

Figure 3.9.: Exemplary LONU of a CALIFA crystal depending on the position of the measurement. For an untreated crystal the light output increases with increasing distance from the read-out sensor, a fact that can be overcome by lapping of the crystal's surface [38].

After assembling the detector it is necessary to check its energy resolution with a γ source and to measure the light yield and LONU. Due to the large number of manufactured crystals, the Swedish CALIFA group from Lund University developed a scanning table where up to 32 crystals can be inspected at the same time. As Figure 3.10 displays, it contains a scanning head that is capable of carrying two collimated sources and is driven in x- and y-direction by two stepping motors. The collimators allow for scanning two crystals at a time with a source that is collimated to $0.01\,\mathrm{sr}$ [39]. The entire volume is lightproof and thermo- as well as RF-insulated. Furthermore, a Peltier element enables the user to set the system to a defined temperature in order to, for example, investigate the temperature compensation of the preamplifier. The entire readout chain equals the final CALIFA readout including the FPGA firmware algorithm for pulse shape analysis.

The measuring procedure to determine the LONU follows agreements with the supplier that demand 10 measuring points along the crystal's main axis starting $10\,\mathrm{mm}$ from the exit window and approaching the entrance window in steps of $20\,\mathrm{mm}$. The source of choice is ^{137}Cs with a γ-ray energy of $662\,\mathrm{keV}$ and crystals showing LONU smaller than 3 % are passed. In addition, the energy resolution is measured with ^{22}Na at the center point of the crystal because the γ-ray energy of $1275\,\mathrm{keV}$ lies close to the benchmark of $1\,\mathrm{MeV}$ where an energy resolution better than 7 % leads to the acceptance of the crystal.

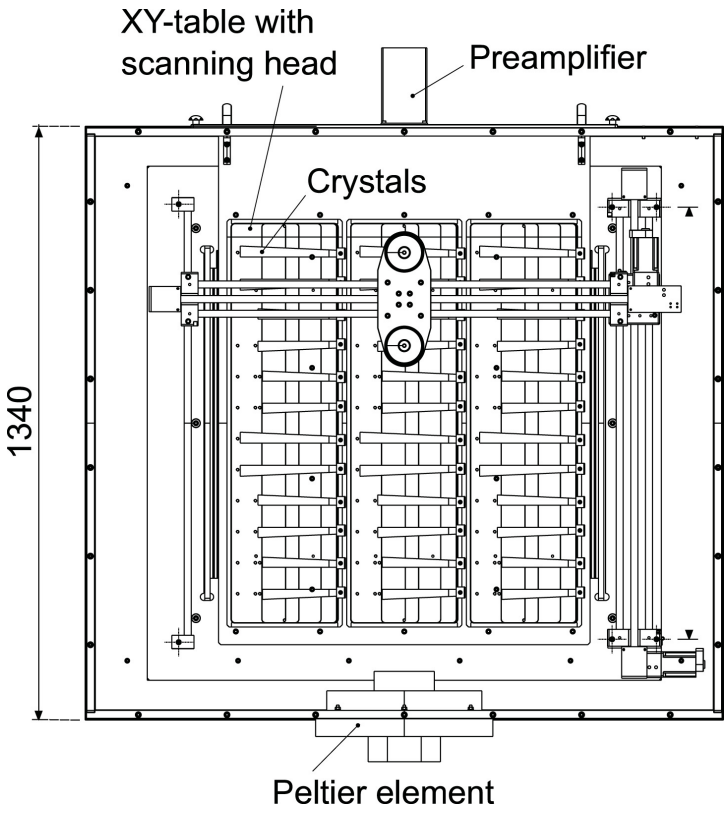

Figure 3.10.: Sketch of the Lund crystal scanner, courtesy of A.Knyazev [39].

As a result, the energy resolution in FWHM for $1275\,\mathrm{keV}$ γ-rays of a ^{22}Na source is plotted in Figure 3.12 over the LONU, measured with $661\,\mathrm{keV}$ from a ^{137}Cs source. Eye-catching is the energy resolution that lies well under 7 % for all crystals independent of their shape as indicated by different colors. However, a correlation between the energy resolution and the LONU is apparent. Generally speaking, crystals with higher non-linearity show worse performance in energy resolution. A reason for this is a lack in focusing of the photons onto the read-out device leading to propagation of photons within the crystal. On the other hand, absorption of photons on their way to the read-out surface also has an impact on the performance. These two processes counteract in the search for the optimal length of a crystal, as shown in Figure 3.11. Anyhow, for CsI(Tl) focusing is the dominant effect.

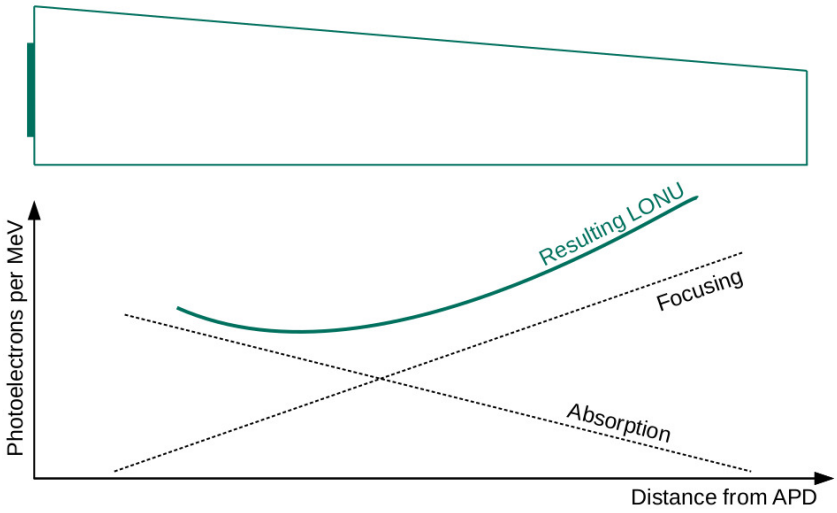

Figure 3.11.: Influence of focusing and absorption on the LONU depending on the distance from the photosensor, being based on [40].

Similar quality-assurance tests performed on the Barrel detectors showed the same behavior as displayed in Figure 3.13. The majority of both Barrel and Endcap crystals does not meet the desired 3 % limit for the LONU. Anyway, as the energy resolution is within the limits the crystals are accepted, but the supplier is encouraged to improve the lapping procedure.

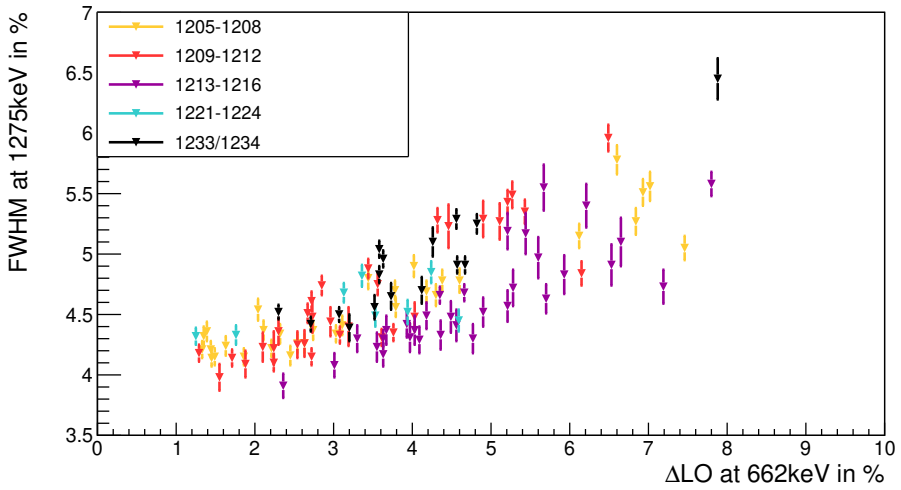

Figure 3.12.: Energy resolution of Iphos crystals depending on their LONU. A correlation between the two measures can be observed and that happens to be a decrease of energy resolution with increasing LONU.

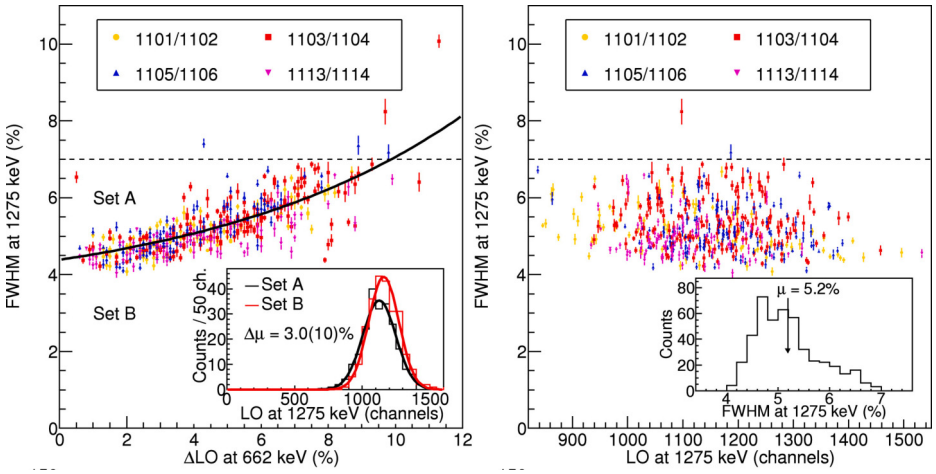

Figure 3.13.: (a) Energy resolution of 478 Lund Barrel crystals depending on their LONU, where a clear correlation can be observed, and (b) the energy resolution depending on the light yield of the detector, that shows no systematic impact on the performance, courtesy of A.Knyazev [39].

In a next step the energy resolution can be related to the light yield of the crystal as shown in Figure 3.14. The light yield is given in ADC channels and apparently the light output of bulkier crystals is lower than of the slimmer detectors. However, there is no clear correlation between energy resolution and light output as also was observed before, see Figure 3.13. Also energy resolution and efficiency do not seem to be strictly correlated, as displayed in Figure 3.15. For crystals of high efficiency, as a result of large volume, the energy resolution tends to be better than for less efficient slim detectors where the entire range of values for the energy resolution can be observed.

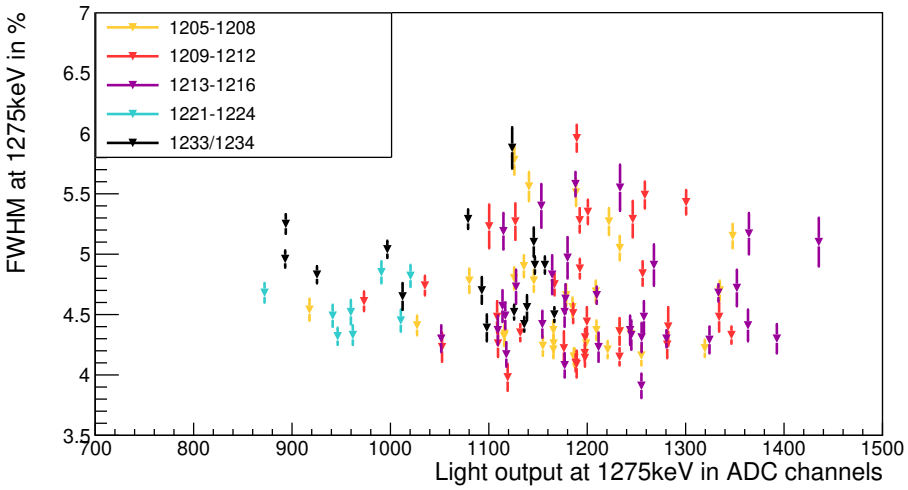

Figure 3.14.: Energy resolution of 120 Iphos crystals depending on their light yield, where no correlation can be observed.

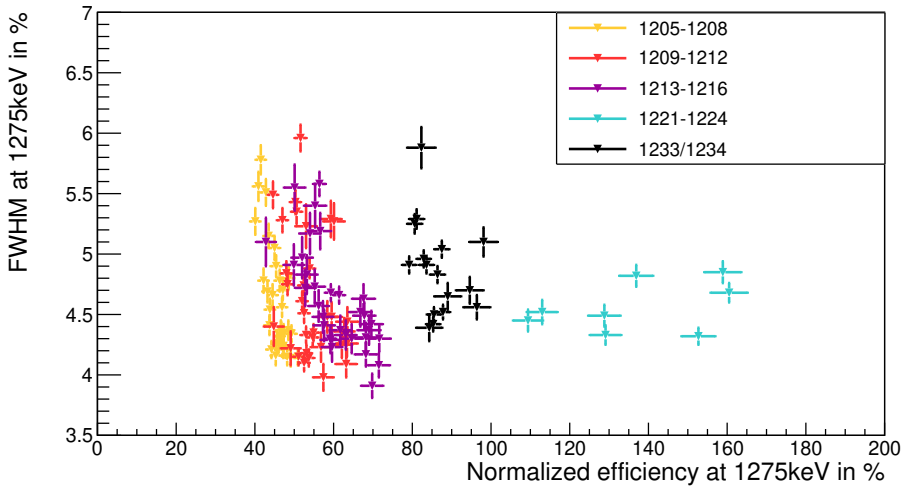

Figure 3.15.: The energy resolution depending on the efficiency of the detector. Here detectors of similar geometry show comparable efficiency, whereas their energy resolution may vary significantly.

3.1. Petal assembly

After assembling the 120 detection units and checking their performance, they can be installed in their designated mechanical structure. Following the mounting into two Iphos boxes, the crystals undergo a test with a γ source to check the addressability of the channels and to perform the gain matching procedure in order to adjust LAAPD bias-voltages.

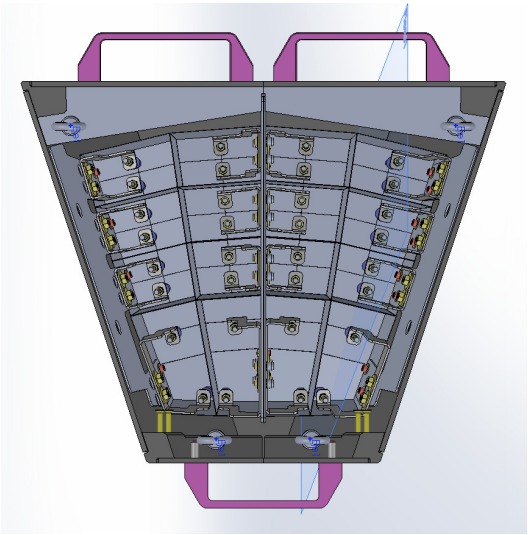

Figure 3.16.: Technical drawing of the top view of an Iphos box. The carbon-fiber pockets are marked and the fingers, preventing the crystals from falling out, are drawn in detail, courtesy of E.Casarejos.

3.1.1. Mounting of two Iphos segments

For test experiments and research purposes, special Iphos boxes were designed by our collaborators of the University of Vigo. These boxes were constructed to properly hold the delicate carbon-fiber structure, that encloses the crystals, and were equipped with handles and hooks to enable the user to move even the fully loaded box. The structure of an Iphos box is shown in Figure 3.16 and the distribution of the carbon-fiber pockets, also called alveoli, can be seen. The segment, that carries in total 60 crystals, is split into two mirrored halves containing 30 crystals each.

Unlike the Barrel section where only eight different crystal shapes are installed, the Iphos segments comprise eighteen different geometries. This variety is necessary to maximally cover the forward direction and to match the high demands of high count rate. As shown in Figure 3.17, there are three shape categories:

- **Bulky**: Innermost crystal
- **Flat**: Two crystals for each inner pocket
- **Slim**: Arranged in groups of four in the outer three rows of pockets

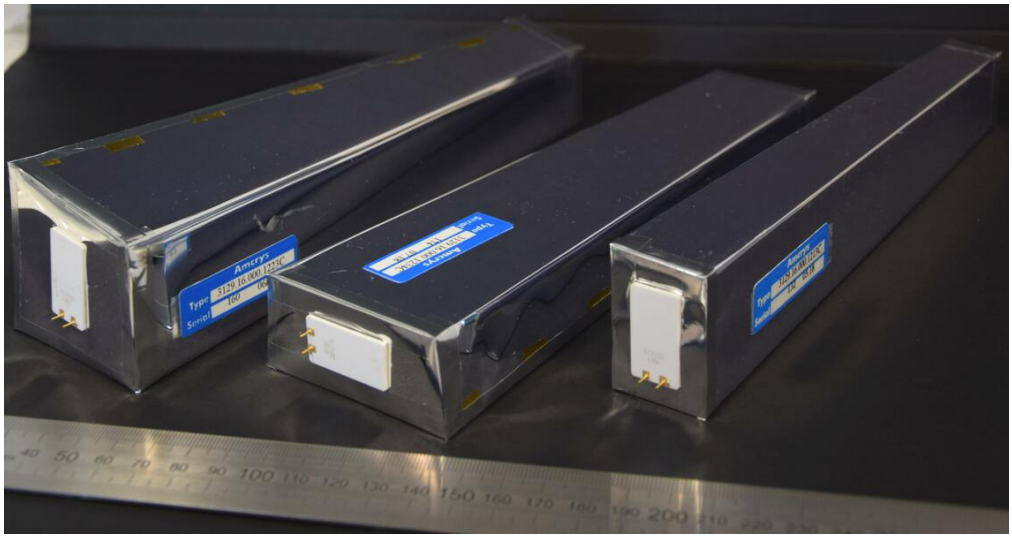

Figure 3.17.: Three Iphos detectors typifying the three major detector shapes used within the Iphos segments and illustrating the differences in crystal volume.

The mechanical part that holds the crystals in place during experiment is the carbon-fiber structure. The advantage of using carbon fiber as opposed to other materials is the very thin wall thickness that allows maximum spatial coverage by CsI(Tl) while, simultaneously, safely supporting the crystals. At this point of the assembling, the two segments are not set up into the final CALIFA structure, that is established at GSI, but into two Iphos boxes that are built for benchmark experiments or in-lab tests. The aluminum boxes support the carbon fibre structure that is sensitive to shock and needs to be protected from tilting. It also contains the fingers that prevent the inserted crystals from falling out of the pockets as can be seen in Figure 3.18a. One Iphos segment comprises 16 pockets, also called alveoli, each containing three or four crystals depending on position and crystal size.

Before inserting the crystals into the alveoli, they need to be equipped with a strap enabling the reversibility of the process. One option here is to use a broad sticky tape that can easily be removed from the reflective foil of the detector. Unfortunately there have been problems with the tape's stability when getting the crystals out of the pockets as the sticky tape tends to tear making it difficult to remove the detectors. To overcome this, an adhesive copper tape is chosen that shows a better resistance against tensile force. Advantageous is a large bonding surface between the copper tape and the detector in order to spread the load over a larger area and thus preventing fissures in the tape. On the LAAPD side of the detector one needs to form a strap with the copper tape that allows easy lifting of the crystal. The crystals can then be inserted into the pockets, as shown in Figure 3.18b.

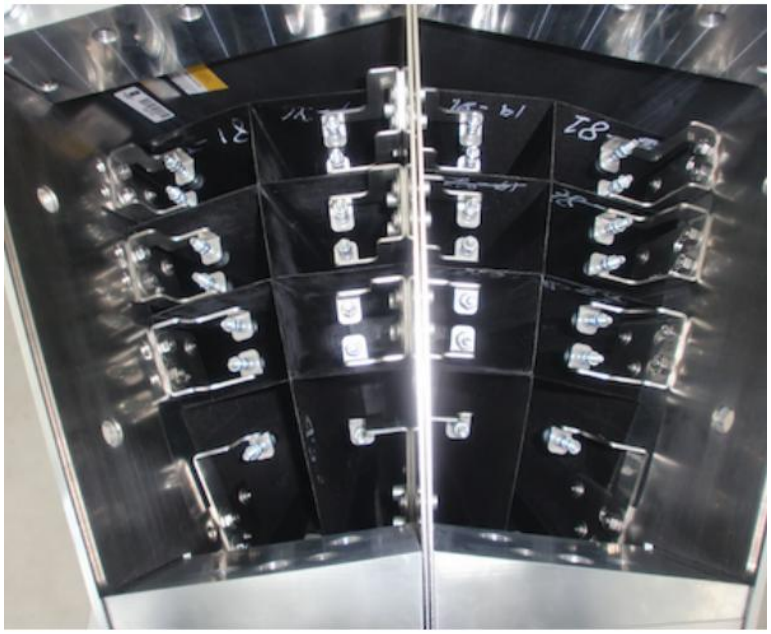

(a) Empty Iphos segment box.

(b) Partly filled segment.

Figure 3.18.: Within the empty segment box (a), a carbon fibre structure forms pockets where later the crystals are inserted in groups (b) and are set by metal fingers in order to prevent shifting or even falling out of detectors.

When all crystals are positioned in the correct pockets, their LAAPDs need to be connected to the preamplifiers. In this test setup for the Iphos segments, an unshielded pair of cables is soldered to a simple connector socket, that can be attached to the two contact pins of the photo sensor. The other end is soldered to a feed through connector, screwed to the lid of the aluminum box. From the outside of the box the preamplifier is plugged together with the connector in order to enable the closure of the box ensuring light tightness. A look into the box as in Figure 3.19 reveals the white ceramic plate of the LAAPD, where the blue cabling is attached, and the fingers, consisting of a set of a screw and several nuts, that hold the crystals in their desired position. Here another advantage of the adhesive copper tape surfaces, namely its formability that makes room for any action inside the cramped box.

Figure 3.19.: The inner cabling of the test Iphos segment is accomplished by unshielded cabling directly plugged to the LAAPD. Adhesive copper tape is used as flaps to ensure the removability of the crystals.

Figure 3.20 shows the inner working of the Barrel petal that was used in the experimental campaign at the Cyclotron Center Bronowice in Kraków, see Chapter 4. Unlike the Iphos segments, the cabling of the Barrel detectors were not connected directly onto the LAAPD during the experiment but a PCB was used. This saves the delicate pins of the LAAPD as the unshielded cabling is connected via a pin connector. Furthermore the board provides the temperature sensor, indispensable during experiments where gain corrections are important, and the connection for the optical fiber that will be used to introduce a well known light signal enabling checks on the actual gain. As straps on the detectors, Kapton® was used, which, at this point has been replaced by adhesive copper tape in more recent setups due to low stability, as discussed earlier.

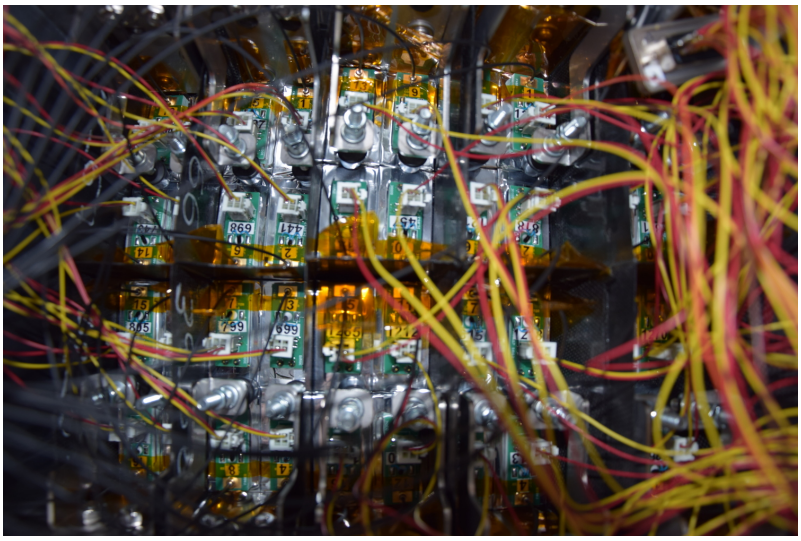

Figure 3.20.: Inner working of the Barrel petal used during the Kraków benchmark experiment. Even though the same cabling is used, its connection to the LAAPD is achieved via a PCB that offers a plug connection and the thermal sensor.

3.1.2. Gain Matching

After closing the two segment boxes and ensuring their light tightness, the four preamplifiers can be connected to the data acquisition. This DAQ is similar to the standard CALIFA system, but missing the add-on board and its shaping capabilities. Anyhow, this does not disturb the addressability check and the performance of a gain-matching procedure.

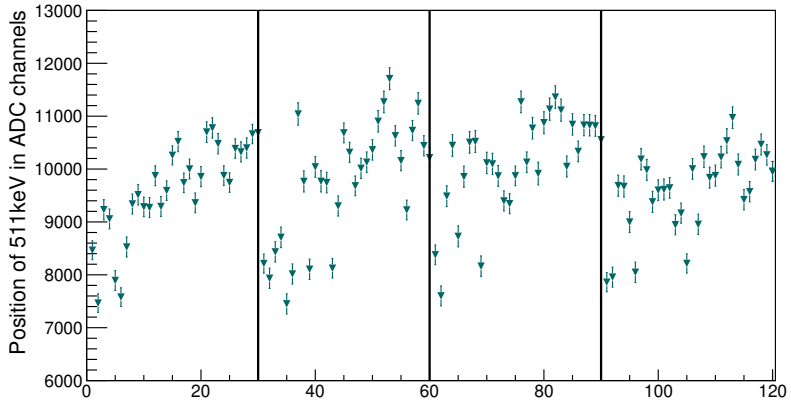

Figure 3.21.: Position of the $511\,\mathrm{keV}$ peak in ADC-channels for all 120 crystals with the respective uncertainty of the Gaussian fit.

A ^{22}Na source is placed next to the Iphos segments and a γ-ray spectrum for each detector is recorded at the nominal LAAPD bias-voltage. The position of the $511\,\mathrm{keV}$ peak in the ADC spectrum differs a bit for each detector due to differences in light collection and gain. All channels and their peak positions are plotted in Figure 3.21. Detectors belonging to one preamplifier are shown within one subdivision with the most voluminous crystal on the left getting to slimmer detectors on the right hand side of the subdivision. Generally speaking, an increase in ADC-channel number is observable when decreasing the crystal's volume. In principle, this is not a major issue but it complicates any fitting routine that can be employed in the further analysis. Therefore it is advisable to perform a gain-matching procedure on the 120 channels and to find a voltage setting where, in the best case, the peak position for each detector is at the same spot. The gain matching is done in three steps, namely:

- Scanning through an interval of bias voltages
- Finding a fitting voltage set for all detectors
- Reviewing the peak positions

Starting point is the recording of energy spectra with a ^{22}Na source, while varying the bias voltage around the nominal value given by the manufacturer. It is sufficient to scan a bias-voltage range from $-5\,\mathrm{V}$ to $+5\,\mathrm{V}$ in integer steps. Following this procedure, Gaussians are fit to all spectra and the position of the $511\,\mathrm{keV}$ peak in ADC channels is derived. A typical shift of the peak position with increasing bias voltage V_{bias} is shown in Figure 3.22a and can be described by an exponential function

$$\mathrm{Mean}_{ADC} = c_0 \cdot \exp[c_1 \cdot V_{bias}] \tag{3.2}$$

where c_0 and c_1 are fit parameters. This fit function describes the data close to the nominal bias-voltage but can not reproduce the observed peaks when going to higher values as the break-down voltage might be reached. Moreover, with increasing bias voltage also the noise level rises and this needs to be kept as low as possible. In a next step, see Figure 3.22b, the recorded peak positions of all detectors are plotted and the peak position where the voltage deviation for each detector is the smallest possible is defined. At this stage potential issues with detector channels are easily discoverable as they normally differ significantly from the average rise in gain.

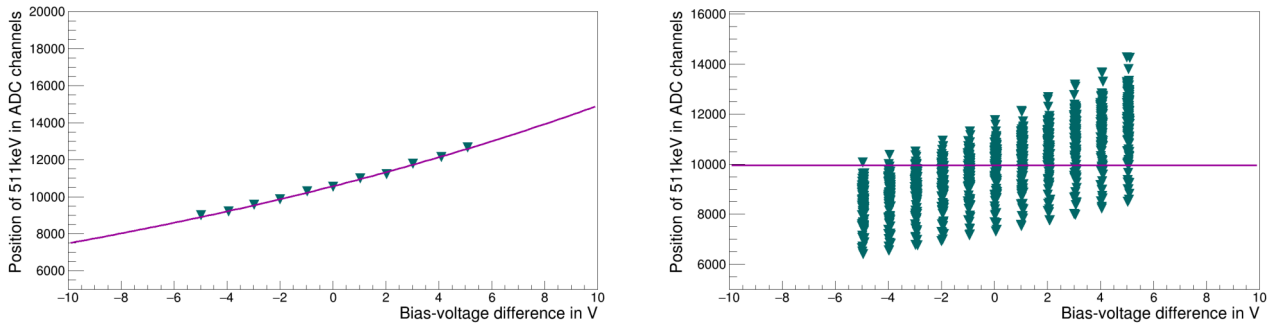

(a) (b)

Figure 3.22.: (a) Development of gain with increasing bias voltage for an exemplary Iphos detector and (b) an overview of all channels where the optimal peak position is marked in red.

It should be noted that the needed changes in the voltage setting may exceed the scanned interval, as is shown in Figure 3.23. This is not a major problem as long as the exponential fit describes the evolution of the peak position well. Another observable trend is that the bulkier detectors need considerably higher voltages resulting in higher LAAPD gain. The reason for this lies in the crystals' lower light yield that must be compensated by higher gain. In contrary to the bulky detectors, slim crystals need a reduced voltage resulting in lower gain in order to get a similar peak position for all channels.

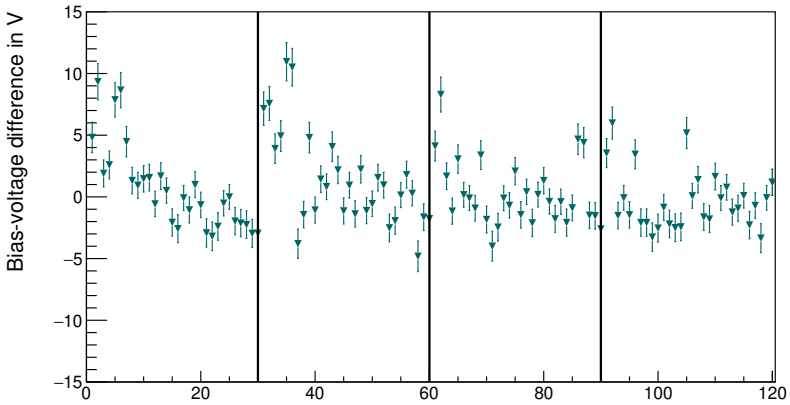

Figure 3.23.: Necessary bias-voltage changes for each detector after the gain matching procedure, also giving an estimation of the uncertainty resulting from the exponential and linear fit.

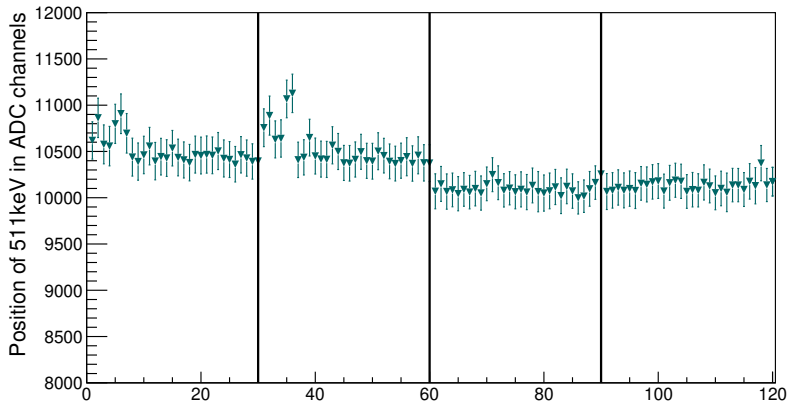

Figure 3.24.: Position of the $511\,\mathrm{keV}$ peak in ADC-channels for all Iphos crystals after the gain matching procedure with the respective uncertainty of the Gaussian fit.

The last step is the reviewing of the spectra that is done after applying the voltage changes and recording a ^{22}Na spectrum with all 120 detectors. The position of the $511\,\mathrm{keV}$ peak is similar for all channels, as can be seen in Figure 3.24, although it has to be mentioned that the result is better for segment two. A possible reason is the overall stability of its performance during the scanning and reviewing runs, where segment one had issues with the electronics. Anyhow, the result matches the requirements and makes further analysis steps easier.

3.1.3. Resolution

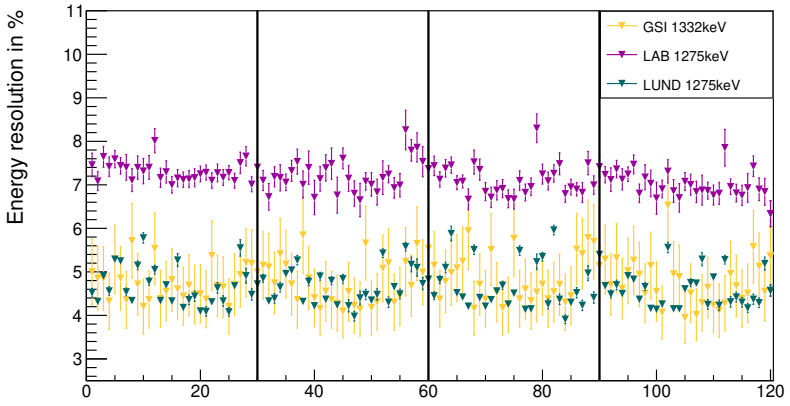

Figure 3.25.: Energy resolution of the Iphos crystals as measured at Lund, in the local lab and at a later experiment at GSI with the respective uncertainty of the Gaussian fits and for the CALIFA phase-0 setup the problems emerging from the unpacker.

With the obtained bias voltages, a source measurement was performed with ^{22}Na source emitting γ rays of $1275\,\mathrm{keV}$. Figure 3.25 shows the result of the measurement performed in the IKP lab utilizing the local DAQ in magenta. Apparently the energy resolutions range from $6.5\,\%$ to $8.5\,\%$ exceeding the scan result

from Lund (in green) by far. This deterioration in resolution of several percent can not be explained by the adaption in bias voltage, as the gain change in the range of the voltage adjustment is small. The third measurement of Figure 3.25 shows the result of a later calibration run of the same crystal set within the CALIFA phase-0 setup performed with γ rays of $1332\,\mathrm{keV}$ stemming from a ^{60}Co source. Besides issues with the unpacker resulting in the respective uncertainties, the performance of the crystals is in accordance with the first quality check conducted at Lund. The originally determined energy resolution could be confirmed. As the reason for the worsening of the resolution could not be reproduced in the scope of the detector calibration at GSI, the focus was put to the local DAQ system. A comparison of the FEBEX settings of the different measurements revealed a difference in the settings of the sampling size. As can be seen in Figure 3.26, the energy resolution of CsI(Tl) crystal equipped with a LAAPD improves with increasing total sampling size. Unfortunately, the quality check in the local lab was performed with an overall sample size of $68\,\mathrm{samples}$, where $1\,\mathrm{samples} = 20\,\mathrm{ns}$, that corresponds to the worst setting in Figure 3.26. The standard CALIFA DAQ utilizes a sampling size of $270\,\mathrm{samples}$ with a rising sample of $32\,\mathrm{samples}$ and therewith energy resolutions in accordance with the first scan results from Lund were achieved.

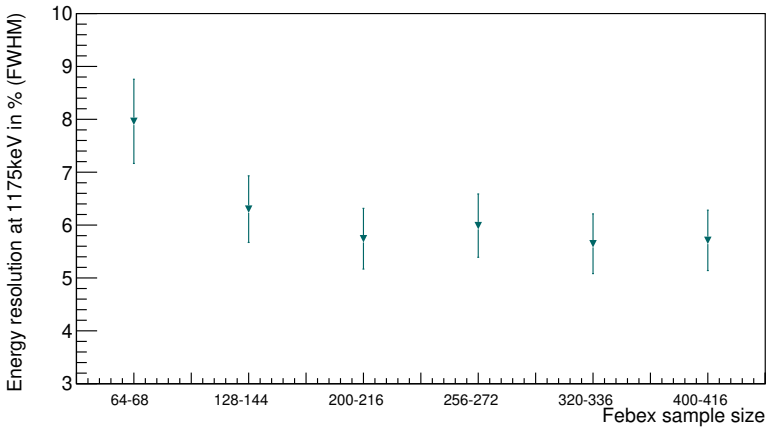

Figure 3.26.: Energy-resolution dependence on FEBEX sample size with uncertainties resulting from a Gaussian fit.

4. Test experiment in Kraków

4.1. Quasi-free scattering ^{208}Pb$(p, 2p)^{207}$Tl

Isotopes with closed nuclear shells offer ideal possibilities to test the shell model. Their states that are lying close to the Fermi surface exhibit single-particle behavior [10]. The single particle moves freely in an average potential created by all remaining nucleons. Hence, the assumption of a quasi-free scattering process holds true when bombarding such a target material with protons of $E_{Beam} = 200\,\mathrm{MeV}$.
It is important at this stage to chose the nucleus of interest with considering also the feasibility of producing a target that can be used in experiment. In general, the target material should be long living and best be malleable into a thin foil of well defined thickness in order to mount it on a target frame. Moreover, a high purity of the isotope is desirable.
At the current development phase of CALIFA, it is also important to chose an isotope that has already been well investigated in terms of cross sections and deexcitation energies of the residual nucleus. There are three $(p, 2p)$ settings that serve as benchmark experiments and were conducted during the campaign in November 2017, namely:

- ^{208}**Pb**: this work
- ^{16}**O**: analysis completed by B. Heiss, TU München [34]
- ^{112}**Sn** and ^{124}**Sn**: analysis to be performed by Lund university

The ^{16}O$(p, 2p)^{15}$N run was performed with a water-jet target and compared to experimental results measured at GSI in inverse kinematics [41] reproducing former results.

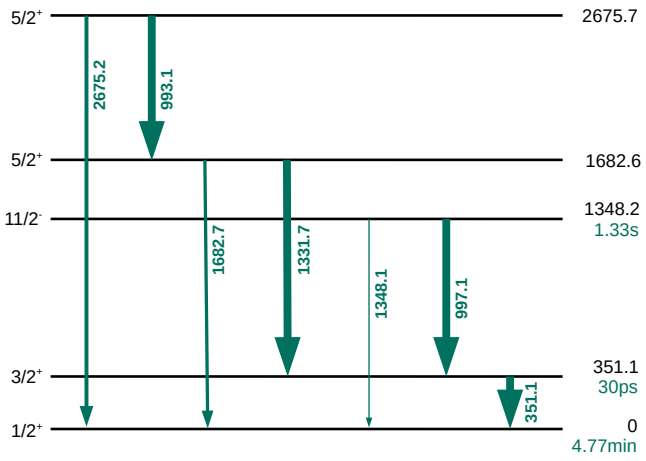

Figure 4.1.: Partial level scheme of ^{207}Tl with level energies limited to $2675.7\,\mathrm{keV}$, data as found in NNDC.

In the scope of this work, the quasi-free scattering on ^{208}Pb will be analysed and compared to results on cross sections of elastic scattering of protons on ^{208}Pb [42]. Moreover, aim of this benchmark experiment is to prove that it is possible to measure the two protons of the $^{208}\mathrm{Pb}(p,2p)^{207}\mathrm{Tl}$ reaction in coincidence with the γ ray of the deexcitation of the residual by employing three CALIFA petals. For this purpose, it is opportune that the excitation energies of ^{207}Tl are well known, as displayed in Figure 4.2, and the reaction has been investigated before by R. Neveling et al. [43] at iThemba Laboratory for Accelerator Based Sciences, Faure, South Africa. There, the reaction $^{208}\mathrm{Pb}(p,2p)^{207}\mathrm{Tl}$ was measured for three angle pairs utilizing a proton beam of $202\,\mathrm{MeV}$ resulting in the observation of levels up to the $3d_{5/2}$. The γ-ray energies were determined from binding-energy spectra and the resolution was high enough to separate the $3s_{1/2}/2d_{3/2}$ from the $2d_{5/2}/1h_{11/2}$ pair, but not the individual states due to the dependence on the precise measurement of the proton energy. In order to overcome this limit, the detection of the coincident γ ray enables the separation of single states and therefore a measurement of the reaction $^{208}\mathrm{Pb}(p,2p\gamma)^{207}\mathrm{Tl}$ with a better angular coverage and detection of the γ ray is very promising.

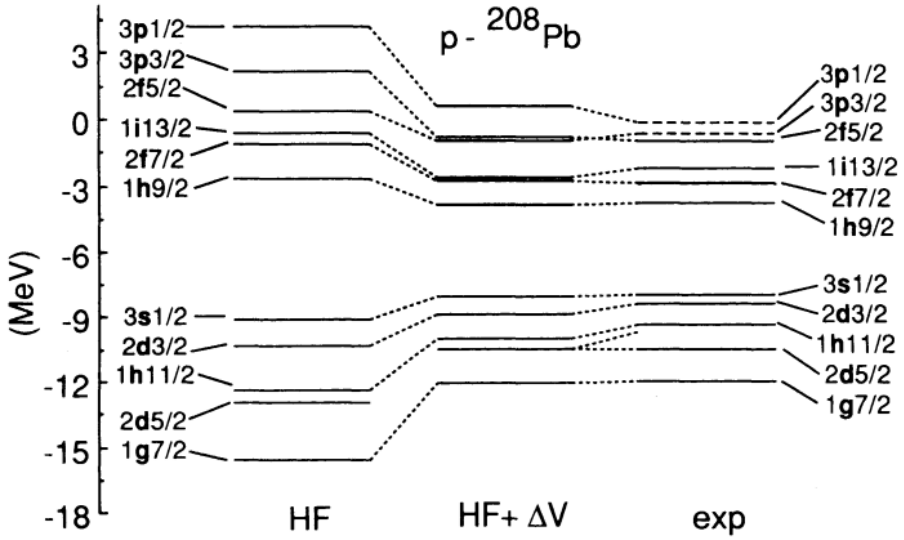

Figure 4.2.: Energy of the valence levels in ^{208}Pb calculated from Hartree-Fock potential (HF), full mean field (HF+ΔV) and experiment (exp), with permission [44].

Besides the feasibility, $^{208}\mathrm{Pb}(p,2p\gamma)^{207}\mathrm{Tl}$ is also an interesting physics case, as the knock-out of one proton leaves a hole in the closed shells of the doubly magic nucleus ^{208}Pb. The QFS reaction allows to probe the angular-momentum assignment of the levels close to the Fermi surface and their occupation probabilities. Unlike indicated by the liquid-drop model, the occupation probability above the Fermi surface is different from zero and and therefore excitation energies within the one-hole nucleus ^{207}Tl are of special interest.

4.2. Experimental setup

In the following, an overview on the used detectors and the experimental setup will be given. This information is complemented by a full scale $(p,2p)$ simulation based on Geant4.

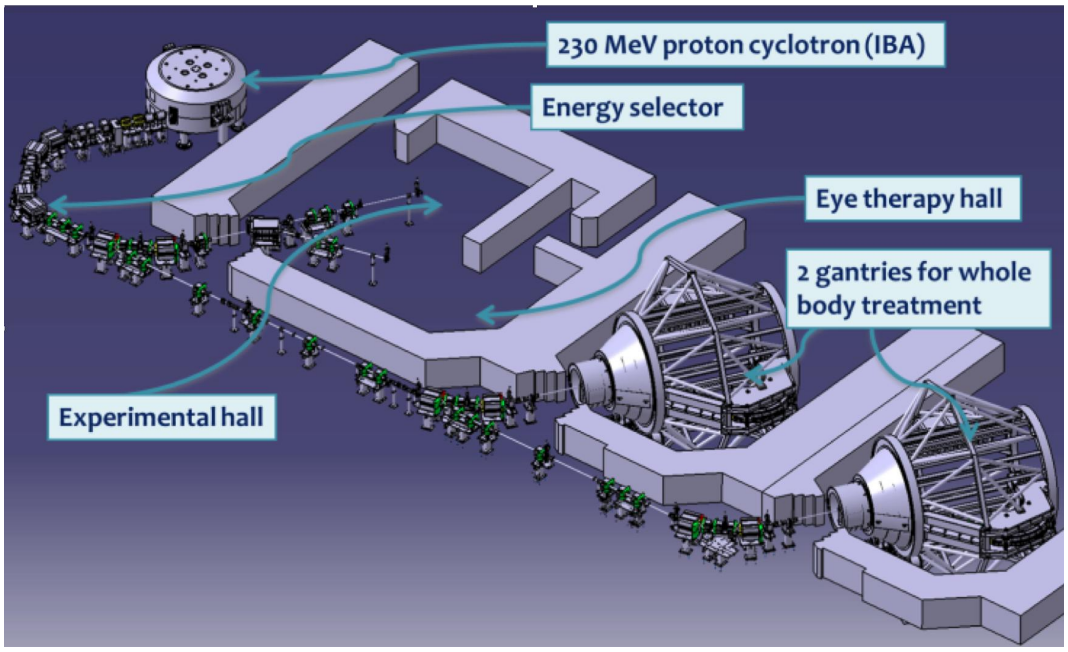

Figure 4.3.: Schematic illustration of the Bronowice Cyclotron Center with the experimental hall and the two gantries for cancer treatment, courtesy of A.Maj [45]

4.2.1. Beam facility and target

The experimental campaign was carried out at the Cyclotron Center Bronowice of the Henryk Niewodniczański Institute of Nuclear Physics belonging to the Polish Academy of Science in Kraków. The core of this facility is the proton cyclotron "Proteus C-235" that is used for nuclear physics, medical and material science research as well as for radiotherapy treatment of cancer patients. As the medical application is the major aim of the facility it provides protons within an energy range of $70\,\mathrm{MeV} < E_p < 230\,\mathrm{MeV}$ and the ability of quickly changing the energy setting by using a degrader wheel. By inserting degraders of defined thickness the beam energy of the primary cyclotron can be precisely downscaled. The degraders also cause energy-loss straggling that needs to be compensated. This is done with the help of magnetic filters that ensure a beam resolution of $\frac{\Delta}{E}E_{Beam} < 0.7\%$, a resolution crucial for medical treatment and also for nuclear physics experiments. Another disadvantage of the facility due to the primary purpose of medical application is the rather low available beam intensity in the range of $1\,\mathrm{nA} < I_{Beam} < 600\,\mathrm{nA}$. On the other hand the scattering of protons on a thin target requires the detection of a large number of secondary particles and the CALIFA detectors are limited to a count rate of $1\,\mathrm{kHz}$ due to the slow scintillating process of CsI(Tl). A higher event rate as result of higher beam intensity is not processible with the chosen detector system.
As a target, a ^{208}Pb foil with a purity of $98.69\,\%$ was rolled in order to produce a thin foil of $9.7\,\frac{\mathrm{mg}}{\mathrm{cm}^2}$ that was later held by a target frame, as shown in Figure 4.4. This target frame can later easily be mounted in front of the beam pipe and offers a quick change between targets. The same type of target frame was used to hold a radio-sensitive film that visualizes the beam-spot size when positioned at the target spot. The two slit settings lead to different spot sizes on the film and the beam-spot size for the ^{208}Pb run can be determined to be $(12 \pm 0.5)\,\mathrm{mm} \times (7 \pm 0.5)\,\mathrm{mm}$.

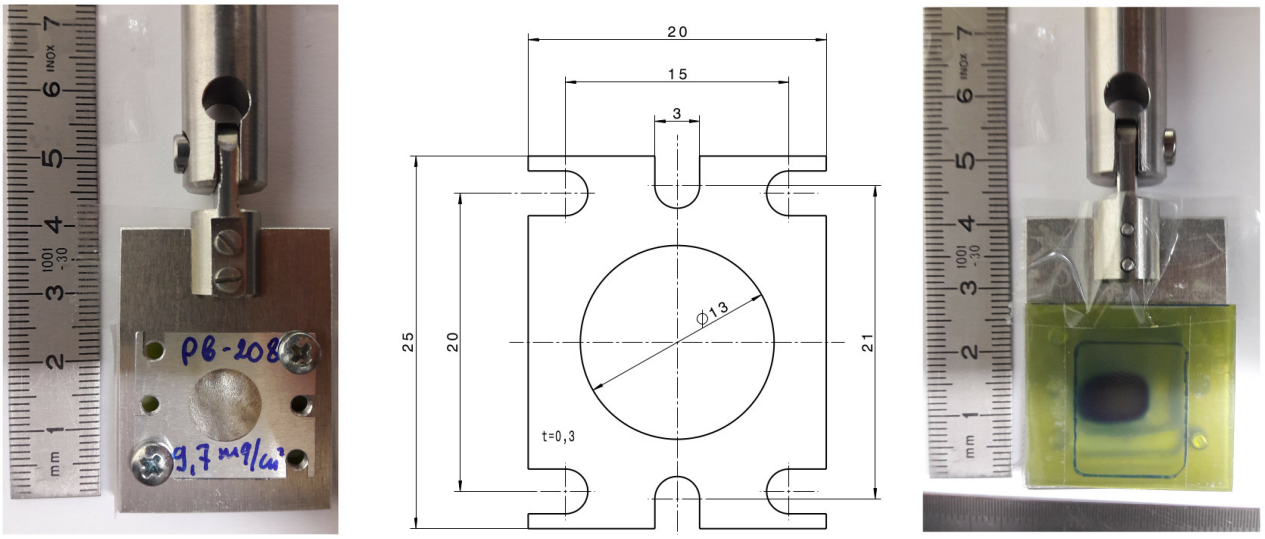

Figure 4.4.: A standard target frame (b) equipped with a ^{208}Pb foil of $9.7\,\frac{\mathrm{mg}}{\mathrm{cm}^2}$ thickness (a) and a radio-sensitive film for beam visualization (c).

4.2.2. Detectors

In order to reconstruct the excitation energy of the residual nucleus, it is necessary to detect both outgoing protons as well as the possible γ quantum stemming from the deexcitation of the target nucleus. Therefore, two petals of the CALIFA demonstrator with silicon strip detectors in front were employed to detect the two protons in one plane. A third CALIFA petal was arranged between them in an upright position with the purpose of detecting coincident γ rays, as can be seen schematically in Figure 4.5 and built up in Figure 4.6. The position of the two flat lying detectors is chosen by taking into account the experience on quasi-free scattering in direct kinematics that showed an average opening angle of $86°$, which was also derived by a full-scale Geant4 simulation discussed later in Chapter 4.3.

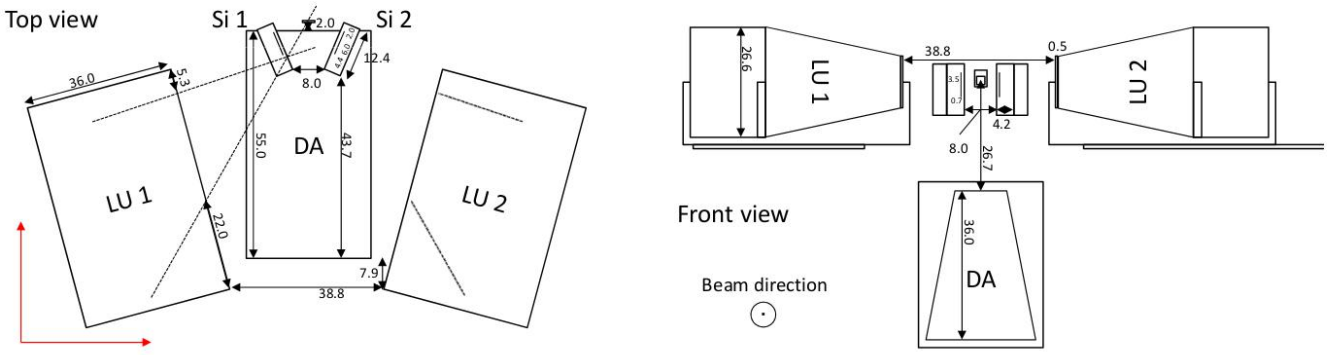

Figure 4.5.: Schematic illustration of the experimental setup with measures given in cm and with a precision of $\pm 0.1\,\mathrm{cm}$.

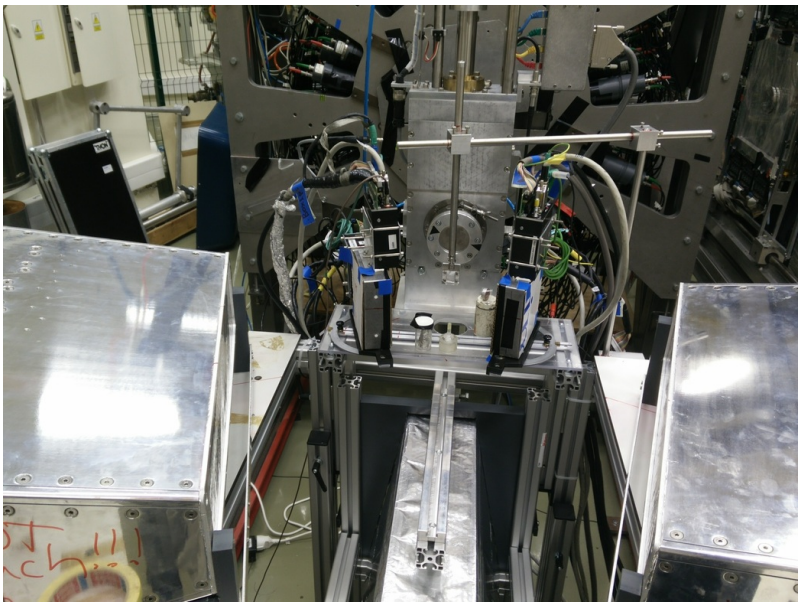

Figure 4.6.: The experimental setup with sources put at target position as seen from a downstream position.

Besides the three CALIFA petals, the setup contained two **D**ouble **S**ided **S**ilicon **S**trip **D**etectors that were supplied by Lund University. These DSSSDs are part of the **L**und-**Y**ork-**C**ologne **CA**lorimeter(LYCCA) and provide 32 strips in x- and y-direction covering an active area of $58.5\,\mathrm{mm} \times 58.5\,\mathrm{mm}$. Each detector has the size of $60.1\,\mathrm{mm} \times 60.1\,\mathrm{mm}$ resulting in a strip pitch of $1.8\,\mathrm{mm}$ on the front side and $1.63\,\mathrm{mm}$ on the ohmic rear-side. The thickness of the silicon wafer is $300 - 320\,\mu\mathrm{m}$. For a more detailed picture, one may consult the LYCCA TDR [46]. For the current experiment the DSSSDs were housed in aluminum boxes whose entrance and exit windows were covered by $20\,\mu\mathrm{m}$ mylar foil. As displayed in Figure 4.7 the preamplifiers for front and rear side were attached to the aluminum case and from there connected to the DAQ.

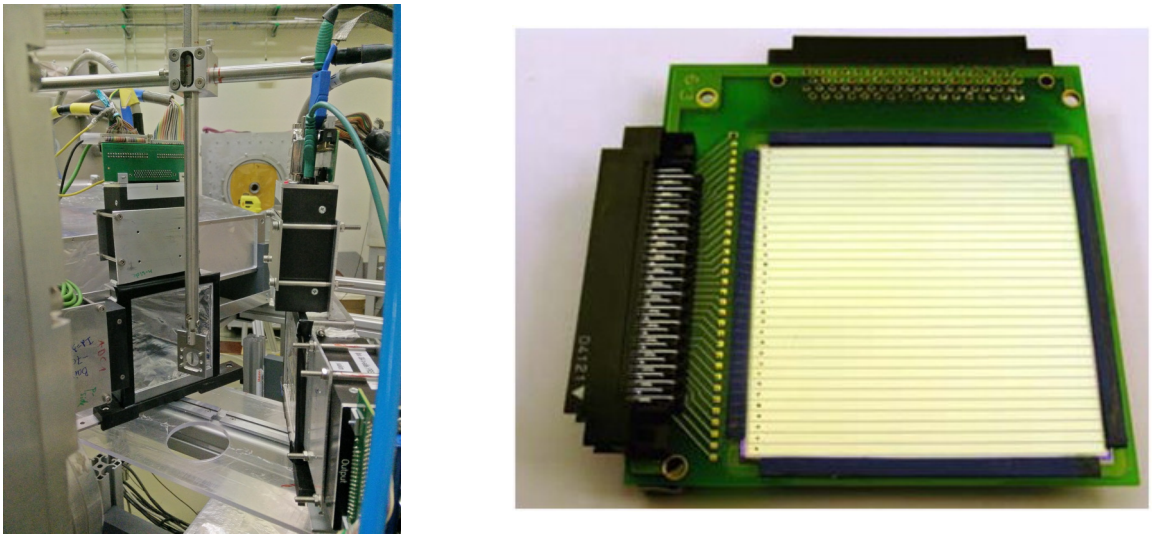

Figure 4.7.: The LYCCA DSSSDs with their two preamplifiers respectively as installed during experiment (a) and a more detailed view on the silicon waver (b).

4.2.3. Data aquisition

As a first stage of the readout, all detector signals undergo preamplification. For the petals, the standard CALIFA preamplifiers MPRB-32 are used that contain two individual 16 channel charge-sensitive preamplifiers. These modules feature high voltage supply for the LAAPDs, two switchable gain stages and compensation for the temperature dependence of the LAAPDs' gain. For the DSSSDs, charge sensitive preamplifiers manufactured by GSI were employed. These preamplifiers provide 32 channels with switchable gain and a decay time $\tau_{decay} = 15\,\mu$s.
The next stage of the DAQ, that processes the analogue preamplifier output, is the FEBEX 3B board. The FEBEX 3b cards were equipped with the FAB enabling particle identification based on the QPID method developed by TU München, for details see Chapter 2.3.5. For this setup, 20 FEBEX 3b cards with FABs were used, separated in two FEBEX crates. As each crate needs to be equipped with a separate fiber readout and trigger bus, the synchronous readout of two crates for the first time in experiment was challenging.
As the single event trigger, where every trigger causes the readout of all 320 detector channels, restricts the event rate of the setup tremendously, a suitable trigger condition needs to be defined. A fingerprint of $(p, 2p)$ reaction is an emitted proton pair where exactly one proton is detected in each detector arm. In order to reduce the overall event rate , but still to record all events of interest, the trigger condition is set to single proton trigger. Hence, a readout of all channels is triggered by an energy deposition of $10\,\mathrm{MeV}$ or more in LUND1 or LUND2 and records all coincident signals.

4.3. Geant4 simulation

For the planning and evaluation of the experiment, a full-scale Geant4 simulation was written by B. Heiss (TU München) and J. Park (Lund University) that includes the entire geometry of the setup and utilizes a QFS simulation code developed by V.Panin (GSI) and L.Chulkov (NRC Kurchatov Institute Moscow, Russia). Therefore, it is a perfect tool to reproduce the experiment and will be described in more detail in the following.

QFS event generator

Heart of the Geant4 simulation is the QFS event generator that is based on a FORTRAN code from L. Chulkov that was translated by V. Panin [47] to work within the R3BRoot environment in order to simulate QFS experiments in the R^3B setup. Alas, this event generator was written for indirect kinematics and needed to be translated to fit normal kinematics.

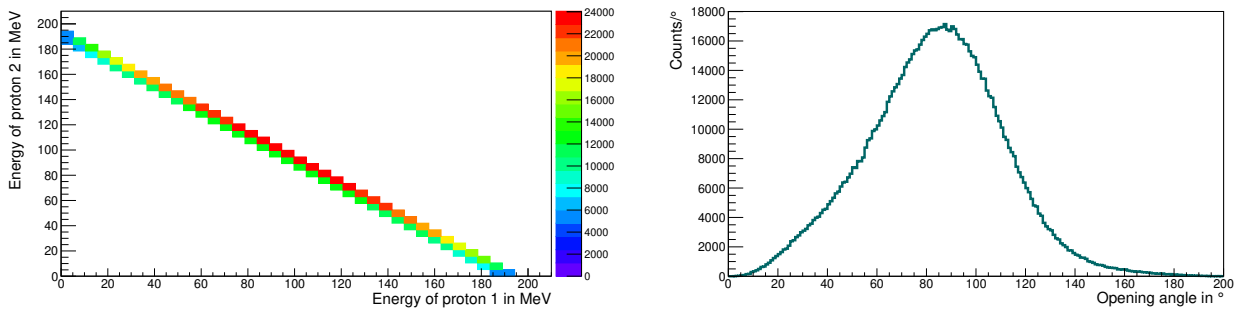

Figure 4.8.: (a) Energy correlation of the two emitted protons and (b) their opening angle as calculated by the QFS code.

The version of the event generator used for this experiment is a kinematical simulation that assumes a Gaussian distributed Fermi momentum and an isotropical emission of the outgoing particles. For the target nucleus ^{208}Pb the Fermi momentum can be calculated with Equation 1.3 and is determined to be $\sigma_{p_F} = 250\,\mathrm{MeV/c}$. The result of the event generator, not taking into account any geometry or detector influences, is displayed in Figure 4.8 for a proton beam of $E_{beam} = 200\,\mathrm{MeV}$. The energies of the outgoing protons are strongly correlated and their opening angle can be deduced to $\theta_{opang} = 86°$. The opening angle, anyhow, is widely spread due to the Fermi-momentum distribution of the knocked-out proton and its width at FWHM is $\sigma(\theta_{opang}) \approx 60°$.

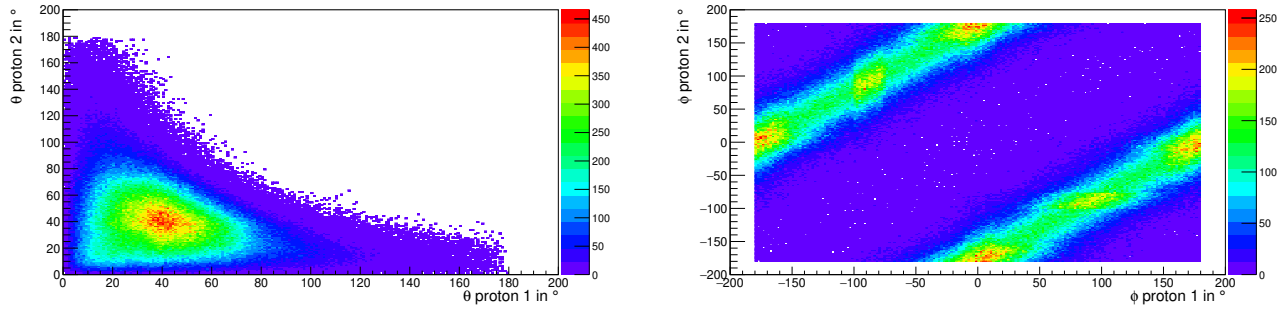

Figure 4.9.: (a) Polar and (b) azimuthal correlation of the two emitted protons as calculated by the QFS code.

Besides the expected energies and the openening angle, also the angular correlation is important for the positioning of the detectors. As already expressed by the opening angle, there is a correlation of the polar emission angle of the protons, as shown on the left of Figure 4.9. With the limited amount of available petals, the azimuthal correlation is even more significant for the feasibility of the experiment. As shown on the right of Figure 4.9, the proton pair is emitted into the same plane enabling their detection in a planar setup.

Simulation of ^{208}Pb$(p, 2p)^{207}$Tl in Geant4

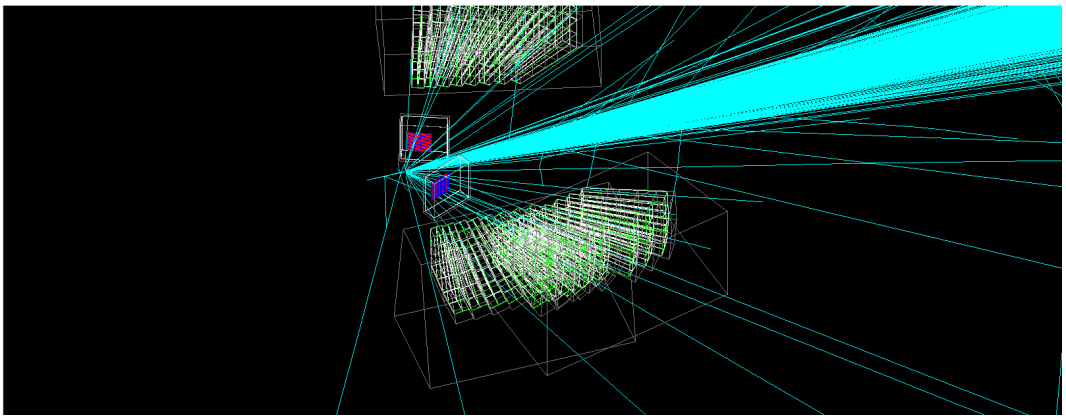

Figure 4.10.: Detector setup as implemented in Geant4 with two DSSSDs and three petals, beam coming from the left.

In order to perfectly copy the experiment into simulation, a full implementation of detectors and materials into Geant4 was done by B. Heiss and J. Park. Based on the measures in Figure 4.5 three petals and two DSSSDs were built and positioned, as shown in Figure 4.10. The above described event generator was used to produce the $(p, 2p)$ events of interest.

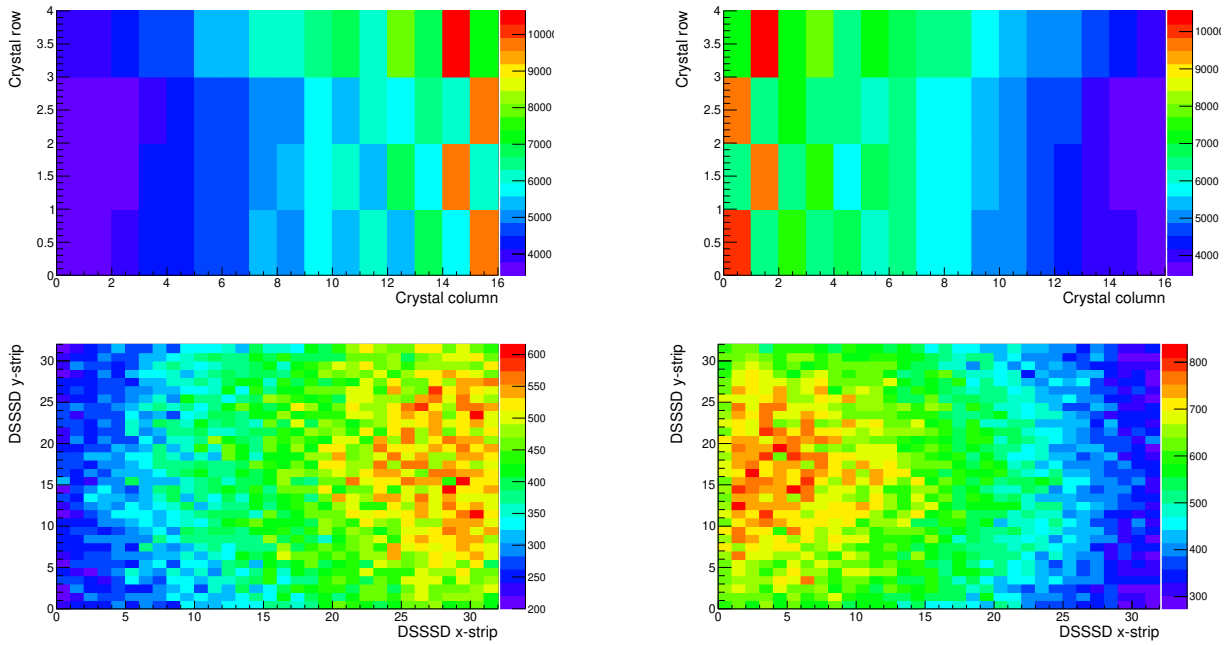

Figure 4.11.: Simulated hit patterns of the proton-tuned petals and the two DSSSDs with the target position lying in between.

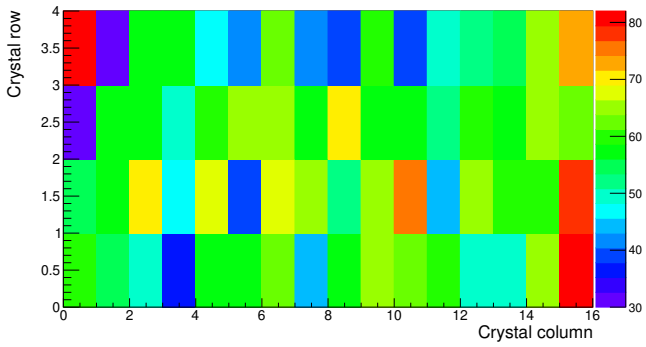

Figure 4.12.: Simulated hit pattern of TUDA1 that is caused by the emittance of γ rays up to $E_\gamma = 10\,\mathrm{MeV}$.

The resulting hit patterns of the four detectors of the experimental plane are displayed in Figure 4.11. It is obvious that the reaction causes emission strongly in forward direction as crystal groups and DSSSD strips referring to smaller scattering angles are hit significantly more often than those lying at larger angles. The hit pattern looks completely different for the third petal, as shown in Figure 4.12, positioned rectangular to the experimental plane and dedicated to measure only γ rays. The isotropical emission of particles as

given by the event generator, the detection of only γ rays as well as its different distance from the target spot are reason for this observation.

As already described for the event generator, the polar and azimuthal correlation of the two outgoing protons is significant for the $(p, 2p)$ scattering reaction. When comparing Figure 4.9 to correlations of the DSSSDs, as shown in Figure 4.13, the picture appears to be blurred. For the polar correlation or front-side correlation of the two DSSSDs the protons are emitted strongly to forward angles, but a sharp signature of the reaction can not be extracted. For the azimuthal or rather backside correlation, no defined correlation is visible. In contrast to former experiments exploiting the $(p, 2p)$ reaction on lighter nuclei, the Fermi momentum of the knocked-out nucleon plays a decisive role here as it smears out the angular correlation tremendously. When taking into account of the angular coverage of the DSSSDs in the experimental setup and reducing the angular range of Figure 4.9 to a polar angular range of $35° < \theta < 70°$ and a azimuthal angular range of $-14° < \phi < 14°$, a very similar picture arises. Hence, the blurred correlation is caused by low angular coverage, but especially by the Fermi momentum of $p_F = 250\,\mathrm{Mev/c}$.

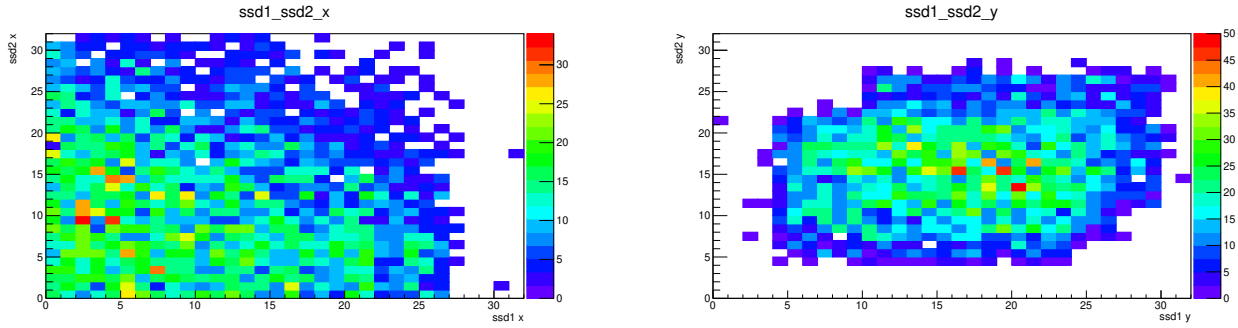

Figure 4.13.: (a) Polar and (b) azimuthal correlation of the two emitted protons as seen on the DSSSDs.

In the next step, the energy correlation between the two protons is plotted in Figure 4.14. In contrast to the output of the event generator in Figure 4.8 (a), the entire geometry of the setup is mirrored in this correlation plot. The resolution of the detectors was taken into account as well as the detector housing and the surrounding air. The effect of energy loss along the trajectory of the particle following the Bethe-Bloch-equation causes stronger energy loss for protons of lower energy and result in a bending of the correlation line. This effect is especially strong at the edges of the line, where the proton energy is lowest.

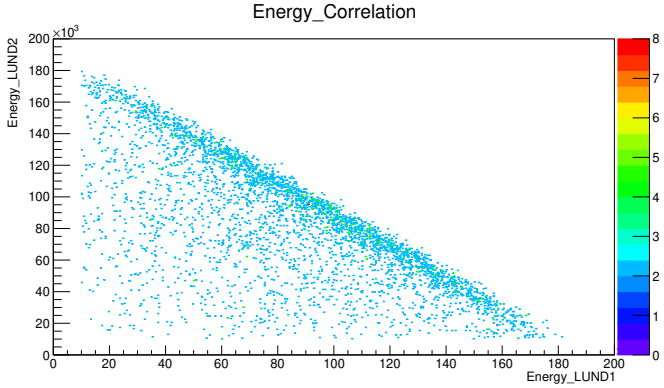

Figure 4.14.: Simulated energy correlation for ^{208}Pb$(p, 2p)^{207}$Tl for the ground state and exited state of $E_{level} = 1683\,\mathrm{keV}$ in the residual ^{207}Tl core.

5. Data analysis

5.1. Calibration of the CALIFA petals

In order to analyse γ rays and protons, each channel of the three CALIFA petals needs to be calibrated. Therefore a two-step calibration procedure is performed in order to achieve energy values on an absolute scale to calibrate both the gamma and the proton range.

5.1.1. γ-Calibration

The first step of the energy calibration of all scintillators is done by irradiating them with γ rays stemming from a ^{60}Co source. This isotope undergoes β^--decay into ^{60}Ni by emitting up to two γ quanta of $E_1 = 1173\,\mathrm{keV}$ and $E_2 = 1332\,\mathrm{keV}$ as displayed in Figure 5.1. The advantage of this calibration source is the energy difference of the two γ rays of approximately $160\,\mathrm{keV}$ whose separation in the spectra gives a first idea on the performance of the detector and both peaks are close to the expected γ ray of $E = 1331.7\,\mathrm{keV}$ stemming from the quasi-free scattering on ^{208}Pb [48].

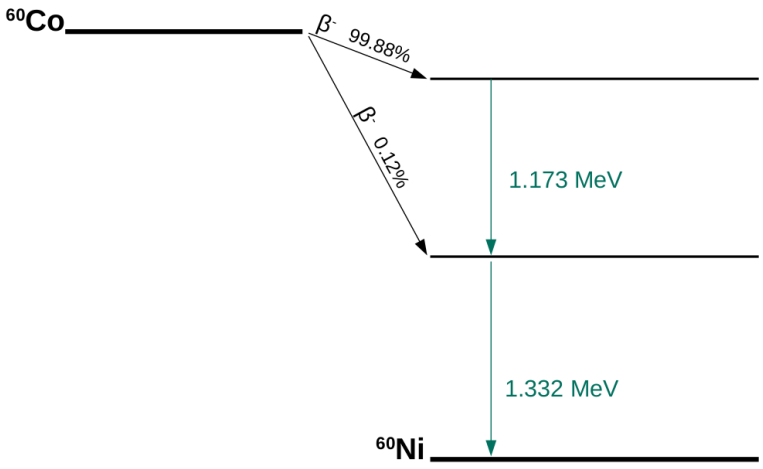

Figure 5.1.: Decay scheme of ^{60}Co with the two observable γ rays at energies of $E_1 = 1173\,\mathrm{keV}$ and $E_2 = 1332\,\mathrm{keV}$, that was used as calibration source for the three petals. Data as found in NNDC.

In order to get a first impression of the energy resolution of the CsI(Tl) detectors two single crystal spectra from the same run are shown in Figure 5.2. Their difference in count rate can be explained by their distance to the target point, where the source was placed. The different energy resolution is a result of the different operation modes of the detectors, the left spectrum belonging to a crystal operated in low gain mode and the right spectrum demonstrating the advantages of the high gain as used for the detection of γ rays.

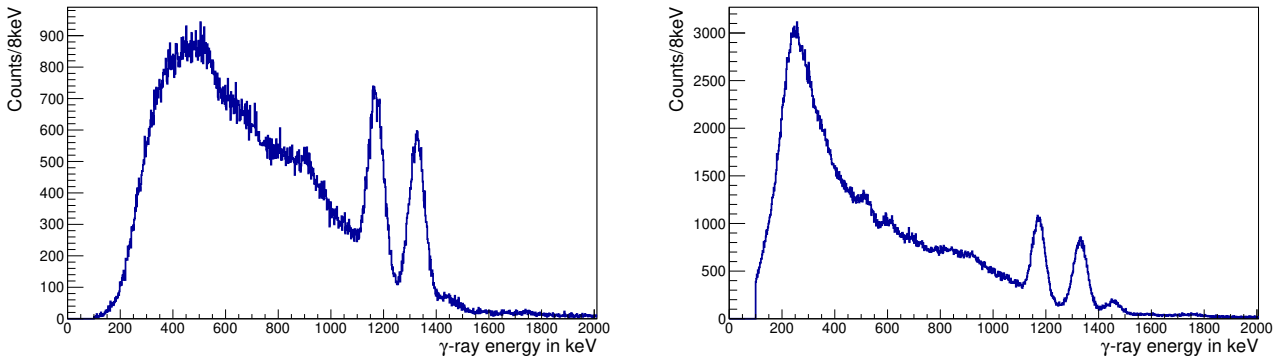

Figure 5.2.: Two exemplary detector channels showing the γ-energy spectrum measured by (a) one channel of the LUND1 petal tuned to proton detection and (b) of a TUDA1 channel running in high-gain mode.

For every detector channel the recorded spectrum needs to be fitted with two Gaussians and an exponential background in order to get the peak position of the two γ transitions. The obtained centroids M can be fitted by a polynomial of the first degree

$$E_{\mathrm{calib}} = a_{\mathrm{offset}} + a_{\mathrm{slope}} \cdot M_{\mathrm{ADC}} \tag{5.1}$$

from which the two fitting parameters a_{offset} and a_{slope} are derived. After applying the calibration parameters to the data set, the energy spectrum of each detector channel can be plotted and compared as done in Figure 5.3 for the two petals manufactured by Lund University, namely LUND1 and LUND2.

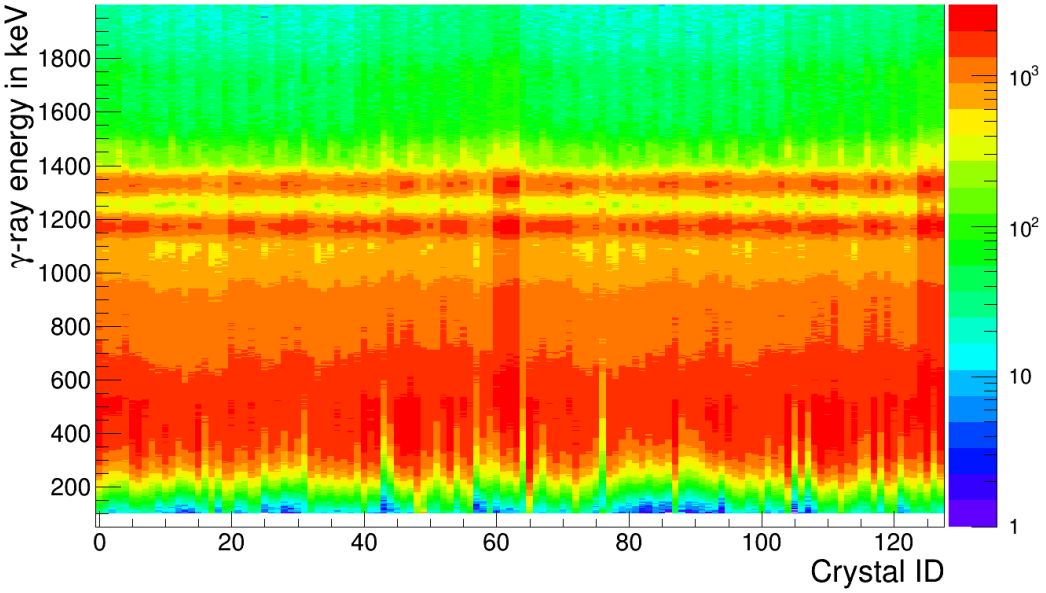

Figure 5.3.: Overview of all calibrated LUND channels. The two γ-ray energies appear as horizontal lines, that are clearly separated, and the individual thresholds show themselves in greenish at low energies. The difference in the threshold settings are based on adjustments due to the specific noise level in the single detectors.

These two petals were operated in low-gain mode and aimed for the detection of protons. Therefore their resolution when irradiated by a γ-ray source is lower compared to the third petal made by TU Darmstadt, whose energy spectra are shown in Figure 5.4. This detector array is operated in the high-gain mode resulting in an enhanced energy resolution when measuring γ rays, something that is obvious in Figure 5.4, but limiting the range to γ-ray energies. Also the setting of the thresholds in this petal was done smoothly so that a homogenous picture evolves.

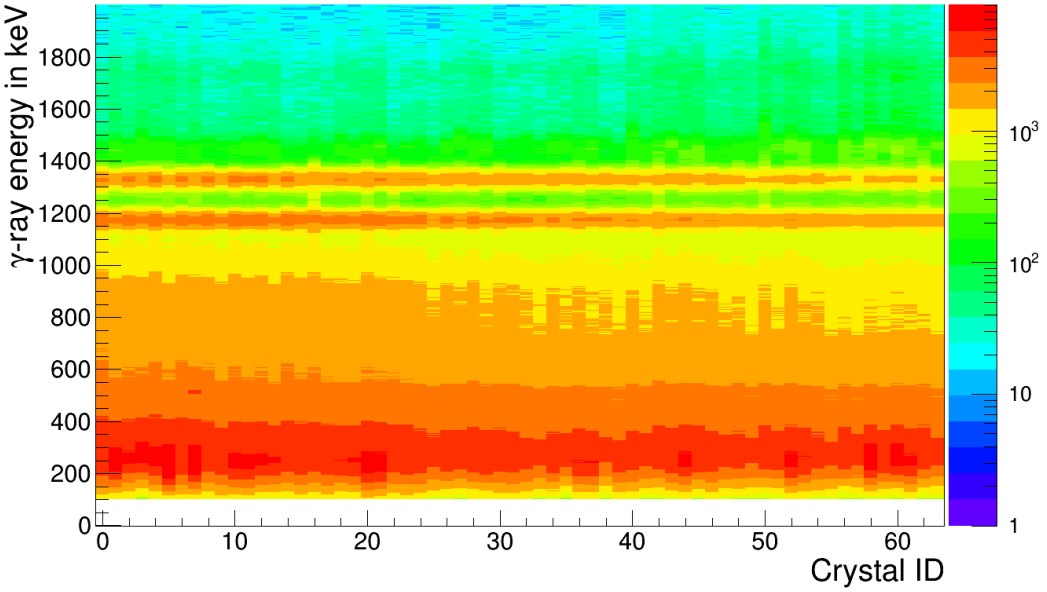

Figure 5.4.: Overview of all calibrated TUDA1 channels, that were operated in high gain mode, with the γ-ray energies appearing as sharp horizontal lines illustrating the high energy resolution for γ-ray detection. The lower count rates for higher channel numbers are a result of increasing distance to the source position.

In contrast, the petals tuned for proton detection show unequal thresholds because some of the channels had noise problems during the experiment and their thresholds needed to be adjusted. Moreover, the higher energy resolution for γ rays in high-gain mode is obvious when comparing the three petals. For TUDA1, the two γ-ray transitions form straight lines within the calibration overview, whereas the low-gain tuned petals LUND1/2 show smeared out lines. This is clearly no quality issue but a result of the available number of ADC channels.
An overview of the energy resolution of the three petals is shown in Figure 5.5, revealing four channels in LUND1, five channels in LUND1 and one channel in TUDA1 that performed badly in terms of energy resolution. Besides these channels, LUND1/2 show lower energy resolution due to the low-gain mode and TUDA1 matched the requirements of the CALIFA array of $5-6\,\%$ for $1\,\mathrm{MeV}$ γ rays [38]. The average energy resolution (FWHM) of the three petals for $1\,\mathrm{MeV}$ γ rays was determined to be

$$(\frac{\Delta E}{E})_{LUND1} = 6.70(4)\,\% \qquad (\frac{\Delta E}{E})_{LUND2} = 6.82(4)\,\% \qquad (\frac{\Delta E}{E})_{TUDA1} = 5.29(3)\,\% \tag{5.2}$$

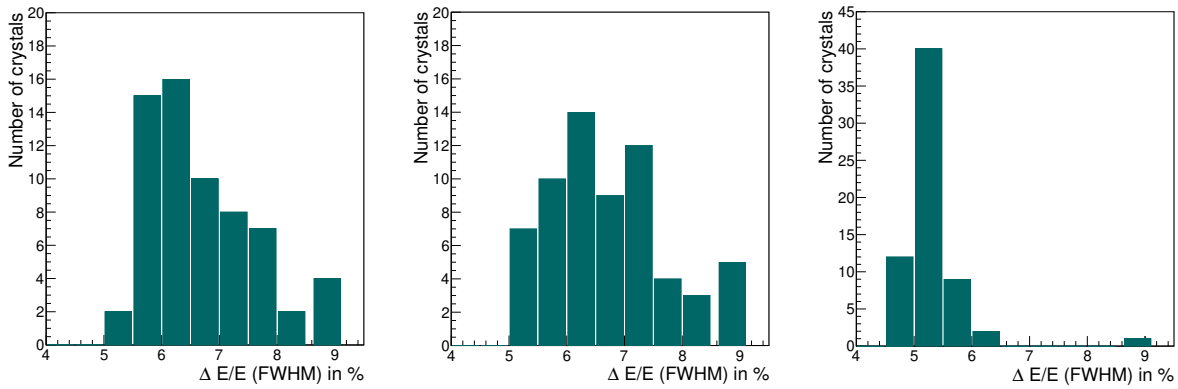

Figure 5.5.: Distribution of measured energy resolutions (FWHM) that were recorded with a ^{60}Co source and extrapolated to $1\,\mathrm{MeV}$ γ rays for LUND1 (a), LUND2 (b) and TUDA1 (c).

5.1.2. Proton calibration

After running the γ calibration with the source, a proton-beam run on a polypropylene target was performed. With a constant energy of $200\,\mathrm{MeV}$, protons impinged on a $0.6\,\mathrm{mm}$ thick target causing elastic scattering of beam protons on target protons. The scattered protons passed the DSSSD and deposited their energy in the corresponding CALIFA petal triggering the DAQ to record the event. Ideally, one proton is detected in each petal arm and the measured energies of both protons sum up to match the beam energy of $200\,\mathrm{MeV}$. When checking the resulting γ-calibrated spectrum, as shown in Figure 5.6, the picture differs considerably. The prominent peak, stemming from the elastic scattering, can be located at $214.5\,\mathrm{MeV}$ with a large tail towards lower energies. This clearly exceeds the beam energy and can be explained by the negative quenching of CsI(Tl) increasing the light yield that has to be taken into account when measuring protons and light charged particles. In addition, a second peak can be observed and associated with background reactions, e.g. the surrounding air as the entire set-up was operated in air and not in vacuum.

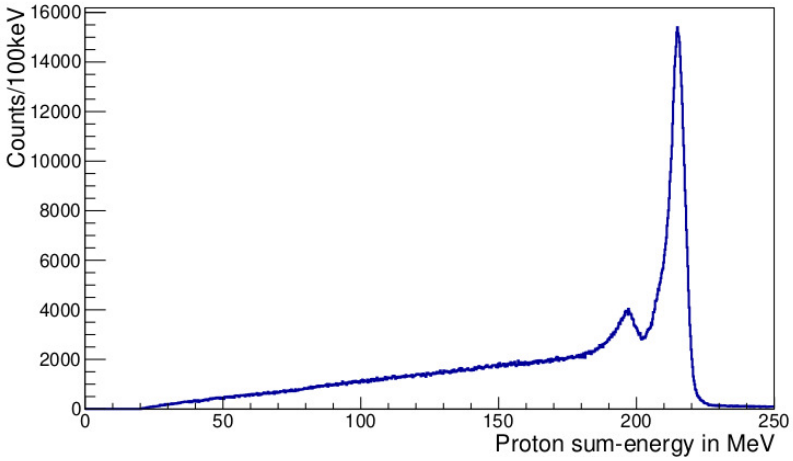

Figure 5.6.: Proton-energy spectrum after γ calibration with a peak at $214.5\,\mathrm{MeV}$ with a resolution of $\frac{\Delta E}{E} = 3.0(2)\%$ (FWHM) exceeding the beam energy of $200\,\mathrm{MeV}$. The smaller peak is a result of the interaction of protons with the surrounding air.

The negative quenching is a result of scintillation process within the CsI(Tl) crystal, that is in detail described in [49]. The light output for γ rays is diminished in contrast to protons by the ratio of 1:1.26 [50]. This is caused by recombination of excitons due to the lower ionization density of γ rays resulting in a lower light yield. As a consequence, the measured proton energies are systematically overestimated when solely applying the γ calibration.
Another indication for the need to have an additional proton calibration can be taken from Figure 5.7 where the detected energy in LUND2 is plotted versus the energy in LUND1. Both energies are given in MeV and were achieved by applying the γ calibration only. Clearly visible is the diagonal line that reflects the energy sum of the two elastically scattered protons that should match the beam energy of $200\,\mathrm{MeV}$. The clearness of the anti-correlation line confirms that the γ calibration is a suitable first approximation to transform ADC channels to energy. However, the line is not perfectly straight, but seems to be formed by several spots marking the energy sum of two corresponding crystal, one being in LUND1, the other in LUND2. This leads to the necessity of closely investigating the crystal correlation in pairs.

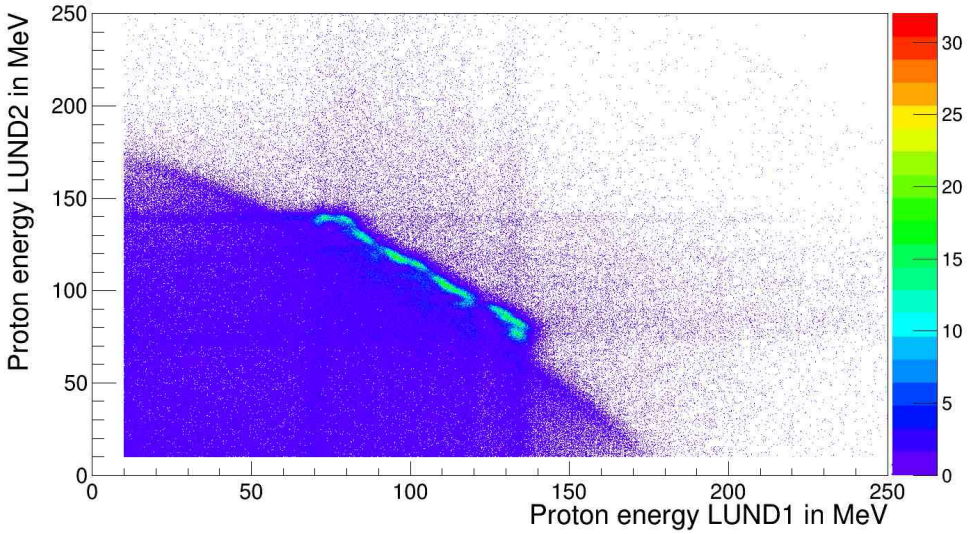

Figure 5.7.: Correlation plot between the two LUND petals before quenching correction showing an anti-correlation line that seems to be made of serveral peaks.

To better understand how crystals of LUND1 are linked to those of LUND2, hit entries of LUND2 are given in correlation with entries in LUND1 in Figure 5.8. An event causes an entry in this plot when a proton is detected in LUND1 and is correlated with a proton in LUND2, both of them exceeding the proton threshold of $E_{proton} = 10\,\mathrm{MeV}$. In this visualization of the correlation on crystal level, one can easily identify groups of crystals referring to a fixed ratio of measured proton energies. These energies are correlated to the scattering angle of each proton and hence are found in four detectors that are inside the petals stacked in groups of four. In Figure 5.8 they emerge in four correlation spots that are arranged in a step-like fashion. In order to derive a calibration factor that is able to compensate the negative quenching, it is now mandatory to plot the energy-sum spectrum of each correlated crystal pair. A Gaussian fit of the sum peak in relation to the beam energy then gives the correction factor for each pair that can be applied in addition to the γ-ray calibration. For crystals that do not have a matching partner the correction factor is calculated from the energy sum of all crystals.

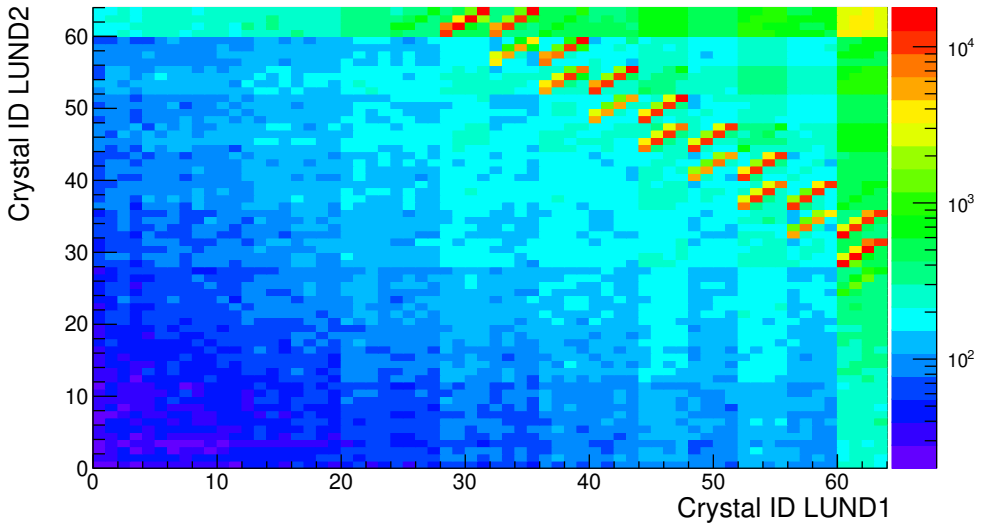

Figure 5.8.: Correlation of LUND1 and LUND2 on crystal level reflecting the inner structure of the petals as four detectors form a group within the petal box.

When applying the correction factors, the anti-correlation line straightens, as can be seen in Figure 5.9. In the edge region the line is still smeared out due to acceptance effects. An even more tremendous effect can be seen in the energy-sum spectrum, shown in Figure 5.10. The quenching-corrected energy sum of the two protons (green) moves to lower energies and matches the beam energy E_{Beam}. Furthermore, the energy resolution improves significantly and is $\frac{\Delta E}{E} = 2.1(2)\%$ (FWHM).

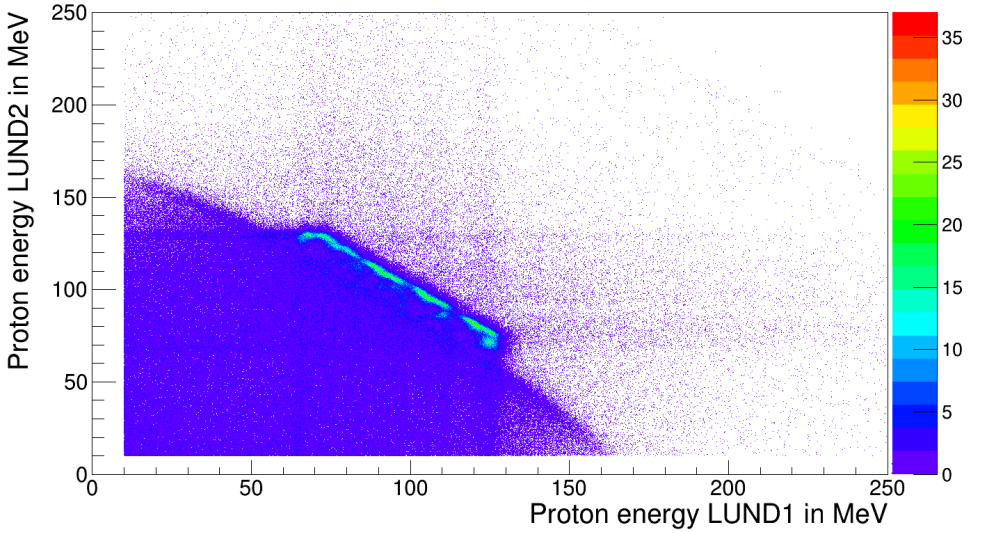

Figure 5.9.: Correlation plot after quenching correction resulting in a strightening of lines.

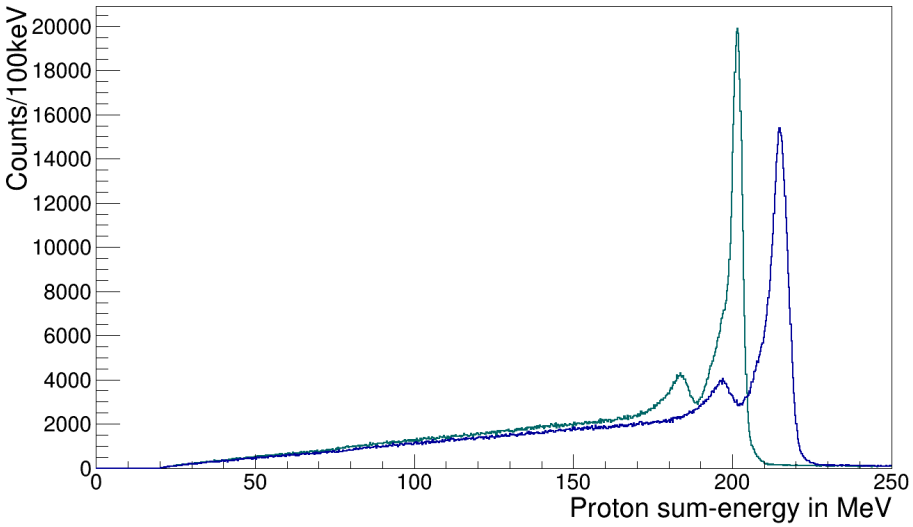

Figure 5.10.: The results of the quenching correction in the proton-energy spectrum, resulting in a shift of the peak towards the beam energy and an improvement of the energy resolution.

5.2. Addback

As the final CALIFA spectrometer is dedicated to measure high-energy particles, a precise Doppler correction is necessary. Therefore, the CsI(Tl) crystals of the calorimeter are relatively small improving the angular resolution. A drawback of this is an increase of Compton scattering and pair-production events when a crystal is hit by a high-energy γ-ray leading to a deposition of energy in several neighboring crystals. Hence, the energy of interest is split to two or more channels and a suited addback method needs to be defined. A glimpse at the internal structure of a CALIFA petal, as shown in Figure 5.11, leads to two simple approaches. The first option is to search for the highest energy entry, to locate its position and to add up energies of crystals sitting in the same alveolus whenever exceeding a required threshold. The other displayed possibility is the identification of the highest energy entry and adding the energies of all, maximum eight, neighboring crystals to this cluster.

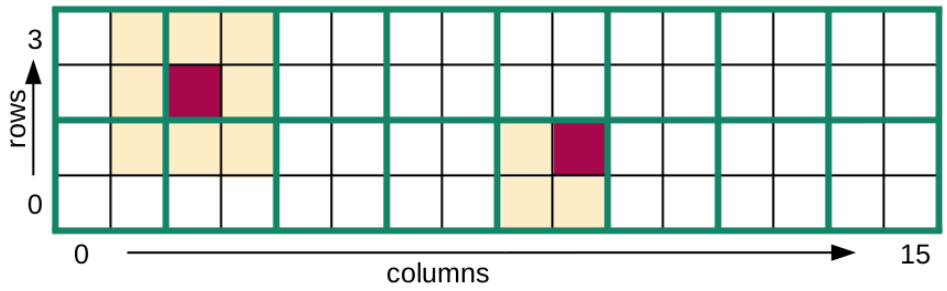

Figure 5.11.: Schematic representation of a CALIFA petal with a depiction of cluster (left) and pocket addback (right).

In order to decide on a suitable addback algorithm, both approaches were applied on the source measurement that was also used for calibration. As Figure 5.12 clearly shows, the two γ peaks stemming from the ^{60}Co source strongly gain entries when applying any addback algorithm. However, the cluster addback shows slightly better results in terms of peak height and reduction of entries in the region of $400\,\mathrm{keV}$ to $1000\,\mathrm{keV}$. In addition, it is more readily applied to the data structure of the experiment.

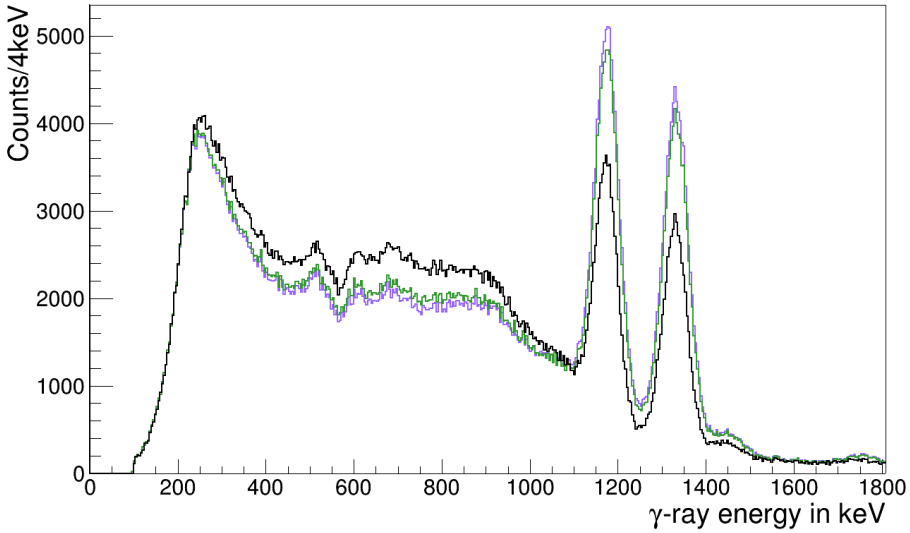

Figure 5.12.: γ spectrum **without addback** algorithm as reference to the same data set with applied **cluster addback** or **pocket addback**.

The addback procedure starts then with sorting all energy entries of a petal that exceed the γ-ray threshold. The highest energy entry defines the center of the first cluster and all energies of the neighboring crystals are added to the cluster energy. In case the cluster energy of LUND1 or LUND2 oversteps the proton threshold of $10\,\mathrm{MeV}$, the procedure is repeated but with taking into account the derived quenching correction. In order to not doubly count energies, these crystal are marked as used and are deleted from the list, and the number of crystals forming cluster is stored for later analysis. This operation is repeated for the next, not used, entry in the list until all clusters are defined.
With this routine, γ and proton clusters are build on an event-by-event basis following the same scheme.

5.3. Position calibration

Besides an accurate energy calibration, the absolute positions of the two petals and their corresponding DSSSDs need to be determined as well as the polar and azimuthal emission angle of the outgoing particles. The measures within the silicon waver are given with great precision by the manufacturer. So in order to calculate the absolute position of a DSSSD strip, it is necessary to determine the absolute position of the waver itself. The same holds true for the CALIFA petals that exhibit a fixed structure within the aluminum housing and can only be moved as entity.
The documented detector positions shown in Figure 5.13 assume a completely symmetric positioning of the detectors with well known distances with an estimated precision of the positions of about $\pm 0.1\,\mathrm{cm}$. Moreover, an optimal overlap of the angular coverage of DSSSD and petal is apparent.

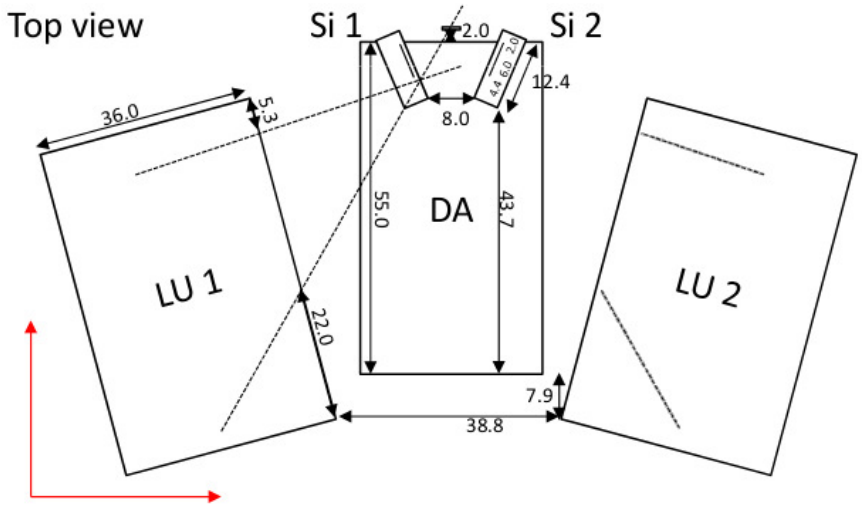

Figure 5.13.: Sketch of the Kraków setup with the measured distances in cm given with a precision of $\pm 0.1\,\mathrm{cm}$ and a tilting angle of the petals $\alpha_{petal} = 15°$ and of the DSSSDs $\alpha_{DSSSD} = 23°$.

Unfortunately, there are three major issues contradicting the above shown picture of the setup, namely:

- Calculated positions and angles do not match the picture.
- Hit patterns of the DSSSDs are not alike.
- Hit patterns of elastically scattered protons on the petals do not match.

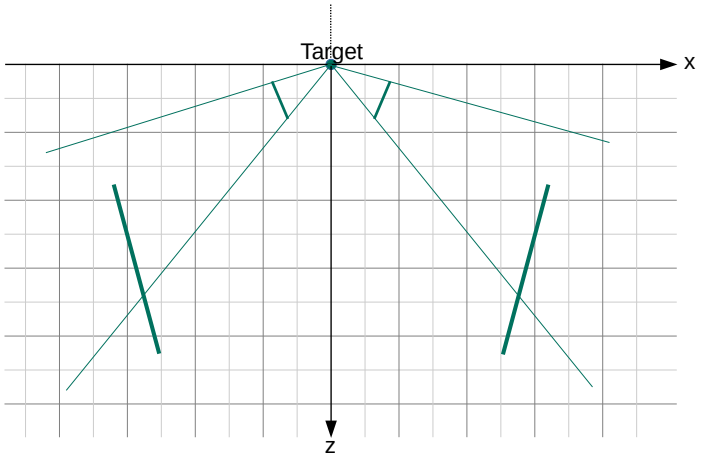

Figure 5.14.: Detector positions calculated by using the given distances in Figure 5.13 together with the known detector dimensions. The target is located in the origin of the plot and the detectors are arranged as in the setup's sketch (Black grid marking $10\,\mathrm{cm}$).

The positions of the detectors can be calculated with the help of the given distances in Figure 5.13 together with the tilting angle $\alpha_{DSSSD} = 23°$ of the DSSSD and $\alpha_{petal} = 15°$ of the petals and inner dimensions of both DSSSD and petal. The result of this calculation is given in Figure 5.14 and the misalignment of the DSSSDs is obvious. At the resulting location, the DSSSD would not sufficiently cover the petals.

Obviously, as shown in Figure 5.15, the hit patterns expected from the assumption based on the geometry in Figure 5.13 clearly contradict the observation. Due to the DAQ, described in more detail in Chapter 4.2.3, that is triggered by a particle hit in one of the petals operated in low-gain mode, the firing CsI(Tl) detector is projected onto the DSSSD's hit pattern. This results, as plotted in Figure 5.15 (a) for a plastic-target run, for DSSSD1 in a rectangular field in the center of the waver that has to deal with a significantly higher count rate than its surroundings. The rectangular region comprises 28 strips in x-direction and hence contradicts the findings of the strictly sketch-based calculation, where only a few DSSSD x-strips are hit together with a petal channel. Another observation can be made in Figure 5.15 (b), where the rectangle of coincident hits covers a lower y-strip range. In an absolutely symmetric setup, both x and y coverage would be the same. This proves that the initial assumption of a symmetric setup is not correct. Besides this, the positioning of the DSSSDs and the petals in height perpendicular to the x-z-plane was done properly, as also the horizontal gap caused by the inner structure of two layers of alveoli is visible also in the center of the DSSSD. For both DSSSDs it is strongest for y-strips 15 and 16, so the horizontal lines splitting the petals in two halves also divides the DSSSDs into equal halves.

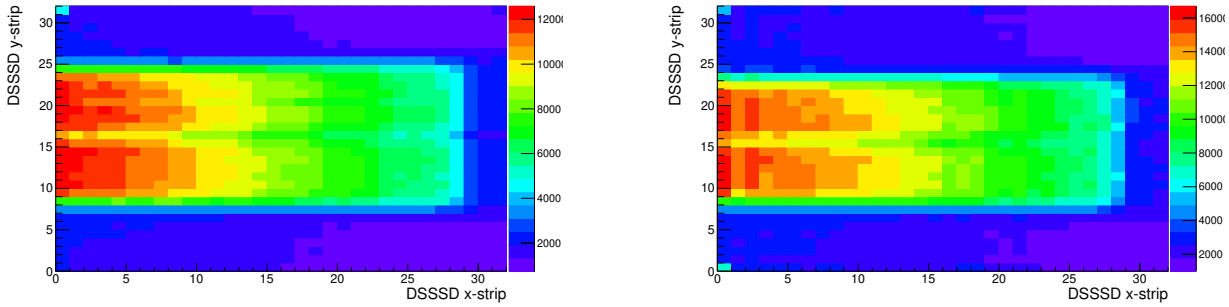

(a) Hit pattern of DSSSD1.

(b) Hit pattern of DSSSD2.

Figure 5.15.: Hit pattern of both DSSSDs with the projection of the corresponding petals caused by the proton-trigger condition of the DAQ.

To make clear, why also the petals' hit pattern do not match the original drawing of a symmetric setup, one has to have a look at the elastically scattered protons. Here, the following conditions need to be employed:

- Exactly two protons need to be registered, one in each petal.
- The sum of the two proton energies must match the beam energy E_{Beam}.

The procedure of distinguishing protons from other particles is described in detail in Chapter 2.3.5, and will be used at this point to make sure that the detected particle is a proton. Furthermore, the detector with the highest proton-energy deposition is marked as the point of first interaction. The energy of the proton is then determined by summing up the energy of the entire petal neglecting at this stage the different possibilities of add-back procedures. When employing the above mentioned conditions, one gets a hit pattern for each petal as shown in Figure 5.16.
For elastic scattering of protons on hydrogen, the opening angle between the two outgoing protons is

fixed. Therefore, the hit patterns of the petals should be alike in a symmetric setup where the DAQ is triggered by proton events in the petals. As Figure 5.16 (a) and Figure 5.16 (b) reveal, this is not the case as the maximum of hits is detected in LUND1 in detector group 10 and in LUND2 in detector group 12. Employing the sketch of Figure 5.13 as exclusive basis for a position calculation is not sufficient and more sophisticated steps are mandatory.

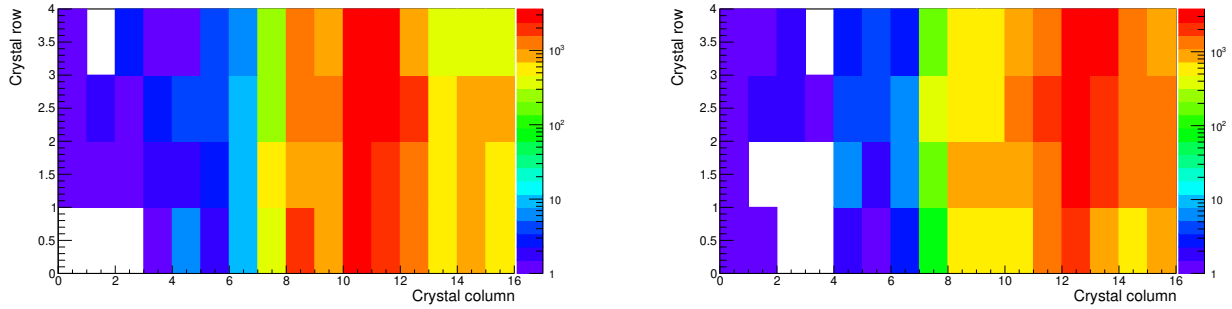

(a) Hit pattern of LUND1.

(b) Hit pattern of LUND2.

Figure 5.16.: Hit pattern of LUND1 and LUND2 for elastically scattered protons where both outgoing particles are detected by the corresponding petal.

First quantitative information in order to determine the absolute position of the four detectors, that are involved in the detection of protons, can be extracted from Figure 5.17. Here, the correlation between a crystal group within the petal and the corresponding x-strips of the DSSSD is apparent. In general, there are several possible x-strips that can be hit before the proton is finally detected in a CsI(Tl) crystal. What needs to be taken into account is that for LUND1 three detector columns were not covered by DSSSD1 (namely 13-15), see Figure 5.17a. On the other hand, DSSSD2 left only two columns in LUND2 without coverage (namely 14+15), as shown in Figure 5.17b, underlining the asymmetry of the setup. However, the correlation of each DSSSDs' x-strip with a CALIFA detector can be extracted.

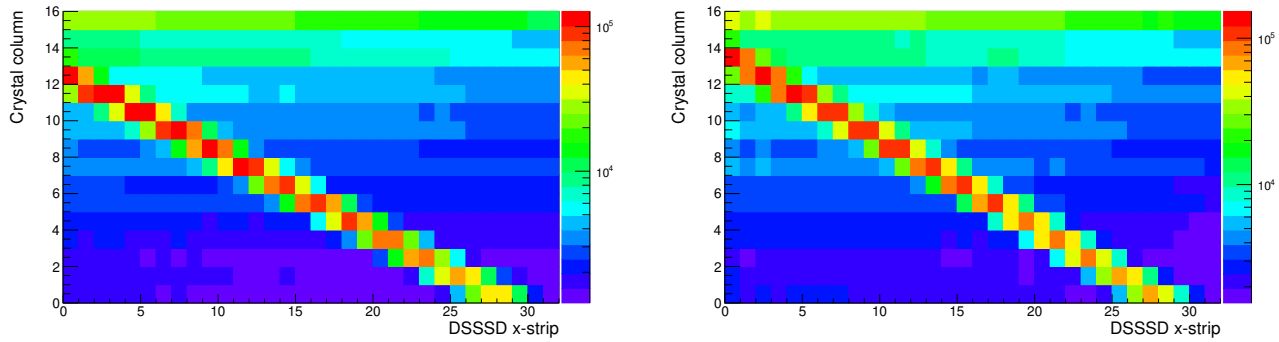

(a) Coincidence plot for DSSSD1 and LUND1.

(b) Coincidence plot for DSSSD2 and LUND2.

Figure 5.17.: Coincidence plots for both proton arms showing which DSSSD x-strips are hit together with a certain detector group in the corresponding petal.

Another piece of information one has to add to the picture is the dependence of the detected proton energy from the detection angle. For elastically scattered protons the scattering process can be expressed

by the Lorentz invariant Mandelstam variables s, t and u

$$\begin{aligned} s &= m_a^2 + m_b^2 + 2m_b E_a^T \\ t &= m_b^2 + m_2^2 - 2m_b E_2^T \\ u &= m_b^2 + m_1^2 - 2m_b E_1^T . \end{aligned} \tag{5.3}$$

Here m_a and m_b describe the masses before the scattering along with the incoming energy E_a^T in the laboratory frame and m_1, m_2 the masses and E_1^T, E_2^T the energy of the outgoing particles, as is also shown in Figure 5.18.

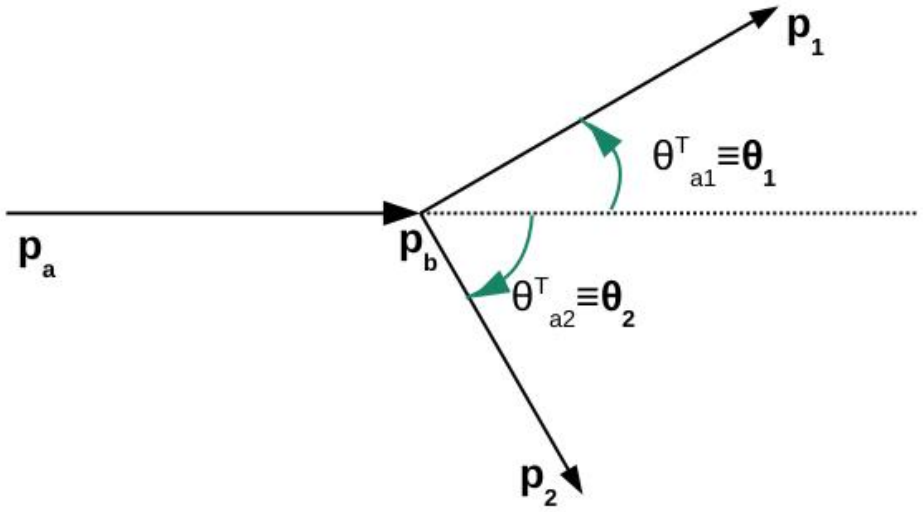

Figure 5.18.: Particle scattering kinematics for elastic scattering in the laboratory frame.

There is a linear correlation between the three Mandelstam variables, namely

$$s + t + u = m_a^2 + m_b^2 + m_1^2 + m_2^2. \tag{5.4}$$

As given in more detail in [51], the laboratory scattering angles θ_{a1}^T and θ_{a2}^T can be related to the Mandelstam variables by

$$\cos\theta_{a1}^T = \frac{(s - m_a^2 - m_b^2)(m_b^2 + m_1^2 - u) + (2m_b^2(t - m_a^2 - m_1^2)}{\lambda^{\frac{1}{2}}(s, m_a^2, m_b^2)\lambda^{\frac{1}{2}}(u, m_b^2, m_1^2)} \tag{5.5}$$

and

$$\cos\theta_{a2}^T = \frac{(s - m_a^2 - m_b^2)(m_b^2 + m_1^2 - t) + (2m_b^2(u - m_a^2 - m_1^2)}{\lambda^{\frac{1}{2}}(s, m_a^2, m_b^2\lambda^{\frac{1}{2}}(t, m_b^2, m_2^2)} \tag{5.6}$$

with the kinematical function $\lambda(x, y, z)$ defined as

$$\lambda(x, y, z) = (x - y - z)^2 - 4yz. \tag{5.7}$$

For the elastic scattering of protons on a plastic target the initial and final masses are the same, simplifying Equation 5.4 to

$$s + u + t = m^2 + m^2 + m^2 + m^2 = 4m^2. \tag{5.8}$$

Moreover, Equations 5.5 and 5.6 can be transformed for elastic proton scattering into

$$\cos\theta_1(t) = \frac{m[m(4mT_{Beam}+t)+m(t+2T_{Beam}^2)+tT_{Beam}]}{\sqrt{m^2T_{Beam}(2m+T_{Beam})(2mT_{Beam}+t)(4m^2+2mT_{Beam}+t)}} \tag{5.9}$$

and

$$\cos\theta_2(u) = \frac{m[m(4mT_{Beam}+u)+m(u+2T_{Beam}^2)+uT_{Beam}]}{\sqrt{m^2T_{Beam}(2m+T_{Beam})(2mT_{Beam}+u)(4m^2+2mT_{Beam}+u)}} \tag{5.10}$$

employing the energy relation $E_a^T = T_{\mathrm{Beam}} + m$. For a more detailed description of the calculation, see [51] or [52].
The result of the entire calculation performed above is a strict dependency of the detected energy from detection angle, as plotted in Figure 5.19. The proton energy is higher under more forward angles and diminishes when going to larger scattering angles. With the help of Equation 5.9 and Equation 5.10 the scattering angles can be determined from the measured energy of the detected protons. More precisely, the angle between the beam axis and the line from target to the CALIFA detector channel can be calculated from the measured energy in the CALIFA channel. Hence, a scattering angle can be assigned to each CsI(Tl) detector that is hit by an elastically scattered proton.

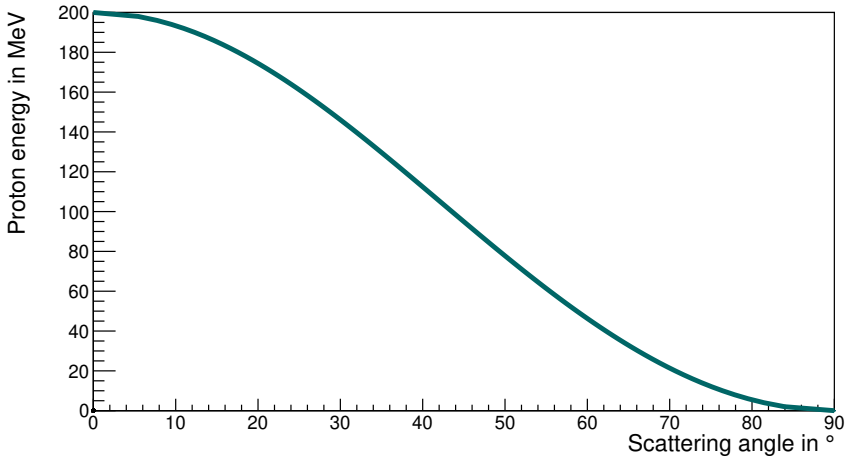

Figure 5.19.: The proton energy for p,p scattering at $200\,\mathrm{MeV}$ depending on the scattering angle, calculated with the help of the Mandelstam variables.

The applicability of this method is limited by the acceptance of the two CALIFA petals. Only a limited number of detector groups in each petal fulfills the condition of the scattering angle between the two protons being $\theta_{\mathrm{sim}} = 86.4°$, as simulated specifically for this experiment [34]. The limitation is already apparent in Figure 5.16a and Figure 5.16b, where the more outer detector groups are not marked as hit due to the fact that the corresponding second proton misses the other petal on the inner side.
For each detector in the CALIFA petals the corresponding strips on the DSSSD can be identified when hit in coincidence with a crystal. It is hence possible to assign the calculated scattering angle also to the x-strip of the DSSSD by taking the centroid of the correlated strip.
With the correlation between petal and DSSSD and the knowledge of the obtained scattering angle it is now possible to calculate the absolute positions of the four detectors. Here, a shift of each detector in x and z direction was permitted in order to leave enough margin to match all positions to the angles and also in

the end to reproduce the findings described in the beginning of Section 5.3. Table 5.1 gives the offsets of the detector positions in the proton arms.

Detector	x_{off} in cm	z_{off} in cm
DSSSD1	1.7	1.1
LUND1	2.2	-5.0
DSSSD2	0.7	0.7
LUND2	0.7	-6.5

Table 5.1.: Results of the correction of the detector positions where positive values indicate greater distance to the target and negative values a closer position in respect to the target, whose position was kept unchanged at (0|0|0).

The reconstructed positions of all detectors are plotted in Figure 5.20 revealing an asymmetric setup, as deduced before, with LUND2 slightly closer to the target than LUND1, reproducing Figure 5.16. Also DSSSD2 was found closer to the target which explains the differences in the DSSSD hit patterns in Figure 5.15. The smaller coverage of LUND2 on DSSSD2 is a result of the closer position of LUND2 to the target point. Overall, the correction of the detector positions gives a coherent picture and the further analysis will use this geometry.

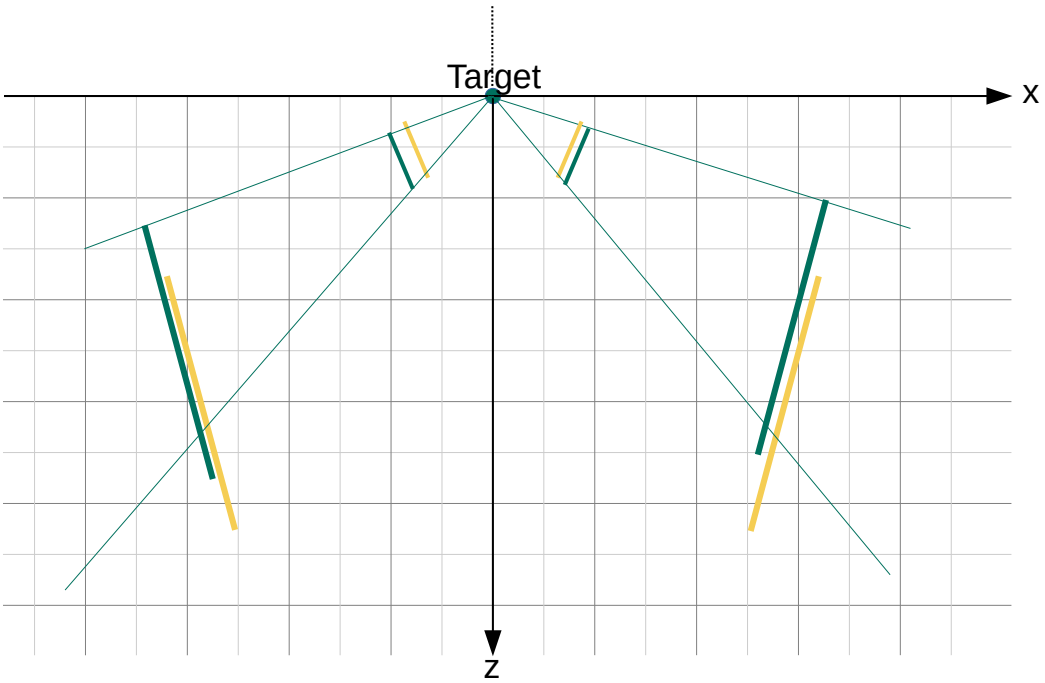

Figure 5.20.: Positions of the detectors **after correcting** the measured positions (green) by considering the detected proton energies in elastic scattering and consequently the scattering angles (Black grid marking $10\,\text{cm}$).

5.4. Event selection

After the calibration of the energy and angles of the detectors, it is now possible to filter out the events of interest, namely stemming from the $(p, 2p)$ reaction on ^{208}Pb. Here, utilizing the well defined kinematics of the reaction it is necessary to discard all registered events that do not include the comprehensive and complete information on the scattering process. The kinematics of the $(p, 2p)$ reaction exhibit the following observables in the outgoing channels:

- There are exactly two outgoing protons.
- The energy of the detected protons together with the binding and recoil energy sums up to the beam energy.
- Both correlated protons are detected in one plane.
- There is a defined opening angle between the outgoing particles.

In order to identify events that exhibit these characteristics several analysis steps need to be undertaken and will be explained in the following.

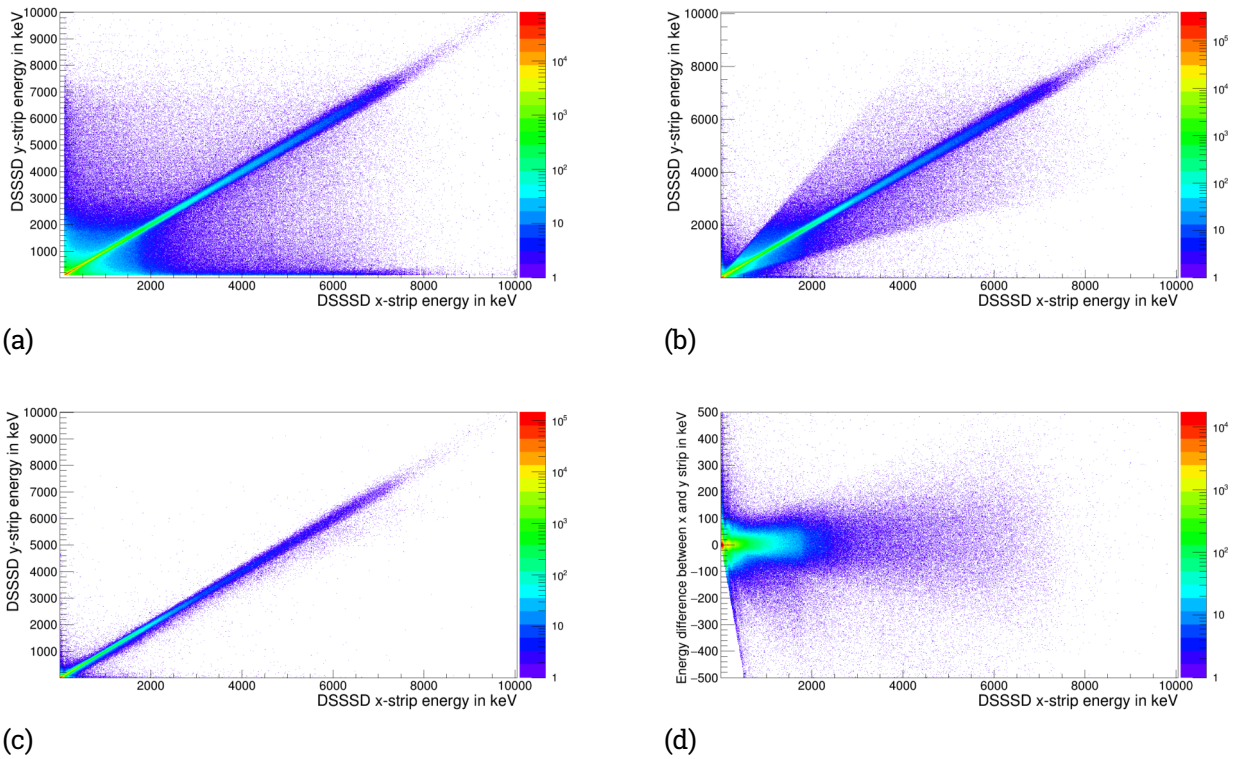

Figure 5.21.: Correlation between energy deposition in front and backside of DSSSD for all entries (a) and for the highest energy entry (b). The correlation forms a line after interstrip correction (c) and the rotated representation allows the setting of limits for the energy-loss difference (d).

5.4.1. Energy loss in DSSSDs

In order to more precisely filter out all plausible physical events, the two silicon strip detectors are checked. A particle hitting one of these detectors should leave more or less the same energy on the front as on the rear side of the waver, hence the energy of the x-strip and the y-strip should be equal. As first step all recorded hits exceeding a very low threshold are displayed in Figure 5.21 (a). Clearly visible is the diagonal line that displays the physically reasonable events where the energy difference between front and rear signal is small. In the the low energy regime one can find a large number of hits with larger gap in energy and along the x-axis a lot of events barely make it above the threshold. This last effect vanishes when only plotting the highest detected energy of an entire event as shown in Figure 5.21 (b). Hits of lower energy, either on front or on rear side, are strongly suppressed. An even better picture, see Figure 5.21 (c), evolves when permitting only single-hit events, i.e. leaving out all interstrip or double-hit events. The diagonal is now very dominant and in a last step the hits deviating from this line can be excluded by setting a thresold and applying it to the rotated representation as displayed in Figure 5.21 (d). The result are only events that hit one x and one y-strip whilst depositing an amount of energy in each strip that at most differs by the set threshold of $50\,\mathrm{keV}$ for DSSSD1 and of $70\,\mathrm{keV}$ for DSSSD2.

5.4.2. Vertex reconstruction

A very efficient way to suppress events that do not originate from the target is to apply a cut on the correlation plot between DSSSD and petal. As discussed before, the correlation between petal and DSSSD was not symmetric and was corrected by shifting the positions of the detectors. Hence, it is completely sufficient to focus on one detector arm. In Figure 5.17 the correlation is shown for the polypropylene target for LUND1 and DSSSD1. A clear anti-correlation line is visible that emerges when particles are emitted from a central point and pass through the DSSSD on the way to deposit their main share of energy in the petal.

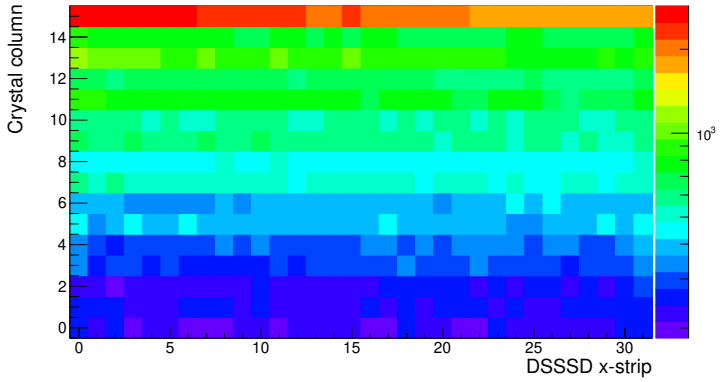

Figure 5.22.: Correlation between DSSSD and petal for an empty target frame and proton beam of $200\,\mathrm{MeV}$.

In contrast, the empty target run shown in Figure 5.22 does not show the anti-correlation line as there is no central point such as a target. What is dominant in this plot, is the high count rate in crystal group 15. It originates from interactions of beam particles with the surroundings, especially air, and occur most likely in the detector group closest to the beam, namely crystal group 15.
Consequently, a cut is applied on the correlation between DSSSD and petal to reduce the data set to events

of interest. Due to the differences in alignment, individual cuts need to be set for the two detector arms. This is easily done as the limits of the region of interest can be analytically expressed by

$$N_{col} = \frac{N_{col,maxlimit}}{N_{strip,maxlimit}} N_{strip} + N_{col,maxlimit} \tag{5.11}$$

and

$$N_{col} = \frac{N_{col,minlimit}}{N_{strip,minlimit}} N_{strip} + N_{col,minlimit}. \tag{5.12}$$

Here, $N_{col,maxlimit}$ and $N_{col,minlimit}$ describe the intersection on y-axis and $N_{strip,maxlimit}$ and $N_{strip,minlimit}$ the intersection on x-axis. The result is given in Figure 5.23, were the number of entries declines drastically when applying the cut. For the ^{208}Pb target, only $2\,\%$ of triggered events lie within the cut that refers to particles originating from the target spot.

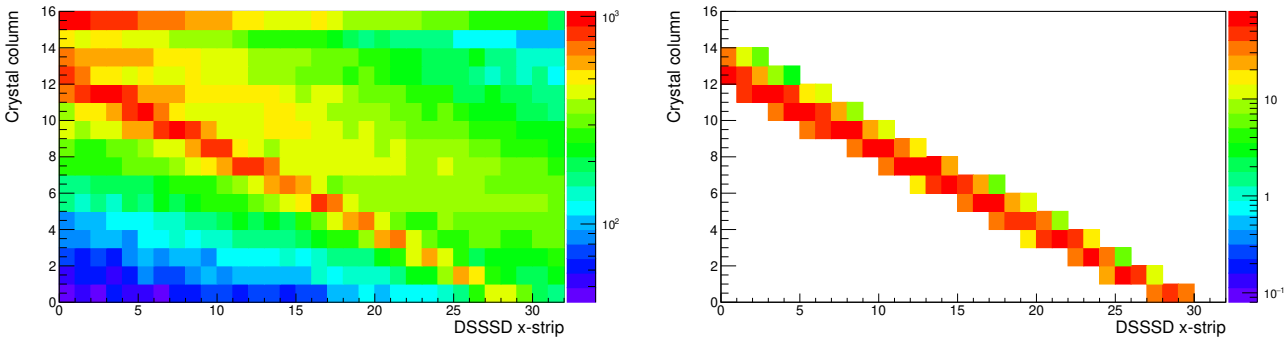

Figure 5.23.: The vertex plot of ^{208}Pb target run (a) is reduced to its anti-correlation line by applying a vertex cut (b).

5.4.3. Particle identification

Besides the vertex reconstruction, the identification of particles in CsI(Tl), as described in Chapter 2.3.5, will be employed to reduce the data set and to pick out events of interest. The sum PID of LUND1 is given in Figure 5.24 revealing clear lines that refer to γ rays, fully stopped protons and heavier particles. However, this representation makes it difficult and error-prone to separate the particle branches.

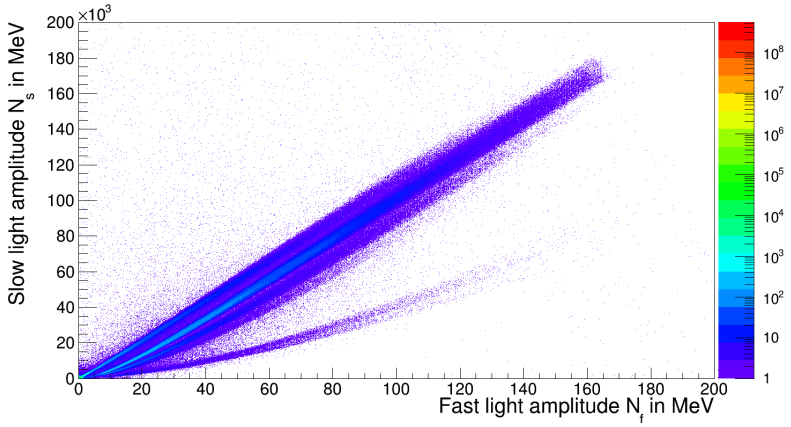

Figure 5.24.: The PID sum-plot of all LUND1 channels with closly together lying lines for γ rays, protons and heavier particles.

The solution here is to go back to single crystal level, redo the PID representation and fit a linear function to the γ branch. This slope gives the angle α of Equation 2.9 and therefore defines the necessary anti-clockwise rotation of each crystal's PID plot. The result is again given in Figure 5.25 as sum of all detector channels in LUND1. The gain in separability is striking and graphical cut can be applied to select only fully stopped protons.

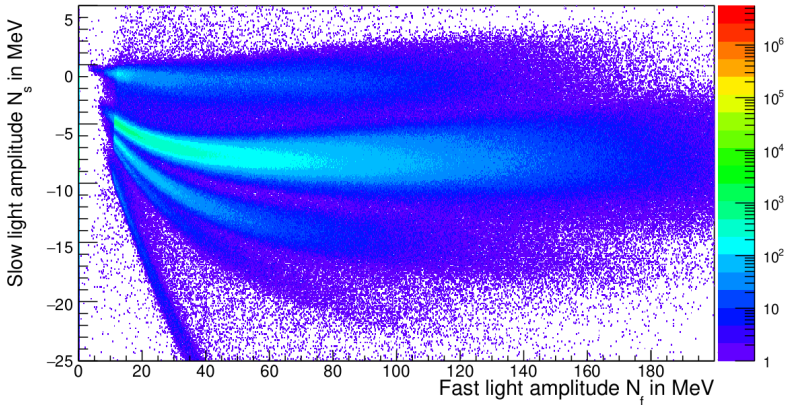

Figure 5.25.: The PID plot of all LUND1 channels in reduced representation revealing a clear separability of branches.

The need of this analysis tool comes apparent in Figure 5.26 where all particles are shown that fulfill the following conditions:

- One proton in each detector arm exceeds the proton threshold.
- Both protons lie within the respective vertex cut.

As Figure 5.26 shows, not only protons are detected in the petals, but also high-energy γ-rays and heavier particles. With the help of the graphical cut it is possible to get rid of these events that falsify the analysis of the $(p, 2p)$ events. For the ^{208}Pb target, approximately $60\,\%$ of the two-proton events lie within the PID cut.

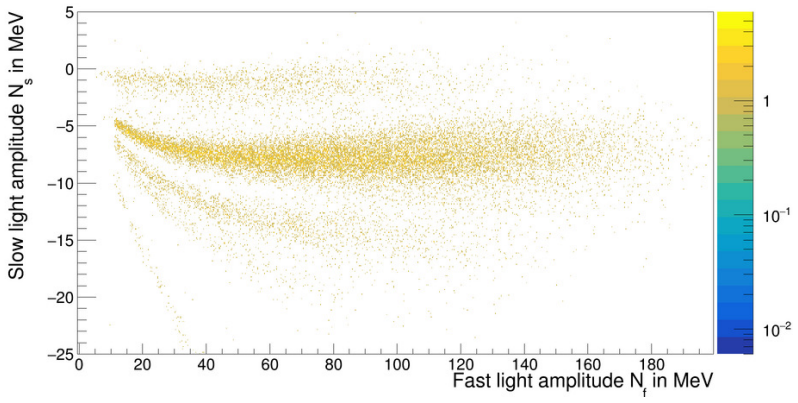

Figure 5.26.: The PID plot of LUND1 after application of the vertex cut.

5.5. Experimental results

In the previous section possible steps for the selection of the reaction channels were explained. In this section the experimental results obtained from the CALIFA test experiment, that aimed to show the feasibility of the quasi-free scattering on ^{208}Pb, will be presented.

5.5.1. Identification of the elastically scattered protons

As the measurement of absolute cross section is hardly possible, a standard approach is the identification of the reaction channel of interest and its normalization to a well known reaction channel like the one belonging to elastic scattering. For the plastic target there are two possible scatterings partners for the incoming protons, namely the hydrogen and the ^{12}C core. The elastic proton-proton scattering is the dominant process, as shown in Figure 5.27. For exactly two detected protons, the particle is detected in the more forward angles due to the acceptance of the petals, see Figure 5.27 (a). When the conditions are changed to exactly one proton, the energy line continues to higher angles following the dependence of the energy from the angle as previously shown in Figure 5.19.

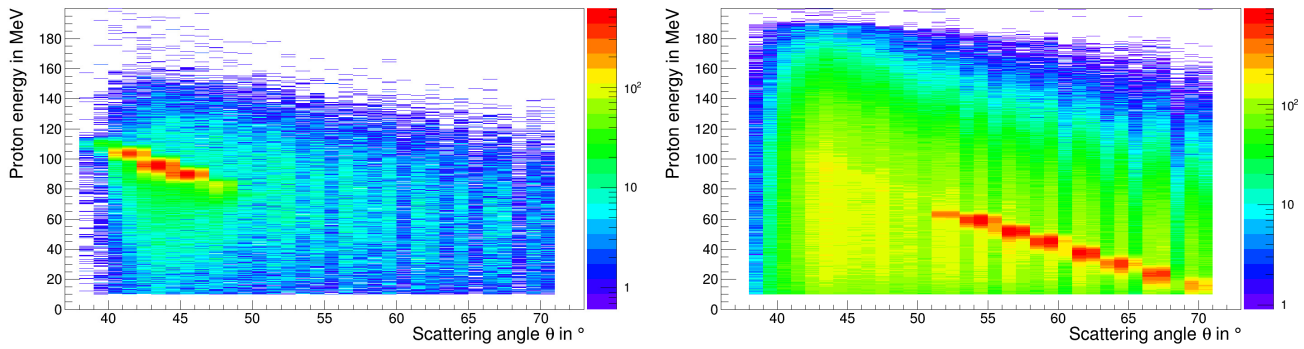

(a) (b)

Figure 5.27.: Energy of protons scattering from a plastic target for exactly two detected protons (a) and for proton multiplicity one (b) depending on the scattering angle θ.

The elastic scattering on the ^{12}C core can not be identified in Figures 5.27 (a) and (b). The dependence of energy from the angle for the scattering process on ^{12}C can be calculated analogously to the proton-proton scattering and the result is shown in Figure 5.28 (a). As there is no additional line stemming from a different scattering center than hydrogen visible in the energy over scattering-angle plot, the proton-energy spectrum can be analysed for each petal column individually. As an example, an appropriate spectrum is shown in Figure 5.28 (b) for scattering angles of $60° \pm 2°$. The protons that scattered of hydrogen cores are clearly peaking out at $45\,\mathrm{MeV}$ of the proton background. At the high-energy end of this background, a second peak of very low intensity emerges. The position at $175\,\mathrm{MeV}$ is in accordance with the result of the calculations when taking into account the surrounding air and the energy loss in the setup.

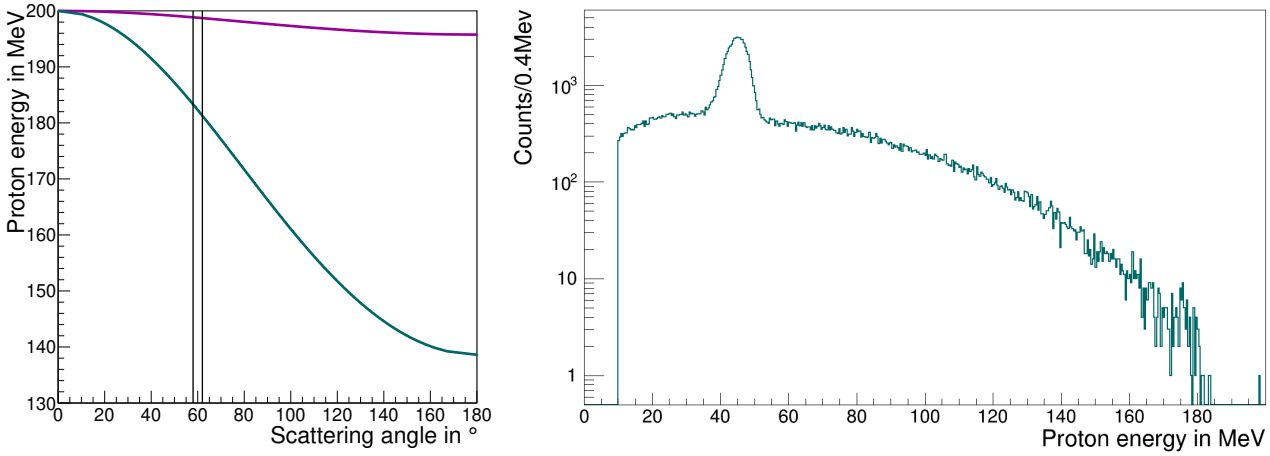

Figure 5.28.: Angular dependence of the proton energy for plastic (green) and ^{208}Pb (purple) target (a) and proton-energy spectrum for the plastic target at $60° \pm 2°$ (b).

For the ^{208}Pb target the picture looks similar and as the dominant proton-proton scattering is not present, no correlation between energy and angle can be observed as shown in Figure 5.29 (a). For the shown case of exactly one detected proton, the scattered particles are detected in more forward direction. The proton-energy spectrum, shown in Figure 5.29 (b), equals the afore shown spectrum for the plastic target run without the peak stemming from elastic proton-proton scattering. At the end of the proton background, there are very few protons that originate from the elastic scattering on the ^{208}Pb core and are consistent with Figure 5.28 (a).
This low number of elastically scattered protons is in accordance to expectations when considering a total reaction cross-section of $\sigma_R = 1.7\,\mathrm{b}$ for protons of $200\,\mathrm{MeV}$ impinging on a ^{208}Pb target [53]. In contrast to the total reaction cross-section, the differential cross section $\frac{d\sigma}{d\Omega}$ expected in the angular range covered by the petals ranges from $1\,\frac{\mathrm{mb}}{\mathrm{sr}}$ down to values smaller than $0.01\,\frac{\mathrm{mb}}{\mathrm{sr}}$ [42]. Hence, the positioning of the petals makes it nearly impossible to measure the products of the elastic scattering that are stronlgy emitted to forward angles. The overall statistics of the ^{208}Pb run is neither sufficient to evaluate the cross section of the elastic scattering nor to use it as reference point for a normalization of the reaction channel of interest.

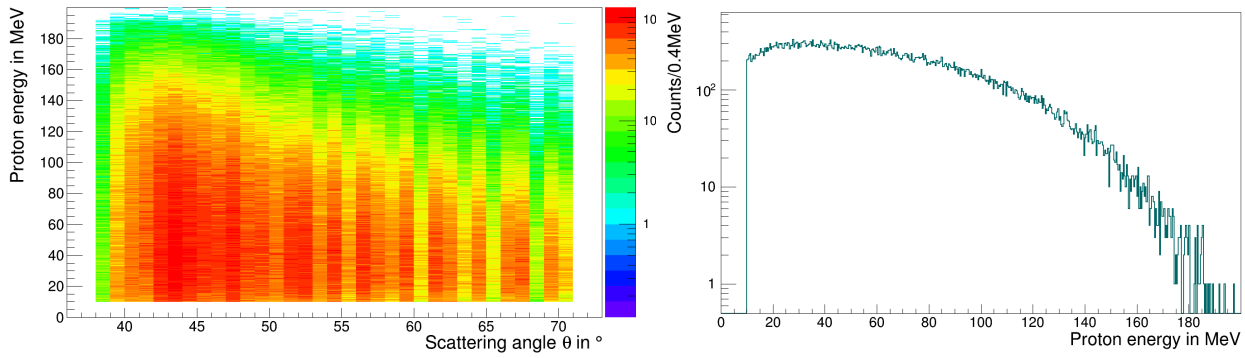

Figure 5.29.: Energy of protons scattering from ^{208}Pb depending on the scattering angle θ when exactly one proton is detected (a) and corresponding proton-energy spectrum at $60° \pm 2°$(b).

5.5.2. Energy correlation of the two-proton channel

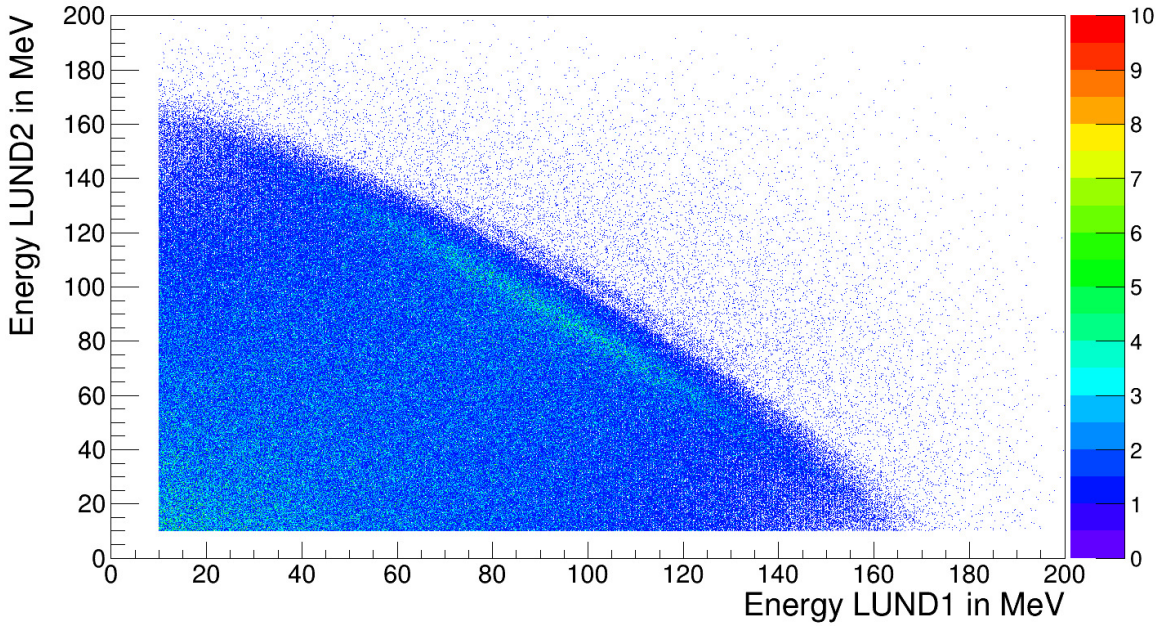

Figure 5.30.: Correlation plot for the ^{208}Pb target exhibiting an anti-correlation band between the two outgoing protons.

A first indication for a $(p, 2p)$ reaction is shown in Figure 5.30, where the proton energy deposited in LUND1 is plotted against the deposited proton energy in LUND2. When demanding exactly one proton in each petal, both exceeding the energy threshold $E_{trigger} = 10\,\mathrm{MeV}$, an anti-correlation band can be observed. The smeared appearance of the band is similar to the simulation result shown in Figure 4.14, and is a consequence of the energy resolution of the crystals and the large Fermi momentum $p_F = 250\,\mathrm{Mev/c}$ of the scattered-out proton. These two factors also rule out the profit of cuts on the anti-correlation lines referring

to ground state and excited state of the residual nucleus as those lie inseparably within the anti-correlation band. In addition to the anti-correlation band, another line is visible that is shifted towards higher energies. The origin of this is the contamination of the target material with water leading to elastic scattering on the included hydrogen.

At this point, a look at the analysed data set on the $^{16}\mathrm{O}(p,2p)^{15}\mathrm{N}$, that was gained within the same experimental campaign utilizing the known setup, is worthwhile. As shown in Figure 5.31 (a), the energy correlation has two anti-correlation lines that refer to the ground state and the excited state at $E_{3/2^-} = 6.32\,\mathrm{MeV}$ [54] in the residual nucleus $^{15}\mathrm{N}$. Due to the relatively high excitation energy, the two lines are clearly separated and a selective cut can be performed that takes into account all events that lie along the anti-correlation line associated to the excited state. Figure 5.31 (b) gives the γ-ray spectrum that was recorded in coincidence with TUDA1, operated in low-gain mode. Besides the $511\,\mathrm{keV}$ line, also the deexcitation of the residual nucleus via the emission of γ rays of $6.32\,\mathrm{MeV}$ stands out of the background.

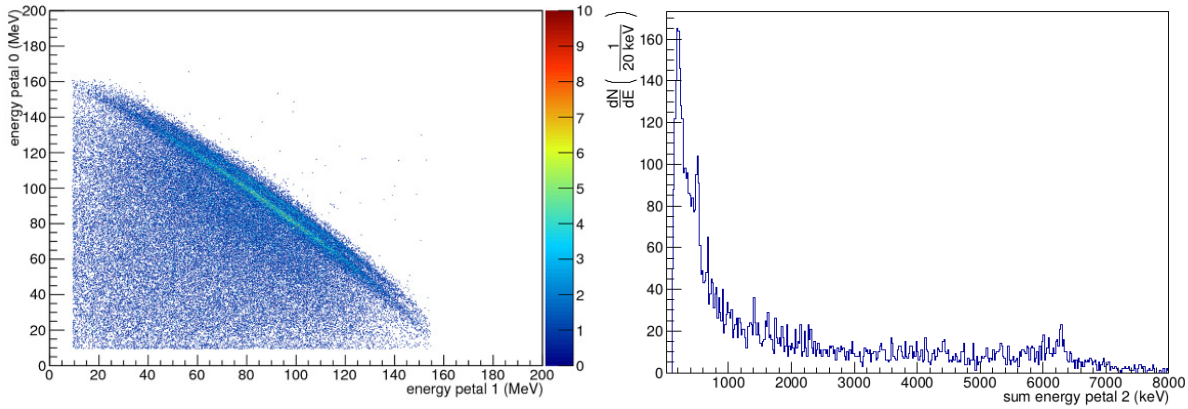

Figure 5.31.: Energy correlation between the two outgoing protons (a) and the coincident γ rays for $^{16}\mathrm{O}(p,2p)^{15}\mathrm{N}$ detected in TUDA1 (b), taken with permission from [34].

This very efficient approach to extract the coincident γ rays was performed on the $^{208}\mathrm{Pb}$ data as well. In coincidence with two protons, whose energies lie within $\pm 2\,\mathrm{MeV}$ along the drawn curve in Figure 5.32 (small), γ rays are detected in TUDA1 and are displayed in Figure 5.32. The $511\,\mathrm{keV}$ line stands out form the background, but no transition that can be related to $^{207}\mathrm{Tl}$ is observed. Moving the scanning window over the energy-correlation plot and checking the coincident γ-ray spectrum does not give further hints on transitions in the residual nucleus. Possible reason for this difference between $^{16}\mathrm{O}$ and $^{208}\mathrm{Pb}$ runs can be the target itself. As for the $^{16}\mathrm{O}(p,2p)^{15}\mathrm{N}$ a water-jet target of $(500 \pm 5)\,\mu\mathrm{m}$ diameter without target frame was used, the chosen $^{208}\mathrm{Pb}$ target of $8.5\,\mu\mathrm{m}$ was very thin. In combination with a relatively large beam-spot size, also the target frame plays an important role on the creation of background that dominates the seldom happening reactions of interest. Hence, a different approach of selecting the γ rays of interest was chosen.

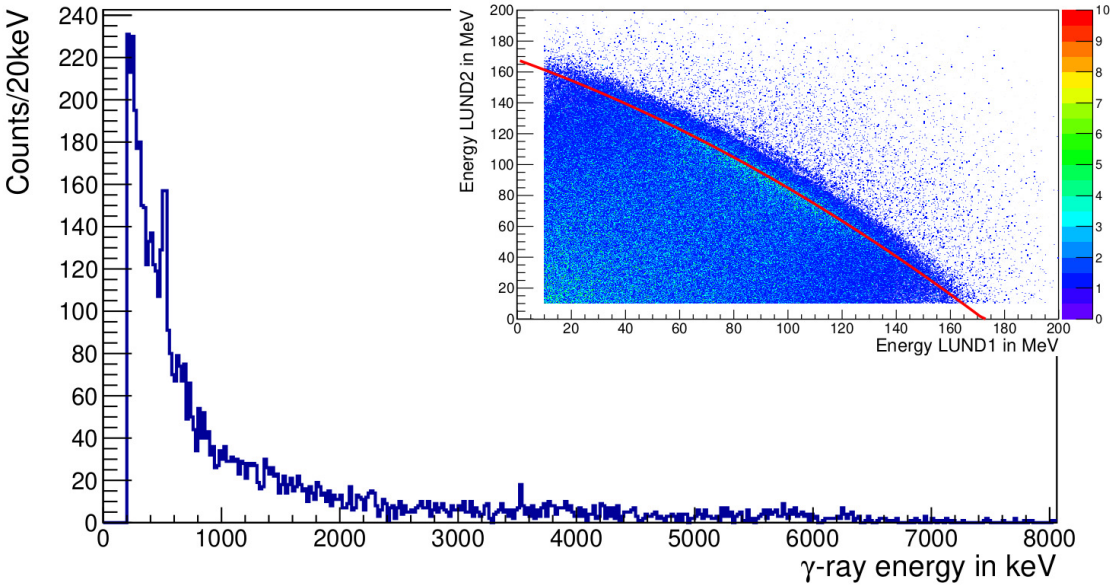

Figure 5.32.: γ-ray spectrum as derived from proton-pair selection based on the association with the excitation band in the energy-correlation plot.

5.5.3. γ-ray spectrum for two-proton events

As the direct cut on the proton-energy correlation, that includes all proton events succeeding an energy threshold of $E_{threshold} = 10\,\mathrm{MeV}$, was not successful, the selection tools described in Chapter 5.4 were applied. A severe reduction of background is achieved when applying the following constrains:

- **Vertex reconstruction** needs to be fulfilled by both protons.
- **Energy loss in** front and backside of **DSSSDs** must be comparable.
- There are **exactly two protons** exceeding the threshold of $E_{threshold} = 10\,\mathrm{MeV}$ and one is detected in each detector arm.
- There is **exactly one γ ray** detected in TUDA1 that exceeds the threshold of $E_{threshold} = 200\,\mathrm{keV}$.

The impact of the vertex condition on the γ-ray spectrum is evident in Figure 5.33, where the number of entries is drastically reduced. Noteworthy is the vanishing of the $511\,\mathrm{keV}$ line that can not be connected to the interaction within the target. In general, γ rays are observed up to $E_\gamma \approx 7\,\mathrm{MeV}$. Beyond this point there are only very few events detected in TUDA1. This is in agreement with the proton-separation energy of ^{207}Tl of $S(p) = 7.255\,\mathrm{MeV}$ and its neutron-separation energy of $S(n) = 6.852\,\mathrm{MeV}$ [55] because excitation energies above these values will lead to break-up, resonances etc., but not to the emission of γ rays.

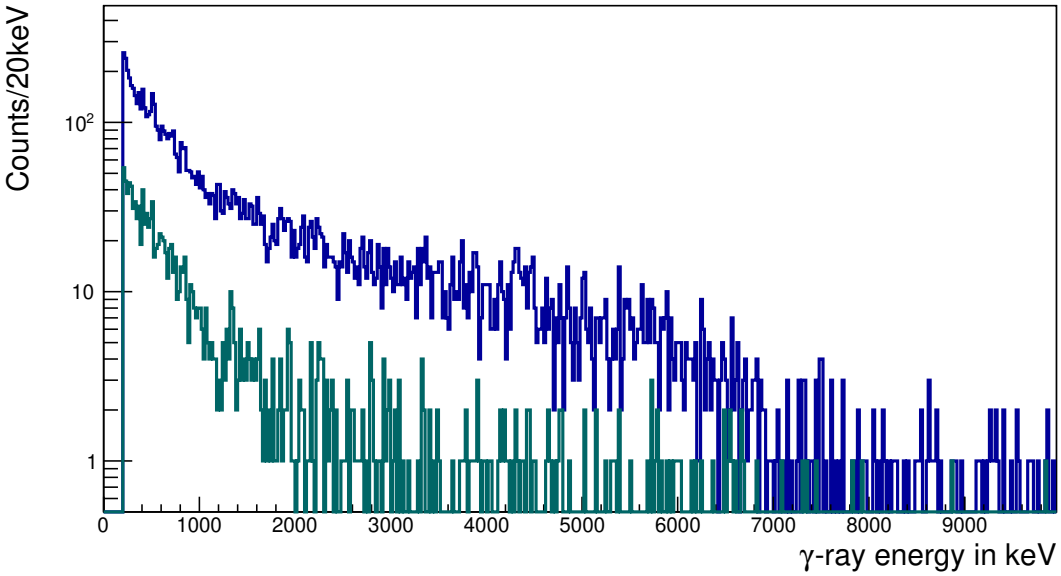

Figure 5.33.: Spectrum of γ rays exceeding the threshold in coincidence with two protons (blue) and γ-ray spectrum with additional vertex condition on the two protons (green).

Besides the listed restrictions, also the QPID identification of the outgoing protons can be employed to further restrict the selection of events. In Figure 5.34 (a) the γ-ray spectrum is shown after application of all listed restrictions. A peak stands out from the background at $1330\,\mathrm{keV}$ that can be associated with the transition from the $5/2^+$-state to the $3/2^+$-state in ^{207}Tl at $1331.7\,\mathrm{keV}$ [56], as indicated in Figure 4.2. It is not possible to mark out more transitions neither in the lower nor in the higher energy region.
Deploying the particle identification on the two detected protons, the number of events is further on reduced, as shown in Figure 5.34 (b). The afore described transition of ^{207}Tl is apparent and stands out stronger due to the reduction of uncorrelated events. In the lower γ-energy region a peak shows up at $840\,\mathrm{keV}$ that can be identified as the first excited state of $843.76\,\mathrm{keV}$ in ^{27}Al [57] and is a random coincidence due to the large amount of aluminum in the target frame and the entire setup.

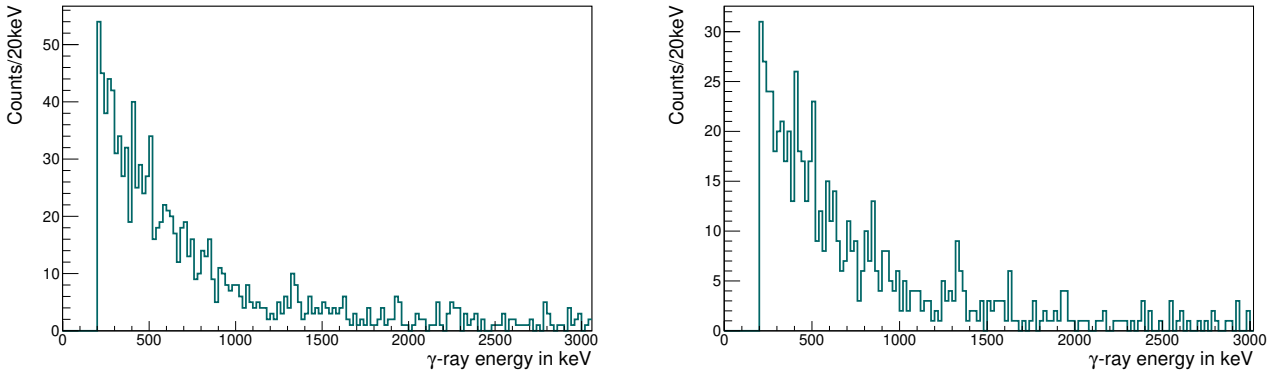

Figure 5.34.: γ-ray spectrum after applying the listed restrictions (a) and with additional QPID identification of the two coincident protons (b).

Another piece of information that can be exploited at this point is the timestamp information. As shown in Figure 5.35 (a), the difference in timestamps between the detected γ ray and the triggering proton can be used to separate prompt events, that are connected to the reaction, and general background. γ rays stemming from the reaction in the target lie within the prompt peak that can be located from $-300\,\mathrm{ns}$ to $+500\,\mathrm{ns}$. When taking only events within this window into account and maintain all former conditions, the γ-ray spectrum of Figure 5.35 (b) emerges. The reduction of γ ray with energies smaller $1100\,\mathrm{keV}$ is convincing, as it does not affect the transition of interest. The peak-to-background ratio of the γ-ray transition at $1331.7\,\mathrm{keV}$ improves significantly and the observation of 10 $(p, 2p)$ events of interest can be claimed.

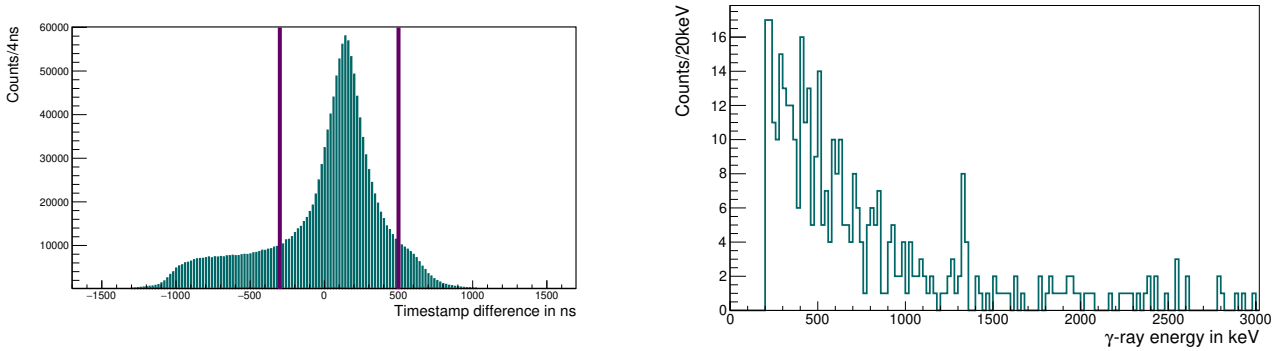

Figure 5.35.: Timestamp difference between γ ray and trigger signal for γ rays exceeding the thresold (a) and the resulting prompt γ-ray spectrum (b) with conditions as in Figure 5.34 (b).

This small yield of events of interest may also explain the absence of a definable transition of $351.1\,\mathrm{keV}$ leading from the $3/2^+$-state to the $1/2^+$ ground-state [58]. This transition lies in the low-energy region of the γ-ray spectrum that is still affected by background reactions and due to its low expected number it is lost in background. What further impacts the distinction of this transition, are Compton-scattering events, that frequently take place for γ rays of lower energy, and that lead to a loss of energy in the surroundings. As the energy threshold of TUDA1 crystals was set to $85\,\mathrm{keV}$, this results in losing part of the energy whenever the Compton-scattered share does not exceed the threshold. Hence, from the analysed data set it is not possible to conclude whether the transition from $3/2^+$-state to $1/2^+$-state took place.

5.5.4. γ-ray spectrum for one-proton events

Complementary to the γ-ray spectra that are in coincidence with two outgoing protons, information can be extracted from those γ rays that are in coincidence with exactly one proton. This is shown in Figure 5.36 for all γ rays exceeding the threshold of $200\,\mathrm{keV}$ but without any further restrictions on the proton.
Due to a high amount of carbon in the alveoli and in the support structure of the setup, the first excited state in ^{12}C with a γ-ray energy of $4439.5\,\mathrm{keV}$ [59] is observed for both targets together with its single and double-escape peak, but disappears when the proton interacted at the target spot. The lower energy region is dominated by the $511\,\mathrm{keV}$ peak and reveals for both targets transitions at $415\,\mathrm{keV}$, $430\,\mathrm{keV}$ and $720\,\mathrm{keV}$. The source of this γ rays could not be identified but lie outside the target as they appear independently of the target material and do not intensify when the vertex condition is fulfilled by the proton.
The γ-ray spectra of the two targets differ at one point located around $1000\,\mathrm{keV}$. Here, the ^{208}Pb spectrum shows a clear peak structure that can not be observed with the polypropylene target. As shown in Figure 4.2,

there is a strong transition from the $11/2^-$-state to the $3/2^+$-state by emitting a γ-ray of $997.1\,\mathrm{keV}$ [56]. The long live time of $1.33\,\mathrm{s}$ of the $11/2^-$-state [60] rules out the observation of this γ-ray in coincidence with the two protons causing the $(p, 2p)$ event. Hence, this transition occurs and is detected together with a random triggering proton that does not need to fulfill any vertex condition. Moreover, the occurrence of the $997.1\,\mathrm{keV}$ transition is not affected by a shift of the timestamp window. Due to the low statistics when gating outside the prompt response-peak, this can not be validated for the current data set. Anyhow, the difference in the two spectra, while applying the same conditions, is a strong argument that the observed transition stems from ^{207}Tl and belongs to its isomeric $11/2^-$-state.

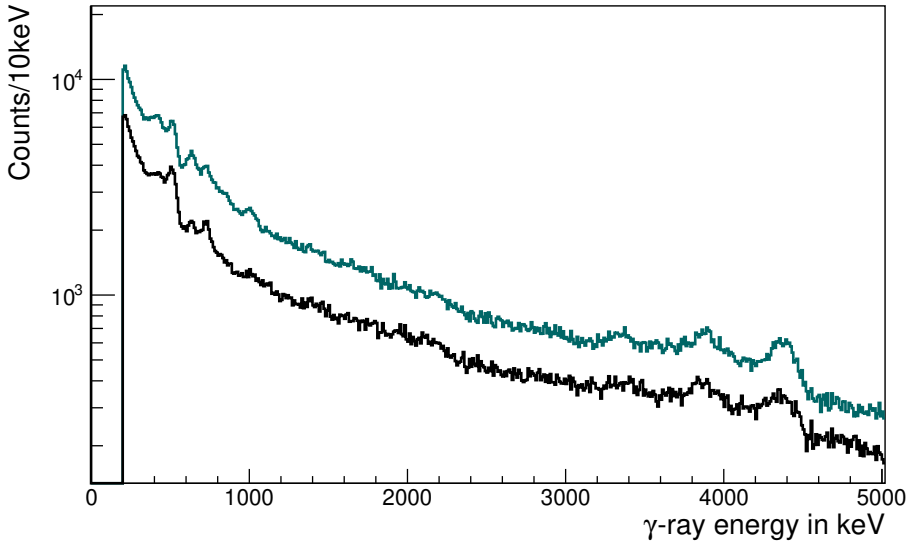

Figure 5.36.: Spectrum of γ rays exceeding the threshold in coincidence with exactly one proton for the ^{208}**Pb target (green)** and for the **polypropylene-target run (black)**.

6. Conclusions and future perspectives

6.1. Summary of the test experiment

The performed test experiment aimed to show the feasibility of studying the ^{208}Pb$(p, 2p)^{207}$Tl reaction in direct kinematics by measuring the emitted γ rays with three petals of the CALIFA calorimeter. In addition to the setup employed by R.Neveling et al. [43] to extract cross sections of the reaction, the CALIFA test setup was capable of detecting the coincident γ rays with sufficient resolution. Hence, the analysis does not solely depend on the detection of the two outgoing protons. Moreover, already the used, limited amount of detector channels made the coverage of a wider angular range possible exceeding the former setup of R.Neveling et al. that limited the measurement to a single angular pair.
Therefore, 194 CsI(Tl) crystals of the CALIFA Barrel were successfully operated together for the first time and in addition 128 DSSSD channels were read-out by the CALIFA DAQ. The performance of the CALIFA scintillators was in agreement with the requirements for the CALIFA calorimeter, as summarized in Table 6.1. For LUND1/2, the energy resolution for γ rays is given when operated in low gain mode resulting in a slightly worse resolution than required. This can be overcome by the usage of dual-range preamplifiers.

	CALIFA	LUND1	LUND2	TUDA1
γ rays $(1\,\mathrm{MeV})$	5-6 %	6.70(4) %	6.82(4) %	5.29(3) %
protons	< 1.4 %	1.5(2) %	1.5(2) %	-

Table 6.1.: Resolution of the CALIFA petals for γ rays and protons given in FWHM.

From the reaction of interest, the γ-ray transition of $1330\,\mathrm{keV}$ from the $5/2^+$-state to the $3/2^+$-state in ^{207}Tl could be identified in coincidence with two outgoing protons. Here, the importance of suited restrictions on the data set could be shown as well as differences in the analysis between the ^{208}Pb and the ^{16}O data-set. In the γ-ray spectrum, that was observed in coincidence with exactly one proton, the transition from the $11/2^-$-state to the $3/2^+$-state in ^{207}Tl at an energy of $997\,\mathrm{keV}$ stood out from the background that was otherwise similar to the polypropylene-target background. An association with two protons using the current setup is not possible due to the long lifetime of the state being $T_{1/2} = 1.33\,\mathrm{s}$ [60] and the delayed emission of the γ ray.

6.2. Suggestions for improvement of the setup

As the extraction of the cross section for the reaction was not possible due to the very low statistics and the analysis of the γ-ray spectra was challenging, some changes need to be made in order to optimize the setup for the measurement of $(p, 2p)$ reaction on heavier targets.

Target thickness

In the planning phase of this experiment, the expected beam current that was taken into account when choosing the target thickness was assumed to be higher than later delivered during experiment. As a result, a target thickness of $9.7\,\frac{\mathrm{mg}}{\mathrm{cm}^2}$ seemed to be optimal in order to deliver a reasonable event rate that can be handled by the CALIFA DAQ. However, the reduced beam current also diminished the amount of $(p, 2p)$ events in the entire data set. In combination with the quite large beam-spot size, this leads to an unfavorable ratio of desired ^{208}Pb$(p, 2p)^{207}$Tl events to background. This background can not be completely suppressed and is caused strongly by events that took place near the target, especially originating from the target frame.

Tracker before target

In order to free oneself partly from the dependence on high statistics to calculate the cross section, an additional tracker before the target can be placed. As the elastic scattering of protons on the ^{208}Pb can not be observed due to its very low cross section in comparison to the other reaction channels, a workaround for future measurements could be a counter of the incoming protons before their interaction with the target. A normalization of the $(p, 2p)$ cross-section to a different reaction channel is avoided and the analysis can be simplified.

Angular coverage

A significant improvement of the setup could be achieved by either a more efficient placement of the already used detectors or by increasing the number of detection channels and hence realizing a larger angular coverage.
The first option is to place the two petals, dedicated to measure the protons in one plane, closer towards the beam line. This would increase the sensitivity in the angular region where most $(p, 2p)$ events are expected. The setup of the Kraków test experiment did not well cover the forward angular region resulting in a loss of events of either the polypropylene target or the ^{208}Pb$(p, 2p)^{207}$Tl reaction. In the same scope, an improvement of the alignment between petal and DSSSD is necessary to better illuminate the entire DSSSD and to cover all petal channels.
In the meanwhile, the second approach is easily achievable, namely increasing the number of detector channels. Already the change from single petals to double petals, where 128 CsI(Tl) crystals are placed in one aluminum housing, would directly double the azimuthal coverage of the setup. Also the use of Iphos segments, that can be brought closer to the beam line due to their geometry, would lead to an enhancement of the coverage in more forward direction. In combination with a optimized number of detection channels, also the use of dual-range preamplifiers would significantly raise the statistics for the γ rays as the petals in the reaction plane can be used to read out γ-ray events synchronously to proton hits.

6.3. Conclusion and outlook

Besides the investigation of the ^{16}O$(p, 2p)^{15}$N reaction, the test campaign in Kraków 2017 showed that with the CALIFA detector-array also studies of $(p, 2p)$ reactions on heavy target can be performed. As proof of concept, two known γ transitions in ^{207}Tl could be identified studying the reaction ^{208}Pb$(p, 2p)^{207}$Tl. Due to a variety of causes, the overall statistics for this reaction was very low making a quantitative analysis of the reaction channel of interest impossible. However, it could be shown in this work that the coincident measurement of the two outgoing protons together with the γ ray, stemming from the transition of the

$5/2^+$-state to the $3/2^+$-state in ^{207}Tl, is feasible and that the CALIFA setup provides an opportunity to overcome the limits of R.Neveling et al.'s setup [43].
In addition to the analysed data sets, there is a third data set on the $(p, 2p)$ reaction on ^{112}Sn and ^{124}Sn from the same test campaign. The evaluation of this run will help to complete the picture on this specific reaction in direct kinematics as the target mass lies in between the already studied nuclei. Hence, it will help to improve and optimize the setup and is a perfect test ground for the different approaches of selecting the events stemming from the quasi-free scattering.
Furthermore, with the phase-0 setup of CALIFA, as it is currently used at GSI, many more detection channels are available to rerun the ^{208}Pb$(p, 2p)^{207}$Tl experiment in inverse kinematics with very large angular acceptance. In addition to the number of channels, also dual-range preamplification and multi-event read-out is possible, leading to higher efficiency and overcoming the restrains due to the low statistics. A repetition of the measurement on ^{208}Pb in order to optimize the setup and analysis for inverse kinematics will give access to the neutron-rich isotopes in this mass region. As information is scarce there, this reaction channel will help to collect valuable information on the appearance and disappearance of magic numbers and therefore contribute to the understanding of nuclear structure.

A. Step-by-step instruction for attaching the reflector wrapping

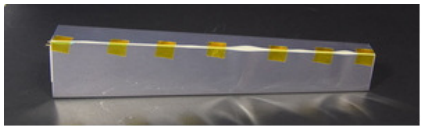

The crystal is wrapped in the mantel piece that is closed with several $1\,\mathrm{cm}$ strips of Kapton® tape. At this point, the crystal may stick out by $1-2\,\mathrm{mm}$ on the LAAPD side.
$\rightarrow$ The mantel piece should be optimize by cutting it with a scalpel if its fitting is too wide/long!

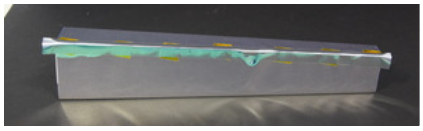

The gap between the cutting edges is then closed with silver polyester tape. The tape is attached along the gap, covering the Kapton® strips, and needs to overhang $5\,\mathrm{mm}$ on both sides.

The overhang on the entrance side is cut in along the edge.

The overhang is used to hold the wrapping of the entrance window by folding the two flaps inwardly.
$\rightarrow$ The entrance-window piece should be optimize by cutting it with a scalpel if its fitting is too broad/long!

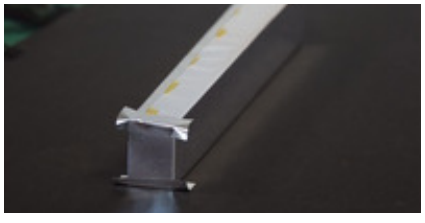

The reflector piece is fixed at the narrow sides by two strips of polyester tape with an overhang of $5\,\mathrm{mm}$ on both sides. They are cut in and folded around the corner.

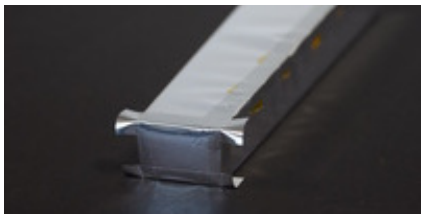

The previous step is repeated for the wide sides of the crystal.

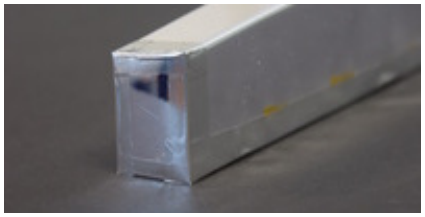

After closing all edges of the entrance window, the crystal needs to be pushed into the reflector pocket.
→ If the crystal is flush at the entrance side, but the mantel piece overhangs at the LAAPD side, it needs to be shortened by cutting it with a scalpel!

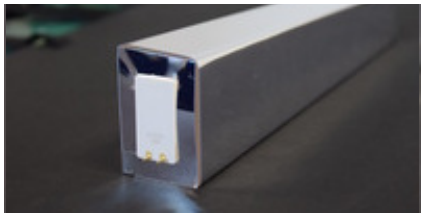

The overhang of the long edge is used to hold the wrapping of the exit window by folding the two flaps inwardly.
→ The exit-window piece should be optimize as well by cutting it with a scalpel if its fitting is too broad/long or the LAAPD is not placed perfectly!

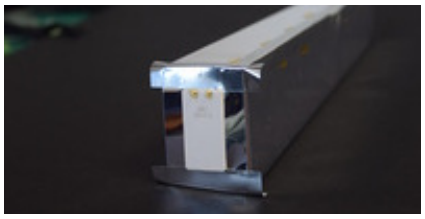

The reflector piece is fixed at the narrow sides by two strips of polyester tape with an overhang of $5\,\mathrm{mm}$ on both sides. They are cut in and folded around the corner.
→ The polyester tape should reach to the LAAPD, closing the gap between reflector and LAAPD! (If a connection to the gain-monitoring system is forseen, the area opposite the LAAPD pins is kept free of polyester tape)

The previous step is repeated for the wide sides of the crystal closing also the gap between LAAPD and reflector.

The assembled crystal is then equipped with its name tag that displays crystal type and ts unique crystal ID. Hence, it can be identified either by its crystal ID or the serial number of the LAAPD, that is etched into the LAAPD itself.

Bibliography

[1] H. Gegier, E. Marsden, and E. Rutherford, "On a diffuse reflection of the α-particles," *Proceedings of the Royal Society of London. Series A, Containing Papers of a Mathematical and Physical Character*, vol. 82, no. 557, pp. 495–500, 1909.

[2] E. Rutherford, "The scattering of α and β particles by matter and the structure of the atom," *The London, Edinburgh, and Dublin Philosophical Magazine and Journal of Science*, vol. 21, no. 125, pp. 669–688, 1911.

[3] E. Rutherford, "Bakerian lecture: Nuclear constitution of atoms," *Proceedings of the Royal Society of London. Series A, Containing Papers of a Mathematical and Physical Character*, vol. 97, no. 686, pp. 374–400, 1920.

[4] J. Chadwick, "Possible Existence of a Neutron," *Nature*, vol. 129, no. 312, 1932.

[5] C.F.v.Weizsäcker, "Zur Theorie der Kernmassen," *Zeitschrift für Physik*, vol. 96, p. 431, 1935.

[6] N. Bohr, "Can Quantum-Mechanical Description of Physical Reality be Considered Complete?," *Phys. Rev.*, vol. 48, pp. 696–702, Oct 1935.

[7] T. Mayer-Kuckuk, *Kernphysik, 7.Auflage*. 2002.

[8] C. S. B. Povh, K. Rith and F. Zetsche, *Particles and Nuclei, 8th Edition*. 2008.

[9] M. Goeppert-Mayer, "On Closed Shells in Nuclei. ii," *Phys. Rev.*, vol. 75, pp. 1969–1970, Jun 1949.

[10] J. J. O. Haxel and H. Suess, "On the "Magic Numbers" in Nuclear Structure," *Phys. Rev.*, vol. 75, pp. 1766–1766, Jun 1949.

[11] D.J. Rowe and J.L. Wood, *Fundamentals of Nuclear Models*. 2010.

[12] H.H. Gutbrot, *FAIR baseline technical report*. 2006.

[13] H. Geissel et al., "The Super-FRS project at GSI," *Nucl. Instrum. Methods Phys. Res. B*, vol. 204, pp. 71–85, 2003.

[14] M. Winkler et al., "The status of the Super-FRS in-flight facility at FAIR," *Nucl. Instrum. Methods Phys. Res. B*, vol. 266, no. 19, pp. 4183–4187, 2008.

[15] FAIR-Center, *Die Maschine*. 31.03.2021.

[16] B. Gastineau et al., "Design status of the r3b-glad magnet: Large acceptance superconducting dipole with active shielding, graded coils, large forces and indirect cooling by thermosiphon," *IEEE Transactions on Applied Superconductivity*, vol. 18, no. 2, pp. 407–410, 2008.

[17] K.-H. Schmidt et al., "Fission of nuclei far from stability," *Nuclear Physics A*, vol. 693, no. 1, pp. 169–189, 2001. Radioactive Nuclear Beams.

[18] J. -F. Martin et al., “Studies on fission with aladin - precise and simultaneous measurement of fission yields, total kinetic energy and total prompt neutron multiplicity at gsi,” *Eur. Phys. J. A*, vol. 51, no. 12, p. 174, 2015.

[19] G. Jacob and Th. A. J. Marris, “Quasi-free scattering and nuclear structure,” *Rev. Mod. Phys.*, vol. 38, pp. 121–142, Jan 1966.

[20] G. Jacob and Th. A. J. Marris, “Quasi-free scattering and nuclear structure. ii.,” *Rev. Mod. Phys.*, vol. 45, pp. 6–21, Jan 1973.

[21] R. C. Johnson and P. J. R. Soper, “Contribution of deuteron breakup channels to deuteron stripping and elastic scattering,” *Phys. Rev. C*, vol. 1, pp. 976–990, Mar 1970.

[22] J. Beringer et al., “Review of particle physics,” *Phys. Rev. D*, vol. 86, p. 010001, Jul 2012.

[23] S. Foroughi-Abari and A. Ritz, “LSND constraints on the Higgs portal,” *Phys. Rev. D*, vol. 102, p. 035015, Aug 2020.

[24] The R3B Collaboration, *Technical Report for the Design, Construction and Commissioning of the CALIFA Endcap*. 2015.

[25] M. Winkel, “Komplexe Pulsformalgorithmen und Teilchenidentifikation zur Echtzeit-Implementierung in CALIFA,” 2016.

[26] Saint Gobain, “BrilLanCe™Scintillators Performance Summary.” website, 2009.

[27] B. Pietras et al., “First testing of the CALIFA Barrel Demonstrator,” *Nucl. Instrum. Methods Phys. Res. A*, vol. 814, pp. 56–65, 2016.

[28] 3M Optical Systems, “Vikuiti TM Enhanced Specular Reflector (ESR).” website.

[29] H.-B-Rhee, “Investigation of the response of a CALIFA demonstrator and development of an APD test stand,” 2018.

[30] M. Gascon, H. Alvarez-Pol, J. Benlliure, E. Casarejos, D. Cortina-Gil, and I. Duran, “Optimization of energy resolution obtained with CsI(Tl) crystals for the R3B calorimeter,” *Nuclear Science, IEEE Transactions on*, vol. vol. 55, pp. pp. 1259–1262, June 2008.

[31] J. D. Valentine, W. W. Moses, S. E. Derenzo, D. K. Wehe, and G. F. Knoll, “Temperature dependence of CsI(Tl) gamma-ray excited scintillation characteristics,” *Nucl. Instrum. Methods Phys. Res. A*, vol. 325, no. 1, pp. 147 – 157, 1993.

[32] Hamamatsu Photonics K.K., “Data sheet of Si APD S8664-1010.” website, 2005.

[33] mesytec GmbH, “MPRB-16 / 32 (data sheet v1.1_01).” website.

[34] B. Heiss, “Development of a CALIFA demonstrator benchmark experiment using (p,2p) reactions in direct kinematics,” 2018.

[35] P. Cabanelas et al., “Performance recovery of long csi(tl) scintillator crystals with apd-based readout,” *Nucl. Instrum. Methods Phys. Res. A*, vol. 965, p. 163845, 2020.

[36] Eljen Technology, *Optical Cement EJ-500*. 01.27.2016.

[37] 3M Deutschland GmbH, *3M Polyester-Klebebaender*. 11.04.2020.

[38] The R3B Collaboration, *Technical Report for the Design, Construction and Commissioning of the CALIFA Barrel*. 2011.

[39] A. Knyazev et al., "Properties of the CsI(Tl) detector elements of the CALIFA detector," *Nucl. Instrum. Methods Phys. Res. A*, vol. 940, pp. 393 – 404, 2019.

[40] D. Britton, M. Ryan, and X. Qu, "Light collection uniformity of lead tungstate crystals for the cms electromagnetic calorimeter," *Nucl. Instrum. Methods Phys. Res. A*, vol. 540, no. 2, pp. 273–284, 2005.

[41] L.Atar et al., "Quasifree $(p, 2p)$ Reactions on Oxygen Isotopes: Observation of Isospin Independence of the Reduced Single-Particle Strength," *Phys. Rev. Lett.*, vol. 120, p. 052501, Jan 2018.

[42] D.A. Hutcheon et al., "The elastic scattering of intermediate energy protons from ^{40}Ca and ^{208}Pb," *Nuclear Physics A*, vol. 483, no. 3, pp. 429–460, 1988.

[43] R. Neveling et al., "Analyzing power and cross section distributions of the knockout reaction $^{208}\mathrm{Pb}(p, 2p)^{207}\mathrm{Tl}$ at an incident energy of 202 MeV," *Phys. Rev. C*, vol. 66, p. 034602, Sep 2002.

[44] J.W. Negele and E- Vogt, *Advances in Nuclear Physics*, vol. 20. 1991.

[45] F.Camera, A.Maj et al., *PARIS White Book*. 32021.

[46] D. Rudolph et al., *LYCCA Technical Design Report*. June 2008.

[47] V.Panin, "Fully exclusive measurements of quasi-free single-nucleon knockout reactions in inverse kinematics," 2012.

[48] O. Hansen et al., "Vibrational states of 207Tl," *Nucl.Phys. A*, vol. 127, no. 1, pp. 71–80, 1969.

[49] P. Lecoq, *Inorganic Scintillators for Detector Systems*. Springer, 2nd ed., 2017.

[50] P. Kienle and R. E. Segel, "Relative Pulse Height of Protons and Electrons in KI(Tl)," *Phys. Rev.*, vol. 113, pp. 909–911, Feb 1959.

[51] E. Byckling and K. Kajantie, *Particle kinematics*. Wiley, 1972.

[52] M. von Schmid, "Nuclear matter distribution of ^{56}Ni measured with EXL," 2015.

[53] Z.Zhang et al., "The cross sections and energy spectra of the particle emission in proton induced reaction on ^{204,206,207,208}Pb and ^{209}Bi," *EPJ Web Conf.*, vol. 146, p. 11019, 2017.

[54] F. Ajzenberg-Selove, "Energy levels of light nuclei A = 13âĂŞ15," *Nucl. Phys. A*, vol. 523, no. 1, pp. 1–196, 1991.

[55] G. Audi, A.H. Wapstra and C. Thibault, "The Ame2003 atomic mass evaluation: (II). Tables, graphs and references," *Nucl. Phys. A*, vol. 729, no. 1, pp. 337–676, 2003. The 2003 NUBASE and Atomic Mass Evaluations.

[56] B. Jonson, O. B. Nielsen, L. Westgaard, and J. Zylicz, "The Decay $^{207}_{80}\mathrm{Hg} \rightarrow {}^{207}_{81}\mathrm{Tl}$," in *Proc.Int.Conf.Nuclei Far from Stability*, 1981.

[57] N. Hayashi et al., "Highly accurate determination of Îş-ray emission probabilities for ^{27}Mg," *Nucl. Instrum. Methods Phys. Res. A*, vol. 422, no. 1, pp. 493–497, 1999.

[58] A. Rytz, "Recommended energy and intensity values of alpha particles from radioactive decay," *Atomic Data and Nuclear Data Tables*, vol. 47, no. 2, pp. 205–239, 1991.

[59] M. Munchet al., "Independent measurement of the hoyle state β feeding from $^{12}\mathrm{B}$ using gammasphere," *Phys. Rev. C*, vol. 93, p. 065803, Jun 2016.

[60] D.Eccleshall and M.J.L.Yates, "The $h_{11/2}$ single proton hole state in ^{207}Tl," *Physics Letters*, vol. 19, no. 4, pp. 301–303, 1965.

List of Figures

List of Tables

Acknowledgements

In the first place, I would like to thank my supervisor, Thorsten Kröll, for having given me the opportunity to work on my doctoral thesis in his group, for his advice, and support over the last years. Thank you, Thorsten, for telling me, that I am not too old to learn something new!

I am also grateful to the colleagues and students of the AG Kröll, former and present, who I have worked and spent time with. Special thanks to my CALIFA colleagues and my former supervisor, Tania Ilieva. Thank you, Tania, for reaching out to me, taking my hand and showing me how to walk the first steps in root!

Special thanks go to Giovanna Umberti Caroli and Carina Seeger, for helping me to solve many organisatoric and other issues over the years, I know my entire file is extensive. Thanks for all the non-physics conversations we had during those years!

Besides the support I received from the local group, I want to thank the CALIFA Collaboration. Without this collaboration the analysed experiment would never have taken place and the CALIFA detector array would not exist. Thanks to all of you for the discussions we had in the past years, your support and your motivation to make this detector work!

Although physics tries to describe how the world works in detail, it still does not display everything. That is why I want to thank my family and close friends for the support I received. Especially in the last months, things would have looked very different without you! Thank you for your help!

Thank you, Mom and Dad, for supporting me and enabling me to study physics!

Thank you, Corinna, for being my friend and companion through all our study time up to the summit of getting our Dr. degrees!

Thank you, Michi, for being my friend for far over twenty years and that I always can rely upon you!

Thank you, Joachim, for the support I receive from you and for having my back. Without you, this thesis would not have been possible.

And finally, my children...

Thank you for being the reason to never quit and being my inspiration every single day! I love you!

This work is supported by the German BMBF under contract 05P12RDFN8, 05P15RDFN1, 05P19RDFN1 and 05P21RDFN2, has received funding from the European Union's Horizon 2020 research and innovation programme under grant agreement no. 654002, HGS-HIRE for FAIR, and was supported by the NUSTAR/FAIR Collaboration, the R^3B Collaboration, and especially the CALIFA Collaboration.